

Electronic Theses and Dissertations, 2004-2019

2006

A Fluid Structure Interaction Model Of Intracoronary Atherosclerotic Plaque Rupture

Eric Teuma-Melago
University of Central Florida

 Part of the [Mechanical Engineering Commons](#)
Find similar works at: <https://stars.library.ucf.edu/etd>
University of Central Florida Libraries <http://library.ucf.edu>

This Doctoral Dissertation (Open Access) is brought to you for free and open access by STARS. It has been accepted for inclusion in Electronic Theses and Dissertations, 2004-2019 by an authorized administrator of STARS. For more information, please contact STARS@ucf.edu.

STARS Citation

Teuma-Melago, Eric, "A Fluid Structure Interaction Model Of Intracoronary Atherosclerotic Plaque Rupture" (2006). *Electronic Theses and Dissertations, 2004-2019*. 1072.
<https://stars.library.ucf.edu/etd/1072>

A FLUID STRUCTURE INTERACTION MODEL OF INTRACORONARY
ATHEROSCLEROTIC PLAQUE RUPTURE

by

ERIC ARNAUD VALASKI TEUMA-MELAGO

B.S. University of Paris Val de Marne - Créteil, France, 1998

M.S. University of Paris Val de Marne - Créteil, France, 1999

Postgraduate Degree of the Doctoral Study, Ecole Nationale Supérieure D'arts et Métiers
(ENSAM) - Paris, France & Ecole Normale Supérieure (ENS) - Cachan, France, 2000

A dissertation submitted in partial fulfillment of the requirements
for the degree of Doctor of Philosophy
in the Department of Mechanical, Materials and Aerospace Engineering
in the College of Engineering and Computer Sciences
at the University of Central Florida
Orlando, Florida

Fall Term
2006

Major Professor: Olusegun J. Ilegbusi

© 2006 Eric Valaski Teuma

ABSTRACT

Plaque rupture with superimposed thrombosis is the primary cause of acute coronary syndromes of unstable angina, myocardial infarction and sudden death. Although intensive studies in the past decade have shed light on the mechanism that causes unstable atheroma, none has directly addressed the clinical observation that most myocardial infarction (MI) patients have moderate stenoses (less than 50%). Considering the important role the arterial wall compliance and pulsatile blood flow play in atheroma rupture, fluid-structure interaction (FSI) phenomenon has been of interest in recent studies. In this thesis, the impact is investigated numerically of coupled blood flow and structural dynamics on coronary plaque rupture. The objective is to determine a unique index γ that can be used to characterize plaque rupture potential.

The FSI index, developed in this study for the first time derives from the theory of buckling of thin-walled cylinder subjected to radial pressure. Several FSI indices are first defined by normalizing the predicted hemodynamic endothelial shear stress by the structural stresses, specifically, by the maximum principal stress (giving the ratio R_1), and the Von Mises stress (giving the ratio R_2). The predicted R_1 at the location of maximum R_2 (i.e. $R_1 \{ R_{2_max} \}$) denoted γ , is then chosen to characterize plaque rupture through systematic investigation of a variety of plaque characteristics and simulated patient conditions. The conditions investigated include varying stenosis levels ranging from 20% to 70%, blood pressure drop ranging from 3125 Pa/m to 9375 Pa/m, fibrous cap thickness ranging from $25\mu m$ to $300\mu m$, lipid pool location ranging

from the leading to the trailing edge of plaque, lipid pool volume relative to stenosis volume ranging from 24% to 80%, Calcium volume relative to stenosis volume ranging from 24% to 80% and arterial remodeling.

The predicted γ varies with the stenosis severity and indicates that the plaques investigated are prone to rupture at approximately 40-45% stenosis levels. It predicts that high pressure significantly lowers the threshold stenosis rate for plaque rupture. In addition, the plaque potential to rupture increases for relatively thin fibrous cap, lipid core located near the leading plaque shoulder, and dramatically for relative lipid pool volume above 60%. However, calcium deposit has marginal effect on plaque rupture. Overall, the predicted results are consistent with clinical observations, indicating that the γ has the potential to characterize plaque rupture when properly established.

In the appendix, the unsteady flow in a collapsible tube model of a diseased artery is solved analytically. The novelty of our approach is that the set of governing equations is reduced to a single integro-differential equation in the transient state. The equation was solved using the finite difference method to obtain the pressure and compliant wall behavior. The analytical approach is less computer-intensive than solving the full set of governing equations. The predicted membrane deflection is quite large at low inlet velocity, suggesting possible approach to breakdown in equilibrium. As the transmural pressure increases with wall deflection, bulges appear at the ends of the membrane indicating critical stage of stability, consistent with previous studies. An increase in wall thickness reduces the wall deflection and ultimately results in its

collapse. The collapse is due to breakdown in the balance of wall governing equation. An increase in internal pressure is required to maintain membrane stability.

I dedicate this thesis to my late Father, Louis Teuma-Tadjougong, and my sister Carine Teuma

ACKNOWLEDGMENTS

My thanks first go to my thesis advisor, Prof. Olusegun J. Ilegbusi who introduced me to this project. Without his guidance and support during the course of this thesis, the work would not be possible. His uncompromised standards made me reach farther and accomplished more than I had thought was possible.

I would like to thank other faculty members, Prof. David Nicholson and Prof. Alain Kassab (former department chair and former department graduate coordinator, respectively) for first, accepting me into the engineering program, and second, providing me the guidance and encouragement during this research.

I wish to express my great gratitude to Dr. Marco Costa, director of the Division of Cardiology, University of Florida, for giving me the chance to visit his lab at the Shands Hospital, Jacksonville, FL, and see first hand how engineering is applied in medicine. I would also like to acknowledge the contribution from my other thesis committee, Dr. Jannick Rolland and Dr. Samar Kalita, who have provided me useful comments on this project.

My special thanks are due to Dr. Celestin W. Soh for his invaluable contributions to the development of the analytical model of this thesis and Dr. Eduardo Divo for his help on the numerical procedures utilized in the solution. I also want to thank my former colleagues of the

Cardiovascular Research Lab, Hitesh Nanda and Gokmen Demirkaya, for sharing their knowledge and insights with me and making this a fun place to work.

I owe a debt of gratitude to my dear girlfriend, Anne Demigné, for her patience and absolute support during the period of my study. I would also send special thanks to my mother, Praxède Teuma, my brothers Guy and Fabrice and my sisters Danielle and Ines for their multiple encouragements.

TABLE OF CONTENTS

LIST OF FIGURES	xii
LIST OF TABLES	xv
LIST OF ACRONYMS/ABBREVIATIONS	xvi
1. GENERAL INTRODUCTION.....	1
1-1- Overview	1
1-2- Definitions	2
1-2-1 Coronary Artery Disease (CAD).....	2
1-2-2 Initiation of Atherosclerosis	3
1-2-3 Inflammatory Mechanisms.....	3
1-2-4 Mechanical Mechanisms	4
1-2-5 Atherosclerotic Plaque	4
1-2-6 Plaque Disruption.....	8
1-2-7 Consequences	8
1-3- Background	12
1-4- Research Objective.....	14
1-5- Research Tasks.....	16
1-6- References	17
2. LITERATURE REVIEW	18
2-1- Overview	18
2-2- Presentation of the Study.....	19
2-3- Two Dimensional Models	21
2-4- Three Dimensional Models	24
2-5- Another Contributing Factor: Vascular Remodeling	27
2-6- Organization of the Study	30
2-7- References	31
3. MODEL FORMULATION	34
3-1- Geometry.....	34
3-2- Material Properties	35
3-3- Structural Analysis	36
3-4- Flow Analysis.....	42
3-5- Fluid Structure Interaction	44
3-6- References	46
4. ESTABLISHING THE FLUID-STRUCTURE INTERACTION (FSI) INDEX OF PLAQUE RUPTURE.....	48
4-1- Overview	48
4-2- Formulation	48
4-3- Results	48
4-3-1 Fluid-Flow.....	49
4-3-2 Structural Analysis	52

4-3-3 Fluid Structure Interaction (FSI)	58
4-3-3-1. Stress Normalization	58
4-3-3-2. Summary: FSI Indices	61
4-4- Closing Remarks	64
4-5- References	66
5. EFFECT OF BLOOD PRESSURE ON FSI INDEX OF PLAQUE RUPTURE	68
5-1- Overview	68
5-2- Formulation	70
5-3- Results	72
5-3-1 Fluid-Flow Analysis	72
5-3-2 Structural Analysis	76
5-3-3 Fluid Structure Interaction (FSI)	79
5-3-4 Effect of Pressure Drop on FSI Index	81
5-4- Closing Remarks	84
5-5- References	85
6. EFFECT OF PLAQUE COMPOSITION ON FSI INDEX OF PLAQUE RUPTURE	87
6-1- Overview	87
6-2- Formulation	88
6-3- Results	90
6-3-1- Fluid-Flow Analysis	90
6-3-2. Structural Analysis	93
6-3-2-1 Effect of Fibrous Cap Thickness	93
6-3-2-2 Effect of Lipid Pool Location	96
6-3-2-3 Effect of Lipid Pool / Calcium Size	101
6-3-3. Fluid Structure Interaction (FSI)	103
6-3-3-1. Stress Ratios	103
6-3-3-2. Summary: FSI Indices	107
6-4- Closing Remarks	111
6-5- References	113
7. EFFECT OF VASCULAR REMODELING ON FSI INDEX	115
7-1- Overview	115
7-2- Formulation	115
7-3- Results	116
7-3-1 Flow Analysis	116
7-3-2 Structural Analysis	117
7-3-3 Fluid Structure Interaction Flow Analysis	119
7-3-3-1 Stress Ratios	119
7-3-3-2 Summary: FSI Indices	121
7-4- Closing Remarks	123
7-5- References	124
8. GENERAL CONCLUSION AND RECOMMENDATIONS	125
8-1- Overview	125
8-2- Establishing the Fluid- Structure Interaction (FSI) Index of Plaque Rupture	126
8-3- Effect of Blood Pressure on FSI Index	127

8-4- Effect of Plaque Composition on FSI Index	128
8-5- Effect of Artery Remodeling on FSI Index	129
8-6- Summary of the Results	130
8-7- Recommendations	132
8-7- References	134
APPENDIX ANALYSIS OF UNSTEADY FLOW IN A CONSTRICTED COLLAPSIBLE	
TUBE MODEL OF A DISEASED ARTERY	
A-1- Summary	137
A-2- Literature Review	138
A-2-1 Presentation of the Study.....	138
A-2-2- One Dimensional Analysis.....	141
A-2-3- Two Dimensional Analysis.....	141
A-2-4- Thee Dimensional Analysis	143
A-2-5- Organization of the Analytical Study.....	145
A-3- Method.....	147
A-3-1- Overview	147
A-3-2- Geometry.....	148
A-3-3- Governing Equations – Fluid Flow.....	150
A-3-4- Governing Equations – Artery Wall	156
A-3-5- Numerical Solution	161
A-4-Results	164
A-4-1- Variation of the Inlet Velocity	166
A-4-2- Variation of the Inlet Transmural Pressure	170
A-4-3- Variation of the Wall Thickness h	172
A-4-4- Closing Remarks	176
A-5- Conclusion and Recommendations	177
A-5-1- Conclusion	177
A-5-2- Recommendations.....	178
A-6- References	180

LIST OF FIGURES

Figure 1.1: Atherogenesis: Differentiation of monocytes into macrophages & LDL implication. MD, Ph.D. presentation, Baylor College of Medecine, 2001).....	7
Figure 1.2: Normal heart- anterior view (a), Myocardial infarction (Ischemia) (b) [8]	9
Figure 1.3: Plaque disruption: (a) Normal arteries, (b) Fatty streaks begin in childhood and develop into atheromas (fat and cell debris), (c) Plaque rupture and thrombus formation [8]. (d) Clot and fatty deposits in the artery [1].....	10
Figure. 1.4: Spectrum of atherosclerosis, from Doherty et al.[9], green arrow indicates thrombosis occlusion, dark arrow indicates small intraplaque hemorrhage and white arrows indicate ruptured cap.....	11
Figure 1.5: Schematic representation of atherosclerosis of internal carotid artery (http://health.allrefer.com/pictures-images).....	12
Figure 1.6: Cardiovascular diseases (source AHA) [1]	14
Figure. 2.1: Bar Graphs showing stenosis severity, coronary occlusion and myocardial infarction (MI) [2]	20
Figure 2.2: 2-D model of 70 % stenosis plaque with 0.25 mm cap thickness and lipid pool 38% of plaque thickness (a). and circumferential stress pattern (b) [6].....	22
Figure 2.3: Arterial model with stenosis made of hydrogel enclosing a lipid pool (a), and maximum principal stress pattern using FSI (b) [15].	25
Figure 2.4: Manifestations of arterial disease [16] and representation of an occluding thrombus [20]. CAD denotes Coronary Artery Disease.	27
Figure 2.5: Outward and inward remodeling mechanisms; Putative effect on plaque rupture [21]	29
Figure 3.1: Schematic representation of stenosed artery model	35
Figure 3.2: Typical bi-linear strain-stress curve	36
Figure 3.3: Representation of principal stresses and principal directions [17].....	38
Figure 3.4: Von Mises stress and Maximum shearing stress [18]	39
Figure 3.5: Buckling of ideal slender column.....	40
Figure 3.6: Buckling configuration of thin-walled cylinder subjected to radial pressure	41
Figure 3.7: Pressure acting on stenotic plaque.....	41
Figure 4.1: Flow velocity profile and flow re-circulations (small arrows).....	49
Figure 4.2: Endothelial shear stress (SS) distribution along the solid-liquid interface for different stenosis levels.....	51
Figure 4.3: (a) Maximum Principal Stress (MPS) and (b) Von Mises Stress (VMS) band plots. 54	
Figure 4.4: Maximum Principal Stress (MPS) and Von Mises Stress (VMS) distributions.....	55
Figure 4.5: Maximum principal stress (MSS) and lateral (circumferential) stress (SZZ) distributions.....	56
Figure 4.6: Stress ratio R_1 and R_2 distributions	59
Figure 4.7: Stress ratio distributions R_3 and R_4	60
Figure 4.8: FSI indices R_{1_mon} (or γ) and R_{4_mon} as a function of stenosis rate	63
Figure 5.1: Flow velocity and flow re-circulations for 40% stenosis	73

Figure 5.2: Flow velocity and flow re-circulations for 70% stenosis	74
Figure 5.3: Endothelial Shear stress distribution along the solid-liquid for 40 % Stenosis.....	75
Figure 5.4: Maximum principal stress (MPS) distribution within the plaque for 40% St., and for $\Delta P_L = 3125$ Pa/m and $\Delta P_L = 5937$ Pa/m.....	76
Figure 5.5: Von Mises stress (MPS) distribution within the plaque for 40% St., and for $\Delta P_L = 3125$ Pa/m and $\Delta P_L = 5937$ Pa/m.....	77
Figure 5.6: Maximum principal stress (MPS) and Von Mises stress (VMS) for 40% stenosis. ..	78
Figure 5.7: Stress ratios R_1 and R_2 along the segment for 40 % Stenosis.	80
Figure 5.8: The FSI index as a function of stenosis rate and pressure.....	82
Figure 6.1: Schematic representation of stenosed artery model	88
Figure 6.2: Typical flow velocity and flow re-circulations	90
Figure 6.3: Endothelial Shear Stress (SS) plots for different stenosis rates	92
Figure 6.4: Maximum Principal Stress (MPS) distributions for different Fibrous cap thickness, t	93
Figure 6.5: Von Mises Stress (VMS) distributions for different Fibrous cap thickness, t	94
Figure 6.6: Maximum Principal Stress (MPS) (a) and Von Mises Stress (VMS) (b)distributions for different fibrous cap thickness, t . $t = 25 \mu m$, $100 \mu m$ and $300 \mu m$	95
Figure 6.7: Model of stenosis. Direction of LP shifting in the stenosis (Arrow)	97
Figure 6.8: Maximum Principal Stress (MPS) distributions for models with different lipid pool positions: 102.5 mm (a), 105.5 mm (b) and 107.5 mm (c).....	98
Figure 6.9: Von Mises Stress (VMS) distributions for different lipid pool location 102.5 mm (a), 105.5 mm (b)and 107.5 mm (c).	99
Figure 6.10: Maximum Principal Stress (MPS) (a) and Von Mises Stress (VMS) (b) distributions for different lipid pool location in 40% stenosis model.....	100
Figure 6.11: Maximum Principal Stress (MPS) (a) and Von Mises Stress (VMS) (b) distributions for different lipid pool volume rate (LPr).....	101
Figure 6.12: Maximum Principal Stress (MPS) (a) and Von Mises Stress (VMS) (b) distributions for for different calcium volume rates	103
Figure 6.13: Typical Stress Ratio R_1 and R_2 for two fibrous cap thicknesses, t	104
Figure 6.14: Typical Stress Ratio R_1 and R_2 for two lipid pool locations, X	105
Figure 6.15: Typical Stress Ratio R_1 and R_2 for two lipid pool volume rates, LPr.....	106
Figure 6.16: Typical Stress Ratio R_1 and R_2 for two calcium volume rates, Ca.....	107
Figure 6.17: FSI index γ as a function of fibrous cap thickness	108
Figure 6.18: FSI index γ as a function of lipid pool location within the stenosis	109
Figure 6.19: FSI index γ as a function Lipid pool / Calcium percentage of total stenosis volume	110
Figure 7.1: Schematic sketch of arterial segments with inward (a) and outward (b) remodeling	116
Figure 7.2: Maximum Principal Stress (MPS) and Von Mises Stress (VMS) distributions for Inward Remodeling (I.R.) and Outward Remodeling (O.R.) cases	117

Figure 7.3: Ratios R_1 and R_2 with $P_{out} = 0$ Pa for Inward Remodeling (I.R.) and Outward Remodeling (O.R.) cases	120
Figure 7.4: FSI index γ as a function of stenosis rate for OR and IR.....	122
Figure A.1: 3D Collapse and buckling of a tube. External compression increases and tube wall progressively collapses from panel (a) to panel (d) [5]	139
Figure A.2: Wall motion using the lubrication flow theory for different control parameters [13], Note that, t the non-dimensional coordinate of the collapsible channel and δ the non-dimensional position inside the collapsible segment channel. The parameter m_o is related to the wall thickness, m_1 to the segment length, m_2 to the pressure at the inlet.	143
Figure A.3: 2-D model of collapsible channel.....	149
Figure A.4: Segment of channel wall	149
Figure A.5 Average velocity profile of pulsatile flow applied at the inlet and $\frac{1}{2}$ distance of the model length.....	165
Figure A.6: Wall shape as the inlet velocity U_o increases from 0.1m/s (a) to 0.2m/s (b) to 0.3m/s (c).	167
Figure A.7: Typical velocity profile at time $t=0.1$ shows that the flow is fully developed throughout the channel.....	168
Figure A.8: (a) the wall shear stress distribution and (b) pressure distribution for inlet velocity range from 0.1 m/s to 0.3m/s	169
Figure A.9: Wall shape as the inlet transmural pressure, tP increases from 180 Pa (a) to 200 Pa (b) to 220 Pa (c).	171
Figure A.10: (a) the wall shear stress distribution and (b) pressure distribution for inlet transmural pressure of 180 Pa, 200 Pa and 220 Pa.....	172
Figure A.11: Wall shape as the wall thickness increases from 0.7 mm (a) to 0.8 mm (b) to 0.9 mm (c).....	174
Figure A.12: (a) the wall shear stress distribution and (b) pressure distribution for wall thickness varying from 0.7 mm to 0.9 mm.....	175

LIST OF TABLES

Table 1.1 Cardiovascular disease statistics from the American Heart Association (AHA) [1]....	13
Table 3.1 Principal input parameters used for the computation	37
Table 5.1 Blood pressure values used at inlet of arterial segment.....	71
Table 6.1 Cases investigated versus parameter values	89
Table 8.1 Summary of relevant literature and present study	130
Table A. Input data utilized in this study.....	164

LIST OF ACRONYMS/ABBREVIATIONS

<i>Acute coronary syndrome</i>	partial or complete occlusion of coronary arteries
<i>Atherosclerosis</i>	The progressive narrowing and hardening of the arteries over time.
<i>Atherosclerotic plaque</i>	Occurrence of thickening and hardening of arteries
<i>Biomechanical stress</i>	Structural stress in a biological tissue (i.e. Artery wall)
<i>Buckling</i>	Sudden deflection associated with unstable equilibrium and resulting in total collapse of the member
<i>CAD</i>	Coronary Artery Disease
<i>Calcium volume rate or Φ_{Ca}</i>	Calcium volume relative to stenosis volume
<i>CVD</i>	Cardiovascular disease
<i>Endothelial shear stress</i>	Shear stress occurring on the inner surface of blood vessel
<i>FSI</i>	Fluid-Structure Interaction
<i>HBP</i>	High Blood Pressure
<i>Hemodynamic stress</i>	Stress deriving from the blood flow in the artery channel
<i>Lipid pool volume rate or Φ_{lp}</i>	Lipid pool volume relative to stenosis volume
<i>LPr</i>	Lipid pool volume rate or Φ_{lp}
<i>M.I.</i>	Myocardial Infarction (see Fig. 1.2 b)
<i>MPS</i>	Maximum Principal stress
<i>MSS</i>	Structural shearing stress
<i>Myocardial Infarction</i>	Heart failure or heart attack, stroke, occlusion of coronary arteries
<i>Plaque shoulder</i>	Segion where stenotic plaque meets the normal arterial wall

<i>SS</i>	Endothelial shear stress
<i>Stenosis rate</i>	Percent stenosis relative to interior artery diameter
<i>Stenosis severity</i>	(see Stenosis rate)
<i>Stenosis</i>	Fatty build-ups in the arteries
<i>Stenotic plaque</i>	see <i>Atherosclerosis</i>
<i>SZZ</i>	Lateral stress (reminiscent of circumferential stress or hoop stress)
<i>Thrombosis</i>	The formation, development or presence of a aggregation of blood factors, primarily platelets and fibrin with entrapment of cellular elements, frequently causing vascular obstruction at the point of its formation (see Fig. 1.4)
<i>VMS</i>	Von Mises stress

1. GENERAL INTRODUCTION

1-1- Overview

Coronary artery disease (CAD) is the leading cause of death in the developed world [1]. It is known as silent killers. Indeed they remain asymptomatic until the patient suffers a heart attack. Hence, the necessity to device methods for early diagnosis and better treatment.

There has been a remarkable decline in myocardial infarction (heart-attack) or stroke in recent years due to advanced diagnostic methods (MRI, CT scan, OCT...), adapted treatments and lifestyle adjustments (diet, exercises...). However, more research is needed to fully understand the genesis and progression of CAD.

Heart attack is generally caused by a partial or complete occlusion of coronary arteries. The occlusion or plaque is composed primarily of fatty deposits. Increased biomedical stresses on the diseased arterial wall may lead to plaque rupture, resulting in myocardial infarction. Therefore, coupled hemodynamic and structural stress analyses are pivotal to understanding plaque stability and vulnerability to rupture. In particular, investigating the correlation between different stages of plaque formation and patterns of mechanical stress may help to detect vulnerable stenosis in patients.

1-2- Definitions

This section presents definitions of common biomedical words and terms used in describing coronary artery disease (CAD) and, the principles and processes of initiation, growth and disruption of coronary plaque.

1-2-1 Coronary Artery Disease (CAD)

CAD, also called Atherosclerosis, is a form of arteriosclerosis, which is the occurrence of thickening and hardening of arteries. It is the process by which the coronary arteries become narrowed or completely occluded. It is the underlying cause of ischaemia (lack of oxygen to heart cells) and, ultimately, of heart attack.

The atherosclerotic plaque is made of fatty build-ups in the arteries. Its location in the blood stream varies with the patient. The fatty deposits grow slowly and often start at childhood. CAD is a predominantly asymptomatic disease and can progress rapidly in some people to become life threatening as early as in their thirties.

1-2-2 Initiation of Atherosclerosis

Atherogenesis or formation of atheroma (fatty deposits) often starts in the early years after birth. It spreads out through the artery blood stream. It is generally assumed that atherosclerotic plaque occurs through two mechanisms: inflammatory and mechanical [2].

1-2-3 Inflammatory Mechanisms

Artery inflammatory may be attributed to two factors: endothelium lesion and endothelium dysfunction. Hypertension, infections, free radicals, diabetes are cited as possible cause of the symptoms. However, the main cause of endothelium lesion is the low-density lipoproteins (LDL) or “bad cholesterol”. This statement stems from the fact that the elevated levels of LDL in blood is found in more than half of the population affected with a form of CAD [2].

The LDL can get trapped in areas of retrograde flow or low shear stress in the artery. Then it undergoes oxidation and gets swallowed by macrophages due to the receptors on their surface. Then macrophages progress to become foam cells. Therefore, a reduction of modified LDL and increase of anti oxidants like vitamin E have an anti-inflammatory effect.

1-2-4 Mechanical Mechanisms

Hemodynamic studies have shown that stenosis is typically located in regions of the artery where flow velocity gradient or shear stress is low [3]. Low shear stress locations favor the sticking of particles and monocytes to the endothelial layer due to the high residence times [4]. These particles tend to remain in the area over several cardiac cycles, exposing the area to increased contact to the endothelial chemical reactions favoring their infiltration into the arterial wall.

1-2-5 Atherosclerotic Plaque

Stenotic plaques partly result from fatty deposits caused by hemodynamic and inflammatory factors as described previously. Besides these fatty accumulations, there are other molecules that play important roles in plaque build-up and rupture. These molecular components are listed and described below.

1-2-5-a *Calcium*: contributes to stiffening and stretching of the arterial wall. Arterial wall calcification has always been associated with severe stenosis. It has been shown that calcium does not improve plaque stability [5].

1-2-5-b *Collagen*: Originates from Greek word “Kolla” meaning, “glue” and “Genna” meaning “to produce”. It is a protein substance of the white fibers of all connective tissues such as skin, tendon, bone, and cartilage. It is non-uniformly distributed in the plaque and contributes to local hardening of the plaque [6].

1-2-5-c *Endothelial cells*: Thin flattened cells lining the inside surfaces of blood vessels. Their lesions or dysfunctions are the principal cause of plaque development.

1-2-5-d *Low-Density Lipoproteins (LDL)*: Proteins that act as carriers for cholesterol and fats in the bloodstream. They are involved in the initiation of the atherosclerotic plaque. LDL level over 130-160 mg/dl is considered as positive risk factor for the development of CAD.

1-2-5-e *Macrophages*: Small, active white blood cells specializing in engulfing, killing and digesting foreign bodies in the blood stream. They can assault collagen and then weaken the plaque locally.

1-2-5-f *Metalloproteinase (MMP)*: Enzymes that utilize metal in the catalytic mechanism (accelerating chemical reaction without being consumed or changed). MMP is always associated with plaque rupture.

1-2-5-g *Monocytes*: Mononuclear phagocytes circulating in the bloodstream that will later emigrate into tissue and differentiate into macrophages. In Vascular smooth muscle cells they favor MMP-1 and MMP-3 secretion.

1-2-5-h *Platelets*: Discoid cells found in large number in blood. They are important for blood coagulation and reparations of breaches in the walls of blood vessels.

1-2-5-i *T-Cells*: Also called *T-Lymphocytes*, coordinate the immune system by secreting growth factors called lymphokine hormones. Their activations by macrophages or vascular smooth muscle cells through oxidized LDL result in secretion of cytokines which stimulate inflammatory response. Thereby they favor disruption of the lesion.

1-2-5-j *Vascular smooth muscle cells (VSMC)*: Found in blood vessel walls. They contribute largely to mechanical properties of the artery.

1-2-5-k- *Atheroma*: A disease characterized by thickening and fatty degeneration of the inner coat of the artery.

1-2-5-l *Fibrous cap*: Fibrous envelope of the fatty deposits inside the arteries. Consisting mainly of smooth muscle cells, it is a thin layer of connective tissue covering the lipid pool. It is characterized by different degrees of infiltration by macrophages [7] and its thickness largely varies with stenosis.

Figure 1.1 summarizes the different stages of atherogenesis [2]. The first step is an attachment of Leukocytes (monocytes) to the intact endothelium in response to hypercholesterolemia. Then, once adherents, Leukocytes penetrate from the endothelial surface into the arterial intima where they differentiate into macrophages. Macrophages produce variety of chemicals, including cytokines, and also phagocyte lipids (modified/oxidized LDL) to become foam cells. Macrophages and foam cells secrete growth factors and matalloproteinases. Growth factors promote cells proliferation and matrix production, where as matalloproteinases promote matrix degeneration. At this step, all the cell types necessary for the inflammatory process that leads to atherosclerotic plaques are present.

Note that monocytes/macrophages, T-Lymphocytes are associated with inflammatory leukocytes (natural immune system).

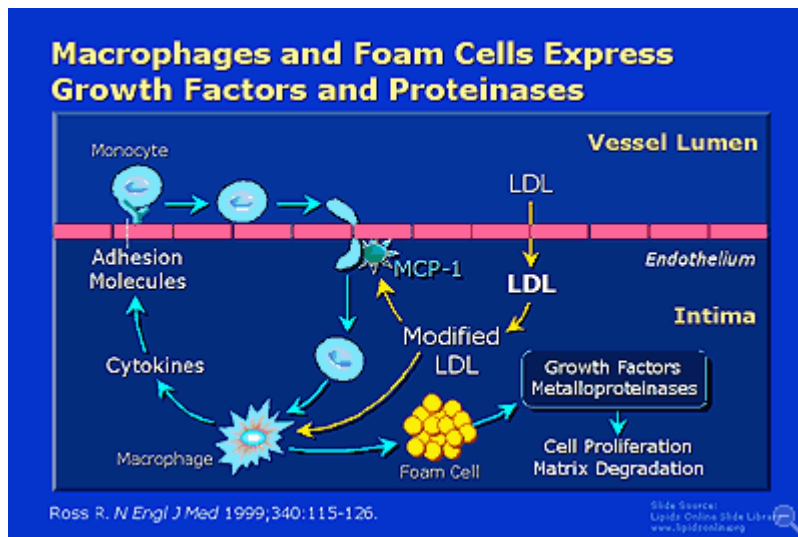


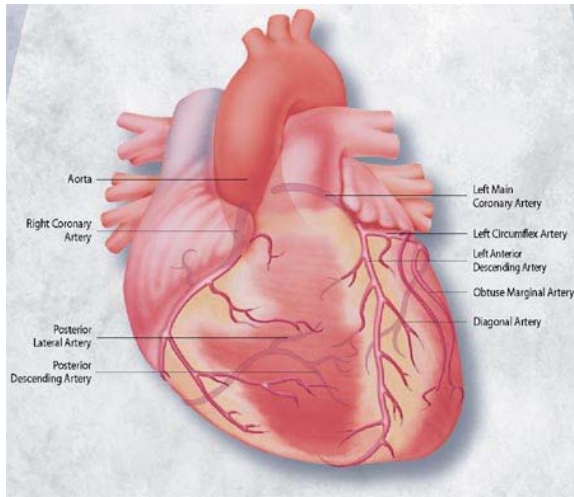
Figure 1.1: Atherogenesis: Differentiation of monocytes into macrophages & LDL implication. MD, Ph.D. presentation, Baylor College of Medicine, 2001)

1-2-6 Plaque Disruption

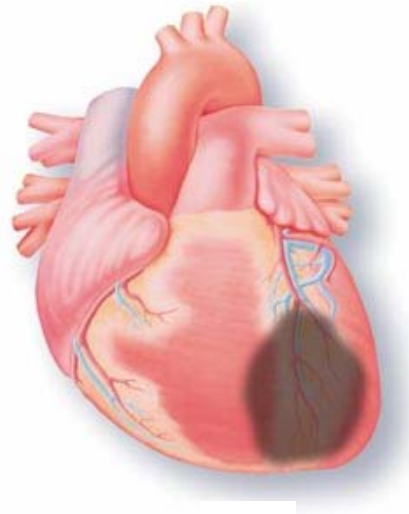
Unstable plaque is usually characterized by a non-uniform, thin and eccentric fibrous cap, accompanied by large lipid pool [7]. Plaque disrupts mainly on its shoulders, that is, locations where the fibrous cap is thinned-out due to macrophage activities [7]. The plaque shoulders have been found to be propitious sites for macrophages accumulation and infiltration [2]. There are critical stages in the progress of the disease which could lead to a thrombus. Although in the past decade intensive studies have shed light on some of these stages [2], the exact mechanism that causes unstable atheroma is not yet fully understood.

1-2-7 Consequences

Atherosclerotic plaque is continuing to be of major research interest in order to fully understand its mechanism. Coronary lesion can progress and remain stable for decades, with intervals of chest pains as the most noticeable complaint due the reduced oxygen supply to the heart. Moreover, ischemia does not always result in irreversible damage. Two things can occur when plaque ruptures, namely, the formation of a blood clot (thrombus) on the plaque surface and bleeding (hemorrhage) into the plaque. Depending on the magnitude, either of these occurrences can entirely block the artery and thereby suppress the oxygen supply to the heart muscle (See Fig. 1.2 & 1.3). A heart attack is the ultimate clinical outcome. Similarly, if the oxygen supply to the brain is suppressed, a stroke may occur.



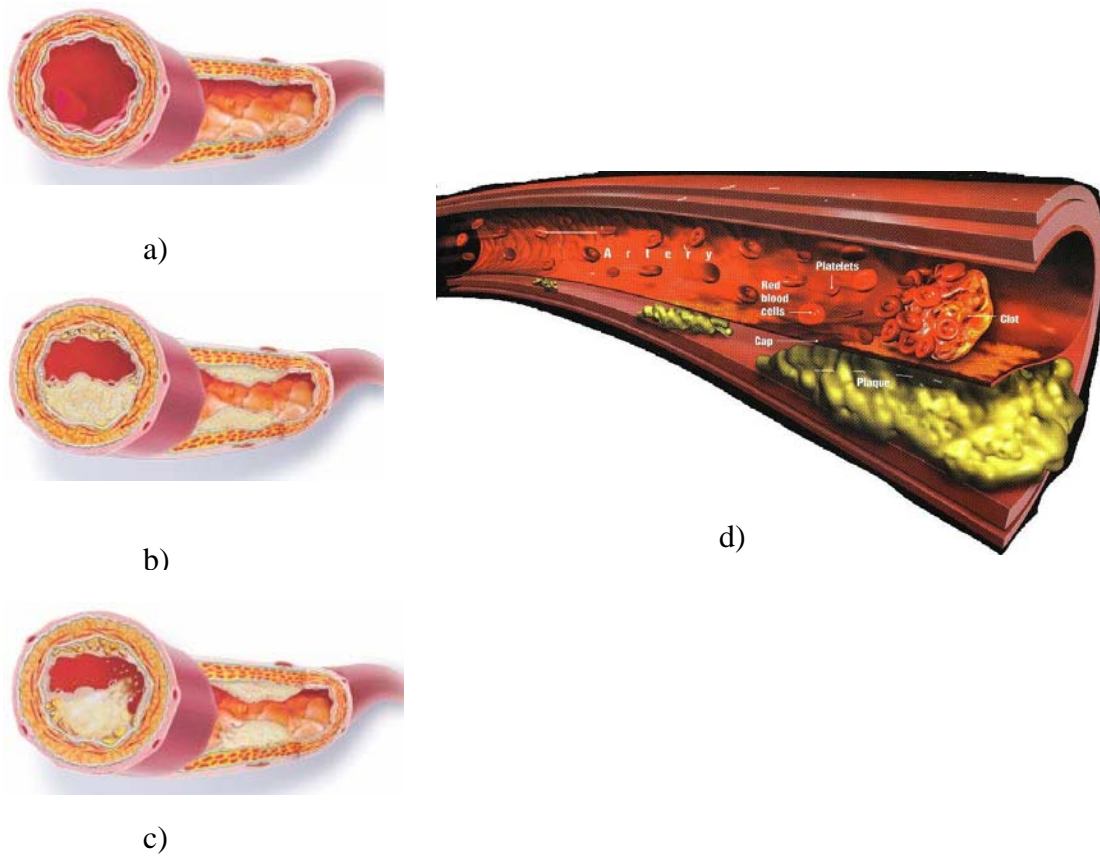
(a)



(b)

Figure 1.2: Normal heart- anterior view (a), Myocardial infarction (Ischemia) (b) [8]

A schematic representation of coronary arteries and plaque deposits in the artery are presented in the following figure.



A

Figure 1.3: Plaque disruption: (a) Normal arteries, (b) Fatty streaks begin in childhood and develop into atheromas (fat and cell debris), (c) Plaque rupture and thrombus formation [8]. (d) Clot and fatty deposits in the artery [1].

Figure 1.4 presents a spectrum of atherosclerotic plaque [9]. It shows the different stages of plaque growth from its nascent to rupture. In the figure, A is the scanning electron micrograph of an intact endothelial layer, with intimal lesion. B shows a segment of aorta from a 5-year-old child obtained during autopsy. The aorta surface is covered with fatty dots. C shows the positive remodeling of arterial wall in reaction to plaque growth in which helps to maintain normal blood flow. D shows a large thrombus adhering to the luminal arterial surface which was caused by the

endothelial erosion or tearing of the fibrous cap. E shows intra-plaque bleeding that may compromise luminal diameter leading to ischemia. In F, we see a complete thrombotic occlusion (dark). In G, is shown thrombotic occlusion similar to that seen in F with presence of large, lipid-filled lesion. In H, the white arrows show the ruptured cap.

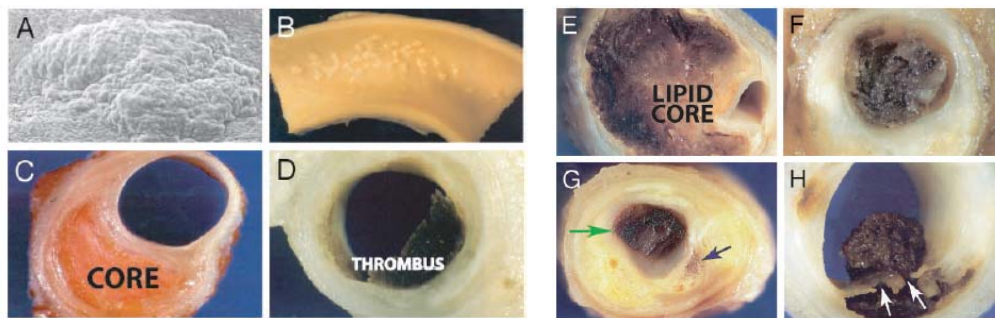


Figure. 1.4: Spectrum of atherosclerosis, from Doherty et al.[9], green arrow indicates thrombotic occlusion, dark arrow indicates small intraplaque hemorrhage and white arrows indicate ruptured cap

Atherosclerotic plaques also affect Carotid arteries. Carotid arteries are the two large blood vessels on each side of the neck as shown in Fig.1.5. Carotid artery stenosis occurs following a similar mechanism as coronary artery stenosis with fatty buildup narrowing and eventually blocking the passageway. It is one of the causes of stroke, which occurs when the brain suffers from lack of oxygen due to the reduction of blood flow in the carotid arteries. It ultimately results in sudden loss of brain function.

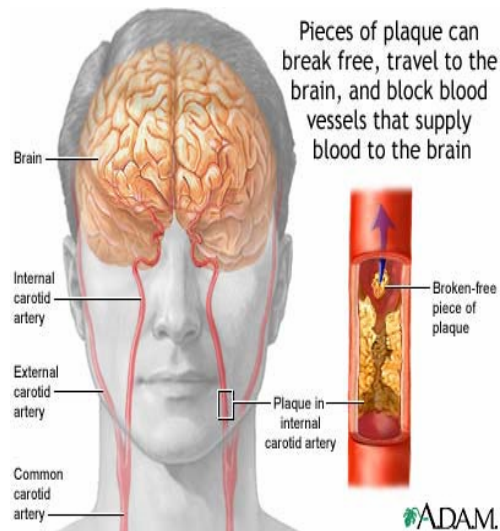


Figure 1.5: Schematic representation of atherosclerosis of internal carotid artery (<http://health.allrefer.com/pictures-images>)

1-3- Background

According to the American Heart Association [1], 70,100,000 Americans were affected with one or more types of cardiovascular disease (CVD) in 2002. The disease represents 38 percent of all deaths or 1 in every 2.6 deaths in the USA. Among those fatalities, 53% resulted from Coronary Heart Disease (CHD) and 18 % from stroke. Indeed, CHD is the single largest killer of American males and females with 656,000 deaths in 2002 and, just after cancer, stroke is the third major cause of mortality with 275,000 deaths [1]. These data are summarized in Table 1.1 and Figure 1.6 below.

Table 1.1 Cardiovascular disease statistics from the American Heart Association (AHA) [1]

Population Group	Prevalence 2002	Mortality 2002#	Hospital Discharges 2002	Cost 2005
Total population	70,100,000 (34.2%)	927,448	6,373,000	\$393.5 billion
Total males	32,500,000 (34.4%)	433,825 (46.8%)*	3,209,000	—
Total females	37,600,000 (33.9%)	493,623 (53.2%)*	3,164,000	—
White males	34.3%	375,392	—	—
White females	32.4%	428,461	—	—
Black males	41.1%	48,993	—	—
Black females	44.7%	56,721	—	—
Mexican-American males	29.2%	—	—	—
Mexican-American females	29.3%	—	—	—

Note: (—) = data not available.

* These percentages represent the portion of total mortality that is males vs. females.

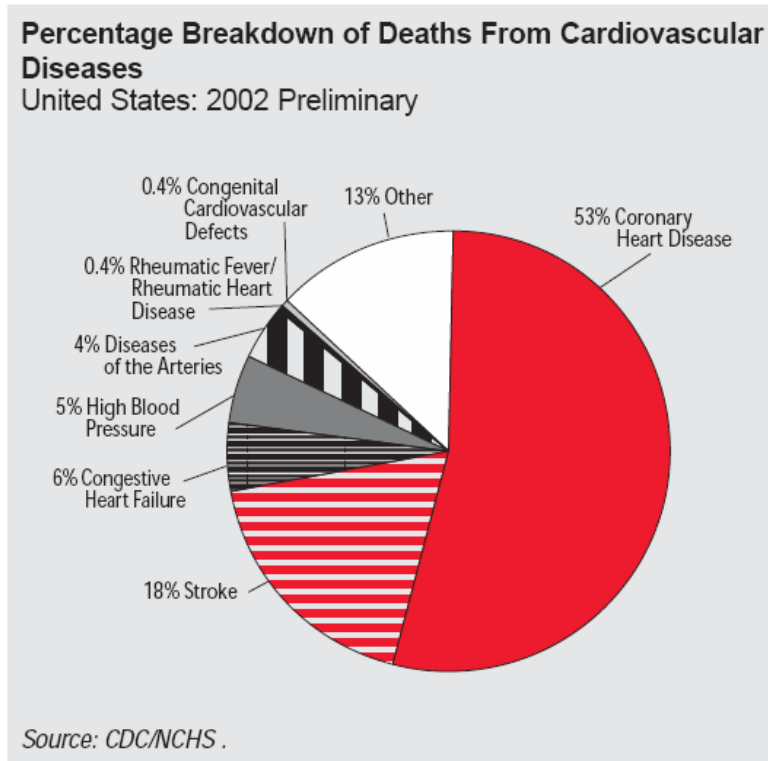


Figure 1.6: Cardiovascular diseases (source AHA) [1]

Equally disturbing is that, 50 percent of men and 64 percent of women who died suddenly of CHD had no previous symptoms of this disease [2]. There was, however, a steady decline of 26% in the death rates from 1992 to 2002 due to more advanced diagnostic methods, adapted treatments and changes in modern lifestyle [1].

1-4- Research Objective

Our research broadly focuses on the mechanism of atherosclerotic plaque stability and vulnerability to rupture. The research integrates image data acquisition of the inner morphology of coronary diseased artery, 3-D image reconstruction of the artery and coupled flow and structural analyses for disease characterization.

The present study focuses on biomechanical plaque behavior in models of human coronary artery segments. The objective is to apply numerical fluid-structure interaction models to these arterial segments derived from images of longitudinal cross-sections available in the literature. *The predicted endothelial shear stresses and structural stresses will be analyzed to define a unique index γ of plaque rupture.*

In addition, such fluid-structural analyses of the influence of plaque morphology on plaque propensity to rupture could be used to validate existing clinical observations and provide new perspectives for further research.

1-5- Research Tasks

The following specific tasks are followed to achieve the objectives described above:

Task 1. Develop the Fluid-structure interaction (FSI) model of diseased coronary artery and implement it in a numerical scheme.

Task 2. Apply FSI to define an index of plaque rupture potential.

Task 3. Characterize the effect of blood pressure on plaque propensity to rupture using FSI model.

Task 4. Investigate the effects on plaque propensity to rupture of plaque characteristics including fibrous cap thickness, lipid core size, calcium layer size and the relative location of the lipid pool in the stenosis model.

Task 5. Investigate the impact of vascular remodeling on FSI index of plaque rupture

1-6- References

- [1] American Heart Association, American Stroke Association, “Heart Disease and Stroke Statistics” 2005 update
- [2] Ross R., 1999, “Atherosclerosis – an Inflammatory Disease” *N. Engl J Med.* (340); 2:115-126.
- [3] A. U. Coskun, Y. Yeghiazarians,, et al. “Reproducibility of Coronary Lumen, Plaque, and Vessel Wall Reconstruction and of Endothelial Shear Stress Measurements in Vivo in Humans”, *Catheterization and Cardiovascular Interventions* 60:67-78 (2003)
- [4] Zhenjun Hu “In ViVo Characterization of Human Coronary Artery Flow”, Ph.D. Thesis, Northeastern University 2000
- [5] Huang H., Virmani R., Younis H., Burke A.P., Kamm R.D., and Lee R.T.,2001, “The impact of calcification on the biomechanical stability of atherosclerotic plaques”. *Circulation*, 103, 1051–1056.
- [6] Richardson PD, “Biomechanics of the Plaque Rupture: Progress, Problems and New Frontiers”, *Annals of Biomedical Engineering* (2002), 524-536
- [7] Erling Falk, Prediman K. Shah, Valentin Fuster, “Coronary Plaque Disruption”, *Circulation*. 1995; 92: 657-671
- [8] MerckSource, 2003, trademark of Merck & Co., Inc.
- [9] Doherty M. T., Fitzpatrick A. L, et al., “Molecular, Endocrine, and Genetic Mechanisms of Arterial Calcification”, 2004, *Endocrine Reviews* 25 (4):629-672

2. LITERATURE REVIEW

2-1- Overview

Understanding of the diverse conditions contributing to fibrous cap vulnerability will help to predict and detect plaques that are susceptible to rupture. Extensive research has been done either in flow analysis or structural analysis of atherosclerotic plaque. However, new approach involving Fluid-structure interaction (FSI) has shown promising results in explaining the mechanism leading to acute clinical events. In this section, we focus on literature relevant to numerical studies of FSI models applied to a diseased arteries and other clinical phenomenon contributing to plaque ruptures.

2-2- Presentation of the Study

Plaque rupture with superimposed thrombosis is the primary cause of acute coronary syndromes of unstable angina, myocardial infarction, and sudden deaths [1]. About 68 % of myocardial infarction (MI) patients have moderate stenoses (less than 50% stenosis), as shown in Fig. 2.1, meaning they had no or little symptom prior to heart attack [2, 3].

This finding motivated further study to explore the possible mechanisms that are responsible for the sudden change of a stable atherosclerotic plaque to an unstable and life-threatening atherothrombotic lesion, known as plaque tearing or disruption. The study focused on the silent growth of the disease, its sudden complication to life-threatening thrombosis, and its composition and vulnerability rather than the stenosis volume or stenosis severity as the most determinant in thrombus formation. Thus, the study clinically assessed the type of plaques that could progress to occlusion and the others that were likely to become culprits, that is, a plaque becoming vulnerable to disruption and/or thrombosis. Less obstructive plaques were found to be more lipid-rich and vulnerable to rupture than larger plaques. Furthermore, the smaller rather than the larger plaques were more likely to lead to acute clinical events in case of abrupt occlusion because they were less frequently associated with preventive consideration. The findings of this study suggest that plaque tearing tends to occur at the locations where the fibrous cap is thinned-out and most vulnerable, and plaque surface is weakest. These locations are coincident with the regions of the stress concentrations resulting from biomechanical and hemodynamic forces.

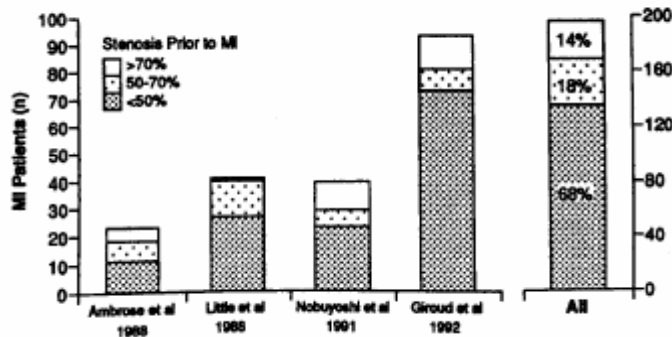


Figure. 2.1: Bar Graphs showing stenosis severity, coronary occlusion and myocardial infarction (MI) [2]

Using results from pathoanatomic examination of plaques and in vitro mechanical testing of isolated fibrous caps from aorta, Falk et al. [2] summarized the vulnerability of plaque to rupture as being dependent on:

- 1- Size and consistency of atheromatous core
- 2- Thickness and collagen content of the fibrous cap covering the core
- 3- Inflammation within the cap
- 4- “Cap fatigue”. Repetitive cyclic stresses may over time weaken the fibrous cap and increase its vulnerability to fracture, ultimately leading to sudden mechanical failure.

Supporting the observations presented above, angiography studies conducted by Fuster et al. [4] demonstrate that most lesions responsible for myocardial infarction were not severe stenosis before rupture. This observation credits the fact that many patients had no prior history of ischemia [2].

It has been established that critical biological factors also contribute to fibrous cap rupture. Lee [5] listed these factors to include matrix-degrading enzymes, which are abundant in the atherosclerotic tissue, inflammatory cells, vascular smooth muscle cells and macrophages, mechanical stimuli and cytokines. Low-density lipoprotein cholesterol (LDL) in the lesion is pivotal in the expressions of those factors, consistent with clinical successes of cholesterol-lowering therapies [5].

2-3- Two Dimensional Models

Among the other determinants of plaque vulnerability, structural stress is essential in understanding the stenosis tearing mechanism. Increased biomechanical stresses in the arterial wall can lead to rupture of the fibrous cap and subsequently, myocardial infarction or stroke. By investigating the correlation between different stages of plaque formation and patterns of mechanical stress, vulnerable plaques may be identified and treated before they rupture.

In recent years, two-dimensional stenosis models have been studied in which important plaque constituents were probed. Predicting subintimal plaque structural features such as thickness of fibrous cap may play a key role on plaque disruption compared to stenosis severity; Loree et al. [6] investigated circumferential stress distribution in the lesion. Finite element analysis was performed on two-dimensional cross-section segments containing a lipid pool and morphology similar to those obtained from intravascular ultrasound images of diseased vessels as shown in Fig. 2.2. The material was assumed orthotropic with linear elastic properties. Using a mean luminal internal pressure of 110 mm Hg, the results indicated that the increase of the stenosis

severity by increasing the fibrous cap thickness reduced the maximum circumferential stress normalized to luminal pressure in the stenosis.

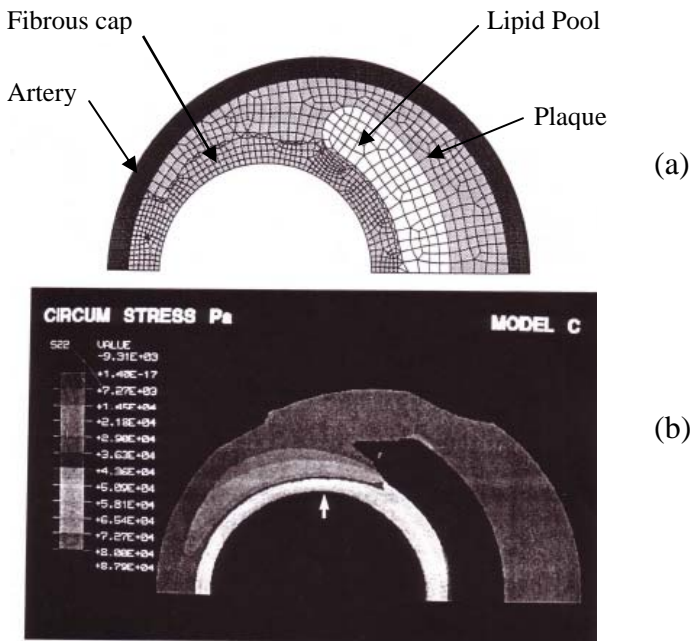


Figure 2.2: 2-D model of 70 % stenosis plaque with 0.25 mm cap thickness and lipid pool 38% of plaque thickness (a). and circumferential stress pattern (b) [6]

Following the approach of Loree [6] approach, Cheng et al. [7] investigated possible correlations between sites of plaque rupture and high circumferential stress in the diseased vessels. Thus, 24 coronary vessel specimens were selected comprising 12 coronary segments that caused lethal myocardial infarction and 12 stable segments for control. A finite element model was used in the study and a mean intraluminal pressure of 110 mm Hg. The results suggest that lethal lesions have the highest percentage of occurrence of plaque rupture in the region of maximum

circumferential stress in the stenosis. This result implies that plaque tearing may not only be related to the site of highest stress, but also to the material properties of the plaque.

Previous studies have typically assumed linear material properties. However, it has been established that soft tissues in living animals exhibit non-linear stress/strain behaviors [8]. Advances in software development have made it possible to implement complex and realistic material properties in describing arterial walls. Gourisankaran et al [9] investigated possible causes of restenosis and plaque rupture on a diseased artery subjected to balloon dilatation using finite element models. The arterial wall was modeled as hyperelastic and Ogden polynomial of order 4. The stress contours over the crescent-shape plaque model obtained from the study showed high regions of circumferential stress near the plaque tip, where the coronary plaque is joined with the normal intima.

Later, by scrutinizing in more detail selected plaque components, Huang et al [10] focused on the fibrous cap thickness, lipid pool and calcium volume, which are important determinants of, increased plaque stresses. Simulations were performed on 20 human coronary lesions (10 ruptured and 10 stable lesions), using large-strain finite element analysis, with assumed isotropic, incompressible, Mooney-Rivlin materials. The results indicate that lipid pools dramatically increase stresses but calcification does not decrease the mechanical stability of the coronary plaque.

Previous 2-D numerical models for stenosis were limited by the unrealistic uniform pressure often assumed. Due to the important role of high pulsating blood pressure in atheroma rupture,

fluid-structure interaction (FSI) phenomenon has been acknowledged as critical in simulating blood flow and plaque stability in stenosed arteries [11-12]. Yamagushi et al. [11] used arterial stenosis and abdominal aneurysm models to perform numerical analysis of the plaque and wall motion. The results showed that stress concentrations were found at the edges of the stenosis and were responsible for plaque tearing. In a subsequent study, Yamagushi et al. [12] suggested that the dragging force from fluid flow impacts on the wall compression.

2-4- Three Dimensional Models

Three-dimensional models have been utilized by Tang et al [13-15] using FSI as a basis to perform experimental and numerical investigation of plaque rupture, and to provide new insights on the effects of FSI on strain and stress distributions. A non-linear thick wall model was used to simulate blood flow in diseased carotid arteries in order to assess the physical conditions leading to wall compression and ultimately, occlusion [13]. The wall model was made of PVA hydrogel. The results show that severe stenosis causes considerable compressible stress in the arterial wall and, affects stress localizations and flow characteristics. Maximum compressive stress and maximum tensile stress are localized within the stenosis. In the recent publication, Tang et al. [15] used a similar model but included lipid cores within the stenosis as illustrated in Fig. 2.3. The arterial wall was modeled as a hyperelastic Mooney-Rivlin material. FSI was solved numerically using ADINA [16]. The results show that stress-strain distributions over the plaque are affected by lipid pool size, shape and location of fibrous cap thickness, and the pressure. All numerical results were supported by experiments.

A comprehensive coupling of experimental data with Fluid-Structure Interaction (FSI) modeling is now used to provide a better understanding of cardiovascular mechanical behavior [13-15].

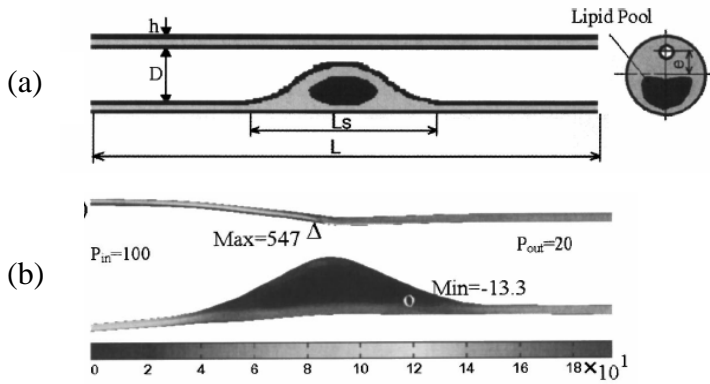


Figure 2.3: Arterial model with stenosis made of hydrogel enclosing a lipid pool (a), and maximum principal stress pattern using FSI (b) [15].

The relationship between plaque morphology and plaque fissure has been a subject of intense interest. Richardson et al [17] investigated the morphological characteristics of plaque that fissure and the sites of fissuring, using 85 stenotic plaques from patients who had died from coronary thrombosis. It was found that 62% of the 67 samples, which contained an eccentric lipid pool in intima, were fissured at the junction of the plaque cap with the normal intima, while 37 % had torn through the center of the cap. Performing computer modeling of the vessel at the systolic phase, it was found that the site of intima tears at necropsy correlated with the region of high circumferential stress. The intraluminal pressures applied during simulation were in the range 70-200 mm Hg. It was speculated that plaque fissuring was closely associated with lipid pool. Moreover, in such stenosis, the lateral margin of the lipid pool is the frequent site of intimal tearing. Fracture can take place where the tensile stress is high but not always at computed site of

maximum stress for the lesion segment. This is due to fissure occurrences and foam cells at the locations. Foam cells are likely to be of macrophage origin. Therefore, this observation suggests that local factors including enzymic degradation of the connective tissue matrix may weaken the intimal layer.

The likelihood of plaque to rupture seems to be a function of the plaque vulnerability, intrinsic factors and external triggers. Internal factors include lipid-rich atheromatous core, thickness of fibrous cap covering the core, and presence of inflammation within the cap. The external factors are mainly the surge in daily activities such as sudden vigorous exercises, emotional stress or cold weather etc. Prediman K. Shah [18] conducted pathoanatomic in vitro studies of intact and ruptured plaques of isolated aortic fibrous caps to characterize plaques that are prone to disruption. By investigating the characteristics that are more prevalent in ruptured plaques, it was found that disrupted plaques tend to have a large, often eccentrically located, soft lipid-rich core that constitutes more than 40% of the plaque volume, and 50 to 60% of plaque disruptions occur on the shoulders of the plaque. The study also indicates that disrupted plaques contain active inflammatory infiltrate commonly found in the fibrous cap and around the lipid core with preferential concentration at the plaque shoulders or underneath the thinned-out sections of torn fibrous cap. Therefore, it was concluded that certain characteristics of plaques, including thickness and composition of fibrous cap, and the presence of a local inflammatory process, foster plaque rupture. In addition, the combination of biomechanical and hemodynamic forces acting on the plaque generates stresses, which trigger plaque disruption as illustrated in Fig. 2.4.

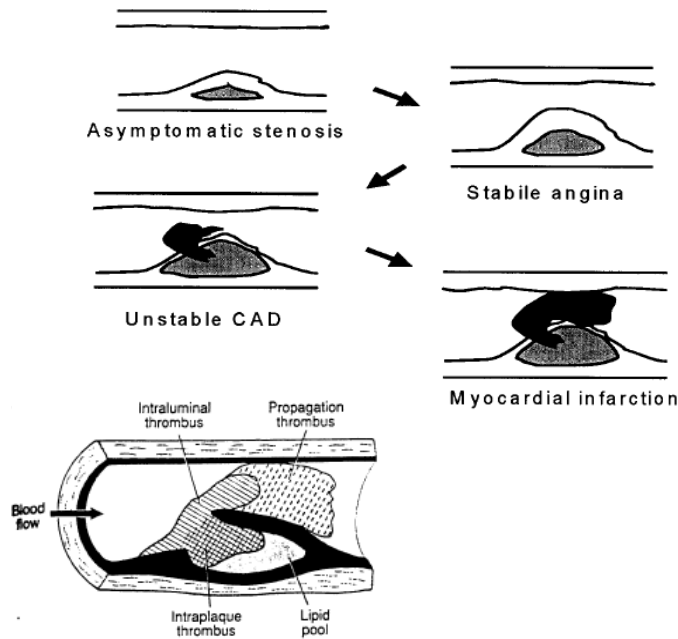


Figure 2.4: Manifestations of arterial disease [16] and representation of an occluding thrombus [20]. CAD denotes Coronary Artery Disease.

2-5- Another Contributing Factor: Vascular Remodeling

Despite extensive studies on plaque disruption described above, stenosis growth within the arterial walls has not been thoroughly examined. Indeed, more recently, clinical observations have shown that atherosclerotic lesions develop slowly and often remain clinically silent for many years [2,3]. As the intima focally thickens, the vessel compensates this at first by dilating, a process called remodeling [1,21], in order to accommodate increasing flow to the organ downstream [21]. This phenomenon can be observed during the natural growth or the left ventricular hypertrophy. When the atherosclerotic plaque or atheroma has reached a size for which the artery can no longer compensate by dilating, it may start to intrude into the vessel lumen and disturb the flow of blood [19]. This ability enables tissues to grow and remodel in

response to disease, injury and even subtle changes in their mechanical environment [22]. In other words, inward remodeling refers to a reduction in vessel size, while outward remodeling refers to an increase in vessel size. Inadequate outward remodeling occurs when it is limited to prevent luminal stenosis.

The radial enlargement of vessels (outward remodeling) has always attracted attention due to its relevance to the growth of plaque. Glagov et al [23], investigated the phenomenon numerically and suggested that by enlarging its size, a vessel compensates for increasing growth of atherosclerotic plaques, thus maintaining good blood flow as well as delaying the development of flow-limiting stenosis. These clinical results were later validated by Hemiler et al. [24] using in vivo intravascular ultrasound (IVUS) experiments. The studies revealed the regular presence of outward remodeling at the site of atheroma. It was demonstrated that outward remodeling could conceal stenoses from angiography studies.

Some vessels do not exhibit only compensatory enlargement or positive remodeling. In some cases they contrarily shrink at the site of stenosis. This phenomenon is called inward remodeling or negative remodeling which has been studied by Pasterkamp et al. [25]. Pasterkamp analyzed the constriction of the vessel lumen and observed that luminal stenosis correlates more directly with the direction and magnitude of remodeling than with plaque size.

Angioplasty, transplant vasculopathy and atherectomy are the treatments typically applied to vascular disease. Experimental studies on diseased arteries of rabbits by Kakuta et al. [30]

contributed to suggest that inward remodeling is the primary cause of restenosis after these treatments in humans.

Ward et al. [21] suggested that adequate outward remodeling may increase the risk of plaque rupture, the underlying cause of acute coronary syndromes and sudden cardiac death as illustrated in Fig. 2.5. Inward remodeling may follow an angioplasty or plaque rupture, resulting in scar contracture.

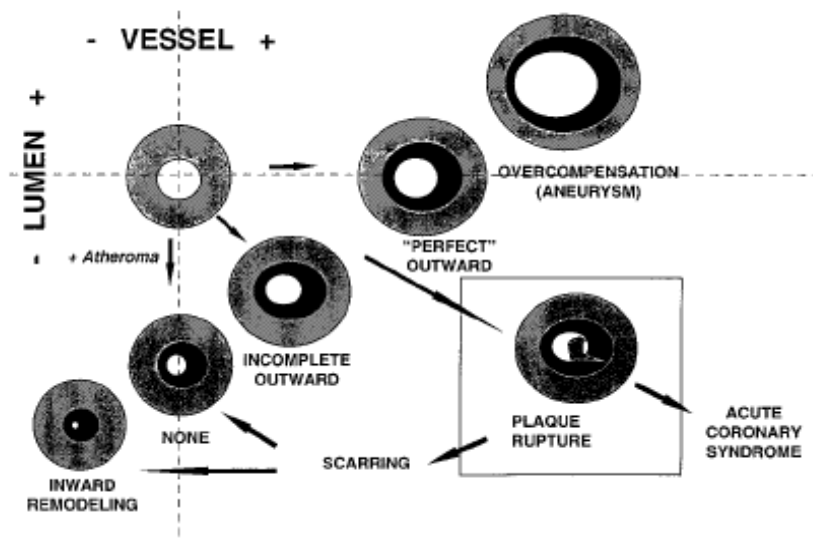


Figure 2.5: Outward and inward remodeling mechanisms; Putative effect on plaque rupture [21]

Plaque morphologies have been characterized in some studies [26-28]. The mechanical behavior of the plaque structure has been experimentally investigated [8, 29]. Beattie et al [8] used non-linear material properties that characterize bio-tissues to experimentally determine the finite strain field in heterogeneous, diseased human aortic cross-sections at physiologic pressures in

vitro. The model included bi-linear material properties for lipid accumulations, fibrous intimal tissue, region of calcification and diseased free zone, which are all essential constituents of atherosclerotic lesions.

2-6- Organization of the Study

The numerous studies listed above present diverse models of the stenotic artery. None of these studies investigate the possible parameters combining fluid and structure behaviors involved in plaque rupture, neither plaque remodeling phenomenon is accounted for. In addition, only few of these studies include the differentiation of the main structural components of the plaques such as fibrous plaque thickness, lipid core size and calcium volume. We will attempt to address these issues by using non-linear material properties for the arterial wall, and non-Newtonian flow on a steady two-dimensional model.

2-7- References

- [1] Ross R., 1999, “Atherosclerosis – an Inflammatory Disease” N. Engl J Med. (340); 2:115-126.
- [2] Erling Falk, Prediman K. Shah, Valentin Fuster, “ Coronary Plaque Disruption”, Circulation. 1995; 92: 657-671
- [3] Suzanne A. Sorof, “Intravascular Atheroma Monitoring: Past , Present and Future of identifying Vulnerable Plaques”, 2004, Applications in Imaging. Cardiac interventions. pp 34-39
- [4] Fuster V, Badimon J, Chesebro JH, et al. “ Plaque rupture, Thrombosis, and Therapeutic Implications”, Haemostasis. 1996; 26(suppl 4): 269-284.
- [5] Lee R.T, 2000, “Plaque stabilization: the role of lipid lowering”. International Journal of Cardiology, 74, S11–S15.
- [6] Loree H M, Kamm Roger D, Stringfellow R G and Lee R T, “ Effects of Fibrous Cap Thickness on Peak Circumferential Stress in Model Atherosclerotic Vessels” , Circulation Research; (1992), Vol. 71, 4; 850-858
- [7] Chen G C , Loree, H M, Kamm R D, Fishbein M C, Lee T R, “ Distribution of Circumferential Stress in Ruptured and Stable Atherosclerotic Lesions: A structural Analysis with Histopathological Correlation”, Circulation. (1993); 87: 1179-1187
- [8] D. Beattie, C. Xu, R. Vito, S. Glagov, M.C. Whang, “Mechanical analysis of heterogeneous, atherosclerotic human aorta”, Journal of biomechanical engineering 120 (1998), 602–607.
- [9] Gourisankaran V., Sharma M.G., 2000, “The finite element analysis of stresses in atherosclerotic arteries during balloon angioplasty”. Critical Reviews in Biomedical Engineering, 28(1&2), 47–51.
- [10] Huang H., Virmani R., Younis H., Burke A.P., Kamm R.D., and Lee R.T., 2001, “The impact of calcification on the biomechanical stability of atherosclerotic plaques”. Circulation, 103, 1051–1056.
- [11] Yamagushi T, Furuta N, Nakayama T, Kobayashi T, “Computations of the Fluid and Wall Mechanical Interactions in Arterial Diseases” 1996 Advances in Bioengineering, ASME BED (1995) ;31: 197-198

- [12] Yamagushi T, Kobayashi T, Liu H, “ Fluid-Wall interactions in the Collapse and Ablation of an Atheromatous Plaque in Coronary Arteries”, Proc. Third World Congress of Biomechanics, (1998) p. 20b
- [13] D. Tang, C. Yang, S. Kobayashi, D. N. Ku, “Effect of a Lipid Pool on A Stress/Strain Distributions in Stenotic Arteries: 3-D Fluid-Structure Interactions (FSI) Models” J. Biomech. Eng.,126, 2004, pp. 363-370
- [14] Tang, D., Yang, C., Kobayashi, S., Ku, N.D., 2002, “ Simulating Cyclic Artery Compression Using a 3D Unsteady Model with Fluid-Structure Interactions”, Computers and Structures, 80, 1651 – 1665
- [15] Tang, D., Yang, C., Kobayashi, S., Zheng, J., Vito R. P., 2003, “ Effect of Stenosis Asymmetry on Blood Flow and Artery Compression: A Three Dimensional Fluid- Structure Interaction Model” Annals of Biomedical Engineering, 31, 1182-1193
- [16] ADINA R&D, Inc., 1999, ADINA System 7.3 Release Notes
- [17] Richardson P. D, Davies M.J, Born D. V. R, “Influence of plaque configuration and stress distribution on fissuring of coronary atherosclerotic plaques”, The lancet, Oct 21, 1989
- [18] Prediman K. Shah, “Plaque disruption and Coronary Thrombosis: New Insight into Pathogenesis and Prevention”, Clin. Cardiol. Vol. 20(suppl. II), II-38-II-44 (1997)
- [19] Lindmark Eva,“ Leukocytes and coronary artery disease” Acta Universitatis Upsaliensis, Uppsala (2002)
- [20] Davies J M, “ A Macro and Micro View of Coronary Vascular Insult in Ischemic Heart Disease”, Circulation (1990); 82 (suppl II): II-38-II-46
- [21] Michael R. Ward, Gerard Pasterkamp, Alan C. Yeung, Cornelius Borst, “Arterial Remodeling: Mechanisms and Clinical implications”, Circulation. 2000; 102:1186-1191
- [22] Humphrey J.D., “continuum biomechanics of soft biological tissues”, The Royal Society review, 2002
- [23] Glasgow S, Weisenberg E, Zarins CK, et al. “Compensatory Enlargement of Human Atherosclerotic Coronary Arteries” , N Engl J Med. 1987; 316:1371-1375
- [24] Hermiler JB, Tenaglia AN, Kisslo KB, et al. “ In Vivo Validation of Compensatory Enlargement of Atherosclerotic Coronary Arteries”, Am J Cardio. 1993;71:665-668

- [25] Pasterkamp G, Wensing PJ, Post Mj, et al. “ Paradoxal Arterial Wall Shrinkage May Contribute to Luminal Narrowing of Human Atherosclerotic Femoral Arteries”, *Circulation*. 1995; 91:1444-1449
- [26] C.L. De Korte et al., Identification of atherosclerotic plaque components with intravascular ultrasound elastography in vivo, *Circulation* 2002, 105 , 1627–1630.
- [27] R. Virmani, F.D. Kolodgie, A.P. Burke, A. Farb and S. M. Schwartz. Lessons from sudden coronary death. *Arteriosclerotic, Thrombosis and Vascular Biology* ,2000, 20, 1262–1275.
- [28] J.A. Rumberger et al. Coronary artery calcium area by electron-beam computed tomography and coronary atherosclerotic plaque area. *Circulation* 1995, 92, 2157–2162.
- [29] Mohan, D. and Melvin. Failure properties of passive human aortic tissue. I. Uniaxial tension tests, *J. Biomech.*, 1982, 15 (11). 887-902
- [30] Kakuta T, Currier JW, Haudenschild CC, et al. “ Difference in Compensatory Vessel enlargement, not Intimal Formation, Account for Restenosis After Angioplasty in the Hypercholesterolemic Rabbit Model”, *Circulation*. 1994, 89:2809-2815

3. MODEL FORMULATION

3-1- Geometry

We consider a diseased artery model illustrated in Fig. 3.1. This model is composed of a channel with an obstruction representing the stenosis. A small lipid core comprising primarily cholesterol is embedded within the stenosis. The volume of the lipid core is less than 15% of the stenosis. In the figure, L and L_s represent the lengths of the artery and stenosis, respectively. The percent stenosis by diameter S_t is defined as follows [1]:

$$S_t = \frac{D_i - D_s}{D_i} \times 100(\%), \quad (3.1)$$

where D_i and D_s are, respectively, the inner diameter of the occluded section and the minimum diameter of the section.

The geometry data used for the study: Total length $L= 110$ mm, length of the stenosis $L_s=10$ mm, inner diameter $D_i = 4$ mm and wall thickness 0.5 mm. The arterial segment proximal to the plaque is chosen to be 50 mm long ($10 D_i$), enabling flow development ahead of the plaque. A similar length of straight segment is provided distal to the plaque to allow some flow recovery before the outlet. The latter also ensures reliable outlet boundary condition in the computation of the fluid flow equations. The eccentricity was assumed to be 100% in all cases to reflect common diseased arteries.

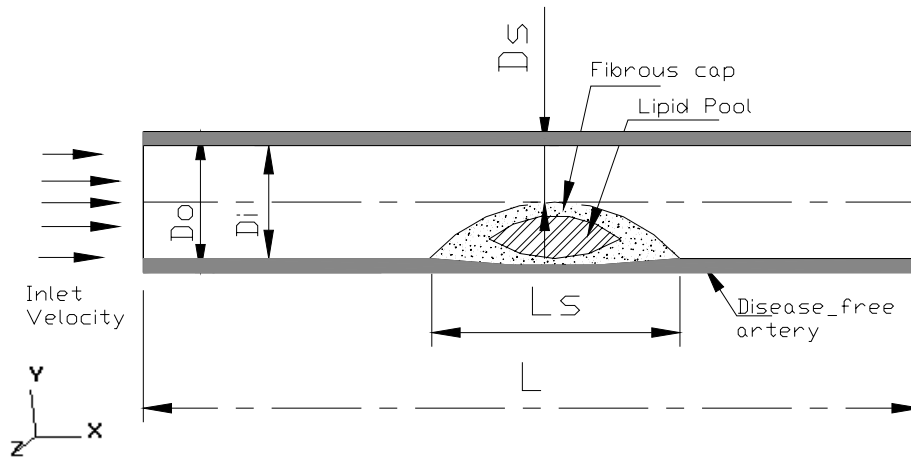


Figure 3.1: Schematic representation of stenosed artery model

3-2- Material Properties

The mathematical model assumes bi-linear isotropic, incompressible material properties. Specifically, we employ the bi-linear models of Beatties et al. [2] for the stenosis constituents, which are defined by the stress-strain curve and the two moduli E_1 and E_2 for the stress values that are less than and greater than the yield stress Y , respectively. This model is chosen because it is an optimization scheme in the sense that it gives good approximation to the non-linear behavior of the material under internal pressure and shear stress. In addition, it is readily implemented in multi-purpose software for simulating fluid structure interactions.

Figure 3.2 presents a typical bilinear strain stress curve. The slopes of the lines L_1 and L_2 give two Young moduli E_1 and E_2 . The approximation of the non-linear stress-strain curve is completely defined by Y , E_1 and E_2 .

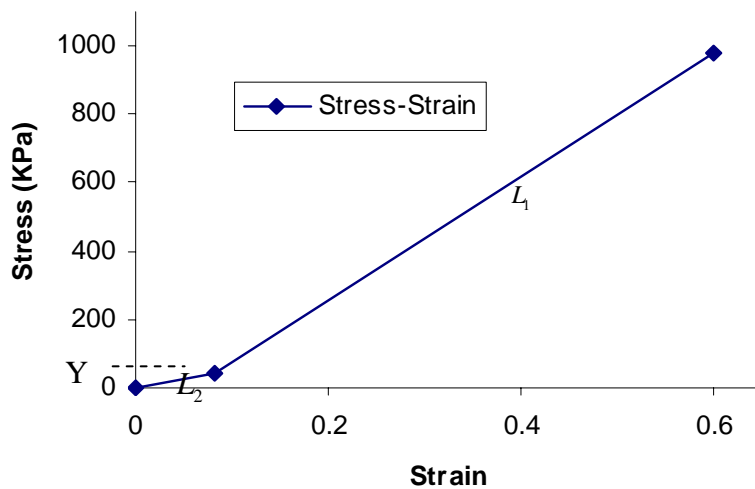


Figure 3.2: Typical bi-linear strain-stress curve

3-3- Structural Analysis

Trilateral and quadrilateral finite elements were generated for the solid and fluid parts of the arterial segment. Unlike previous studies, the internal luminal pressure is not prescribed but rather computed from the flow module and distributed over the inner surface. The input parameters used in the study are summarized in Table 3.1.

Table 3.1 Principal input parameters used for the computation

Materials	Density[3] $\rho - Kg / m^3$	Kinematic Viscosity[3] $\nu - m^2 / s$	Modulus [2] $E_1 - kN / m^2$	Yield Stress [2] Y	Modulus [2] $E_2 - kN / m^2$	Poisson's Ratio [2] ν
Blood-like	1050	$3.6 * 10^{-6}$				
Artery			61.5	8.4	245	0.45
Plaque			483	39.6	1820	0.45
Lipid core			3.81	0.69	38.8	0.45

Previous studies have demonstrated the significant impact of shear stress and structural stresses on plaque rupture [4,5,6,7]. We also predicted the maximum principal stresses (MPS) and Von Mises stresses (VMS). Then, by analogy to the concept of buckling in material failure study [8, 9,19], we normalized the wall shear stresses (SS) obtained from the flow model by each of the above structural stresses for analysis.

Considering a force per unit area $\vec{T}_i = \sigma_{ij} \vec{i}_j$, where σ_{ij} refers to the stress tensor, i (=x, y, z) the face, j (x, y, z) the direction of a cubical domain and \vec{i}_j a unit vector oriented in the j direction.

$\vec{T}_i \cdot \vec{i}_i = \vec{T}_i n_i = \vec{T}_n$ [14,15]. Planes where $\vec{T}_n \cdot \vec{n}$ is maximum give maximum principal stress (MPS)

σ_{\max} or σ_1 . On the other hand, planes where $\vec{T}_n \cdot \vec{n}$ is minimum give minimum principal stress

(mPS) σ_{\min} or σ_2 . The third principal stress is denoted σ_3 [16]. The principal stresses are presented in Fig. 3.3.

$$\sigma_1 = \frac{1}{2}(\sigma_x + \sigma_y) + \sqrt{\left(\frac{\sigma_x - \sigma_y}{2}\right)^2 + \tau_{xy}^2} \quad (3.2)$$

For plane strain, the lateral (reminiscent of circumferential) stress is

$$\sigma_3 = \sigma_z = \nu(\sigma_x + \sigma_y) = \nu(\sigma_1 + \sigma_2) \quad (3.3)$$

where ν is the poisson ratio.

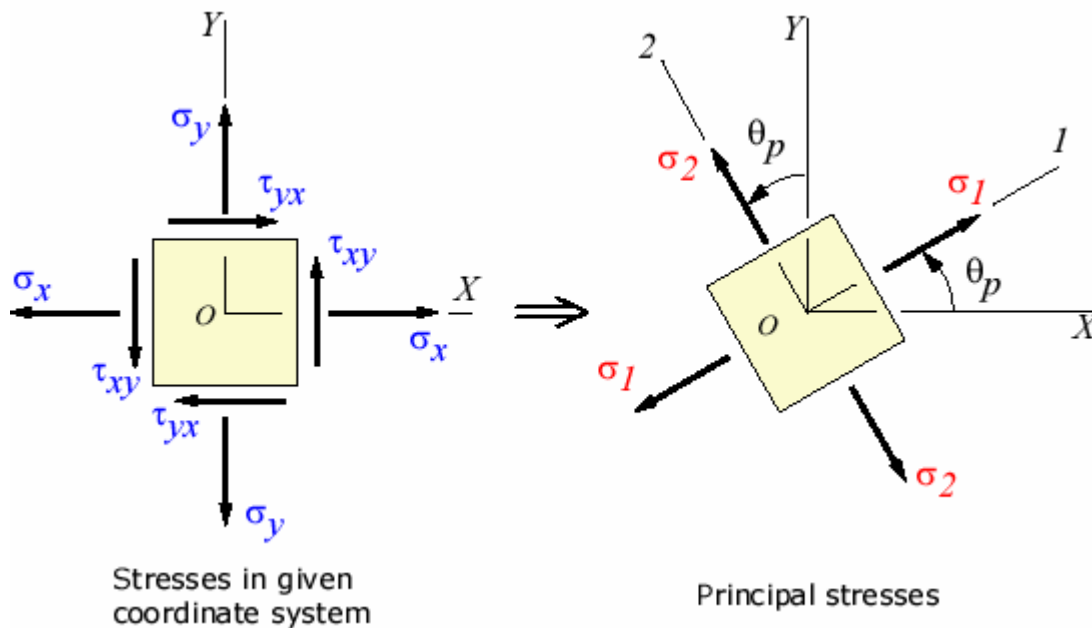


Figure 3.3: Representation of principal stresses and principal directions [17]

$$\tan 2\theta_p = \frac{2\tau_{xy}}{\sigma_x - \sigma_y} \quad (3.4)$$

The angle θ_p defines the principal directions where the only stresses are normal stresses.

The maximum shear stress (MSS or τ_{\max}) at a point is the absolute maximum shear stress that acts on any plane passing through the point, (the largest in magnitude of the three values of structural shearing stress). τ_{\max} is expressed as: [16]

$$\tau_{\max} = \left| \max \left(\frac{\sigma_1 - \sigma_2}{2}, \frac{\sigma_2 - \sigma_3}{2}, \frac{\sigma_3 - \sigma_1}{2} \right) \right| \quad (3.5)$$

The Von Mises stress (VMS) or the effective stress is the stress related to the distortional energy (total energy minus energy due to hydrostatic pressure) of the body, Von Mises stress σ_{vm} is given by the relation

$$\sigma_{vm} = \left[\frac{1}{2} \{ (\sigma_1 - \sigma_3)^2 + (\sigma_2 - \sigma_3)^2 + (\sigma_1 - \sigma_2)^2 \} \right]^{\frac{1}{2}} \quad (3.6)$$

There is a correlation between MPS and lateral (circumferential) stress on one hand (Eq. 3.3), and between maximum shearing stress and Von Mises stress, presented in the figure 3.4, on the other hand. These similarities will be used later when establishing an index of plaque rupture.

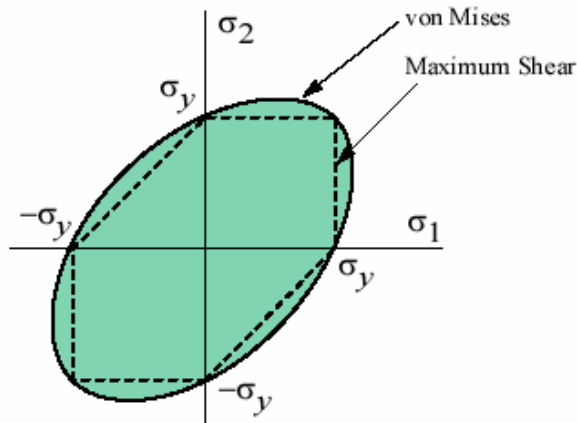


Figure 3.4: Von Mises stress and Maximum shearing stress [18]

Buckling is a sudden deflection associated with unstable equilibrium and resulting in total collapse of the member. Elastic buckling associated with elastic deflection limiting the maximum load that can be applied to the member without causing the member to fall [19].

Consider a straight slender column axially loaded and material perfectly homogeneous, as presented in Fig. 3.5. The column will remain straight under value of the load. It will not bend. At a critical load, however, a small lateral force is applied; giving the column any small deflection and the lateral force is then removed. The critical axial load is the load that will hold the slender column in the slightly bent position. When the buckling takes place the elastic deflection and stresses in the member are not proportional [19].

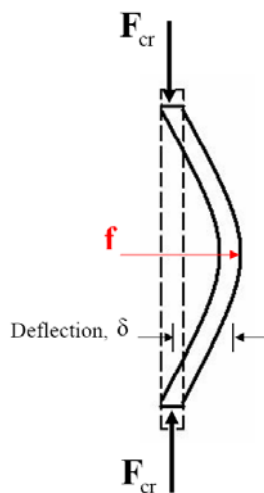


Figure 3.5: Buckling of ideal slender column

The buckling also occurs on thin-walled cylinder subjected to radial pressure [19] as shown in Fig. 3.6. It results in appearance of lobes which are the areas of tensile stress and compressive stress. Considering that patterns of maximum tensile and compressive stress have been found in

stenotic section [20], that finding suggests that there is an analogy between the buckling of a thin-walled cylinder subjected to radial pressure and plaque rupture as we attempt to show in Fig. 3.7., where the shear stress acts as a small force that deflects the fibrous cap in the flow direction, stretching plaque upstream and rendering that area more vulnerable to buckling.

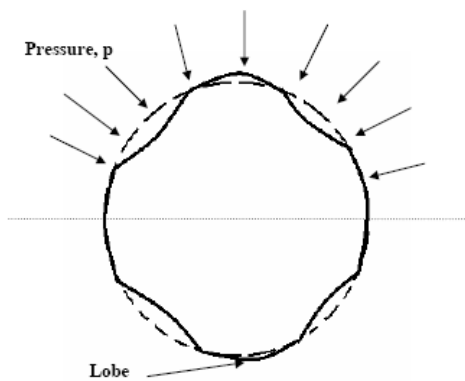


Figure 3.6: Buckling configuration of thin-walled cylinder subjected to radial pressure

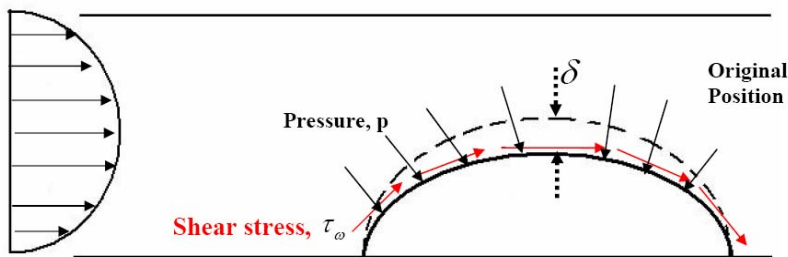


Figure 3.7: Pressure acting on stenotic plaque

The following equilibrium and boundary conditions have been used for the artery wall models [7,10]:

$$\sigma_{ij,j}^{(Sd)} = 0 \quad (3.7)$$

$$\sigma_{ij}^{(Sd)} \cdot n_j \Big|_{inner\ surf} = \sigma_{ij}^{(fd)} \cdot n_j \Big|_{inner\ surf} , \quad (3.8)$$

$$d_{inner\ surf}^{(Sd)} = d_{inner\ surf}^{(fd)} , \quad (3.9)$$

$$d_{-Y}^{(Sd)} \Big|_{outer\ surf} = 0 , \quad (3.10)$$

$$d_{-X}^{(Sd)} \Big|_{inlet,\ outlet\ surf} = 0 , \quad (3.11)$$

where, for a specific value of i or j ($=1,2,3$) the symbol $()_{,i}$ denotes the partial differential operator $(\partial/\partial x_i)$. The parameters $d^{(Sd)}$ ($d_{-X}^{(Sd)}$, $d_{-Y}^{(Sd)}$), $d^{(fd)}$ are the displacements (X and Y directions, respectively) and $\sigma_{ij}^{(Sd)}$, $\sigma_{ij}^{(fd)}$ are the stress tensors for solid and fluid, respectively.

3-4- Flow Analysis

This study considers steady, viscous, incompressible flow in the asymmetric diseased artery models illustrated in Fig. 3.1. A lipid pool is considered due to the clinical observations that its characteristics may be closely linked to plaque rupture and may increase the magnitude of stress distribution over the fibrous cap [12, 4]. The Navier-Stokes equations for 2D flow with compliant walls were solved using the CFD-ACE-GUI flow solver [13].

The governing equations solved in this study for the steady flow behavior can be expressed as:

Flow direction:

$$\nabla \cdot (\vec{V}u) = \frac{1}{\rho} \left[-\frac{\partial p}{\partial x} + \nabla \cdot (\mu \nabla u) \right], \quad (3.12)$$

Transverse direction:

$$\nabla \cdot (\vec{V}v) = \frac{1}{\rho} \left[-\frac{\partial p}{\partial y} + \nabla \cdot (\mu \nabla v) \right], \quad (3.13)$$

where, p is the static pressure.

For boundary conditions, we assume no-slip on the walls, impervious wall and the inlet and outlet of the segment have no axial displacement. The inlet velocity and outlet pressure are prescribed as indicated in Table 3.1, and represented mathematically as:

$$\mathbf{u} \Big|_{\Pi} = (0, 0), \quad (3.14)$$

$$\frac{\partial \mathbf{u}}{\partial x} \Big|_{inlet, outlet} = (0, 0), \quad (3.15)$$

$$u \Big|_{x=0} = u_{in} = 0.2 \text{ m/s}, \quad (3.16)$$

$$p \Big|_{x=l} = p_{out} = 0.0 \text{ Nm}^{-2}, \quad (3.17)$$

where, \mathbf{u} is the inflow velocity vector, p_{out} the pressure at the outlet, and Π is the interface between fluid and structure domains.

The viscous stresses are related to the deformation rates for the assumed Newtonian flow, thus:

$$\tau_{xx} = 2\mu \frac{\partial u}{\partial x} - \frac{2}{3}\mu(\nabla \cdot \vec{V}), \quad (3.18)$$

$$\tau_{yy} = 2\mu \frac{\partial v}{\partial y} - \frac{2}{3}\mu(\nabla \cdot \vec{V}), \quad (3.19)$$

And $\tau_{xy} = \tau_{yx} = \mu \left(\frac{\partial u}{\partial y} + \frac{\partial v}{\partial x} \right).$ (3.20)

where, $\boldsymbol{\tau}$ is the viscous stress tensor.

3-5- Fluid Structure Interaction

The CFD code employed for this study (CFD-ACE-GUI, [13]) uses a two-way implicit coupling between the fluid and structure modules. The pressures and velocities obtained from the flow modules are sent to the stress module at every 10th iteration where deformations and stresses are calculated. Then, these deformations are sent back to the flow module, where the solution is recalculated on the new deformed geometry. Iterations are performed until convergence is obtained. The governing finite element equations for both the solid and fluid were solved by the conjugate gradient squared supplied with preconditioning (CGS+Pre) with 50 sweeps for the velocity equations and 500 sweeps for the pressure correction equation. Convergence was achieved if

$$\|g^{i+1} - g^i\| / \left\{ \max(\|g^{i+1}\|, \varepsilon) \right\} \leq Conv, \quad (3.21)$$

where g is the variable being solved such as pressure, velocity, wall displacement, i , iteration index, ε is the small number to be selected in case $\|g\|$ is near zero, and $Conv$, is convergence

value chosen in this study to be 0.0001. Another convergence based on mass flow rate is also monitored. Specifically, the computational iteration continues until the calculated difference between the mass inflow and mass outflow rates is negligible (less than 0.001%). Typically, the ratio of this difference to the prescribed mass inflow rate is less than 0.1 % [10].

Trilateral and quadrilateral finite elements are generated for the solid and fluid parts of the arterial segment, resulting in 7,800 to 9,300 elements for the models used in establishing the fluid structure index γ of plaque rupture, 10,400 to 11,600 elements for the extended downstream models used in blood pressure investigation and over 23,000 elements for the extended upstream and downstream models used in plaque composition investigation. The basis for application of these models are detailed in the subsequent sections

3-6- References

- [1] American Heart Association, American Stroke Association, “Heart Disease and Stroke Statistics” 2005 update
- [2] Davies J M, “ A Macro and Micro View of Coronary Vascular Insult in Ischemic Heart Disease”, *Circulation* (1990); 82 (suppl II): II-38-II-46
- [3] Ross R., 1999, “Atherosclerosis – an Inflammatory Disease” *N. Engl J Med.* (340); 2:115-126.
- [4] Erling Falk, Prediman K. Shah, Valentin Fuster, “ Coronary Plaque Disruption”, *Circulation.* 1995; 92: 657-671
- [5] Suzanne A. Sorof, “Intravascular Atheroma Monitoring: Past , Present and Future of identifying Vulnerable Plaques”, 2004, *Applications in Imaging. Cardiac interventions.* pp 34-39
- [6] Richardson P. D, Davies M.J, Born D. V. R, “Influence of plaque configuration and stress distribution on fissuring of coronary atherosclerotic plaques”, *The lancet*, Oct 21, 1989
- [7] Prediman K. Shah, “Plaque disruption and Coronary Thrombosis: New Insight into Pathogenesis and Prevention”, *Clin. Cardiol.* Vol. 20(suppl. II), II-38-II-44 (1997)
- [8] Loree H M, Kamm Roger D, Stringfellow R G and Lee R T, “ Effects of Fibrous Cap Thickness on Peak Circumferential Stress in Model Atherosclerotic Vessels” , *Circulation Research*; (1992), Vol. 71, 4; 850-858
- [9] Chen G C , Loree, H M, Kamm R D, Fishbein M C, Lee T R, “ Distribution of Circumferential Stress in Ruptured and Stable Atherosclerotic Lesions: A structural Analysis with Histopathological Correlation”, *Circulation.* (1993); 87: 1179-1187
- [10] D. Beattie, C. Xu, R. Vito, S. Glagov, M.C. Whang, “Mechanical analysis of heterogeneous, atherosclerotic human aorta”, *Journal of biomechanical engineering* 120 (1998), 602–607.
- [11] Gourisankaran V., Sharma M.G., 2000, “The finite element analysis of stresses in atherosclerotic arteries during balloon angioplasty”. *Critical Reviews in Biomedical Engineering*, 28(1&2), 47–51.

- [12] Huang H., Virmani R., Younis H., Burke A.P., Kamm R.D., and Lee R.T., 2001, "The impact of calcification on the biomechanical stability of atherosclerotic plaques". *Circulation*, 103, 1051–1056.
- [13] Yamagushi T, Furuta N, Nakayama T, Kobayashi T, "Computations of the Fluid and Wall Mechanical Interactions in Arterial Diseases" 1996 *Advances in Bioengineering, ASME BED* (1995) ;31: 197-198
- [14] CFD-ACE, 2004, "V2004 Module Manual V1", ESI US R&D. Inc., Huntsville, AL.
- [15] Nicholson, W. David, 2003, "Finite Element Analysis, Thermomechanics of Solids", CRC Press, Florida.
- [16] Vable, Madhukar, 2002, "Mechanics of Materials", Oxford University Press, New York.
- [17] Efunfa, Engineering fundamental.
http://www.efunda.com/formulae/solid_mechanics/mat_mechanics/calc_principal_stress.cfm
- [18] Wikipedia, http://en.wikipedia.org/wiki/Von_Mises_stress
- [19] Fred B. Seely, James O. Smith, "Advanced Mechanics of Materials" John Wiley & Sons, Inc., second Edition 1965, pp.585-625
- [20] Tang, D., Yang, C., Kobayashi, S., Ku, N.D., 2001, "Steady Flow and Wall Compression in Stenotic Arteries: A Three-Dimensional Thick-Wall Model with Fluid-Wall Interactions," *Journal of Biomechanical Engineering*, 123, pp. 548–552

4. ESTABLISHING THE FLUID-STRUCTURE INTERACTION (FSI) INDEX OF PLAQUE RUPTURE

4-1- Overview

In this study, we address the clinical observation that most myocardial infarction (MI) patients have moderate stenoses (less than 50%) by using two-dimensional stenosis models geometrically similar to a coronary artery. We consider non-linear material properties of the arterial wall, a small lipid pool and varying stenosis severities. We investigate the flow, structure and fluid-structure interaction effects by predicting the profiles of velocity, pressure, and fluid and structural stresses, and the impacts of these parameters on plaque stability. The computational results are analyzed to propose new plaque stability criteria.

4-2- Formulation

In this study, 5 models of stenosis levels of 20%, 30%, 40%, 50% and 70% were considered, representing native (20% stenosis), moderate (30%, 40% and 50% stenosis) and severe (70% stenosis) cases. The eccentricity was assumed to be 100% in all cases to reflect common diseased arteries.

4-3- Results

This study has three objectives: First, model the flow characteristics; second, investigate the effects of the mechanical properties of the arterial wall on the stenosis models; and third, identify

a suitable fluid-structure interaction (FSI) index to characterize plaque rupture. These three objectives will be considered separately in the following presentation of the computed results.

4-3-1 Fluid-Flow

The predicted flow patterns in the lumen are presented in Fig. 4.1 for two representative stenosis levels: (a) 40% and (b) 70%. The plot for the 70% stenosis (Figure 4.1-b) is presented on a different scale to amplify the peculiarity of the flow patterns. The oval-shaped section on the bottom wall represents the stenosis. Within the stenosis is a smaller oval structure representing the lipid pool. The two lines connecting the lipid pool to the bottom of the stenosis are reference lines demarcating the area surrounding the lipid pool into two parts. This procedure is dictated by the software meshing protocol that cannot mesh any surface entirely surrounded by another.

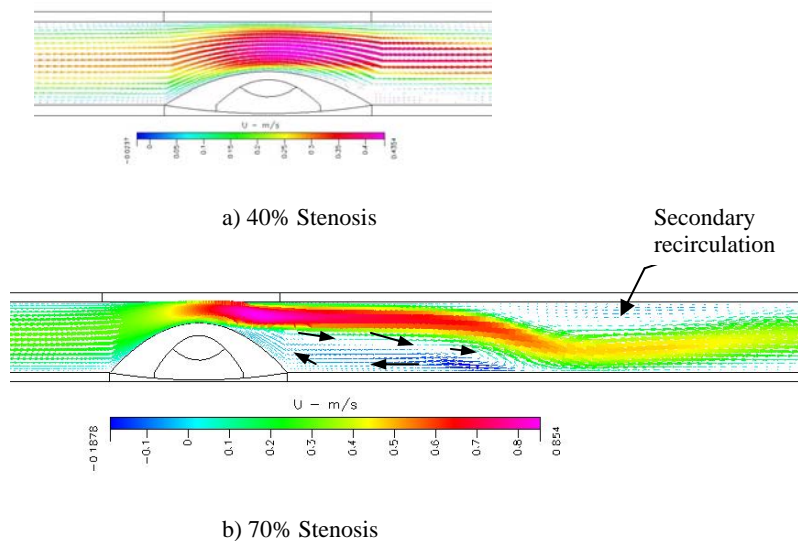


Figure 4.1: Flow velocity profile and flow re-circulations (small arrows)

The predicted velocity profile is parabolic upstream of the stenosis for all the cases. These results indicate that the flow has become fully developed over the 12D length upstream of the stenosis as expected. Then, the velocity increases within the constricted section above the stenosis with the maximum value ranging from 0.34 m/s for 20% stenosis to 0.85m/s for 70% stenosis. The parabolic profile is progressively distorted as the plaque severity increases. A small recirculation vortex develops in the lee of the stenosis, the size and the strength of which increase with the stenosis severity. For the most severe stenosis (70%) a second re-circulation vortex develops on the upper surface (Fig. 4.1-b). The recirculation vortices are characterized by negative velocity.

A flow recirculation occurs just distal to the stenosis due to the decrease in pressure in the expanding flow channel and the no-slip condition on the surface. A second recirculation vortex occurs for the 70% stenosis case due to the combination of flow momentum and the inertia force created by the first recirculation vortex. In other words, the pull by the first vortex creates a vacuum effect on the opposite upper side of the channel, which is rapidly filled with backward flow to balance the momentum. The provided recirculation is important because it impacts the deposition of atherogenesis constituents such as LDL (low-density lipoproteins) in the lumen. The deposition is mediated by both the low shear stress (SS) and the increased residence time of the constituents in the recirculation zone [1,2]. The resident time increases with the size of the recirculation vortex.

The corresponding predicted pressure distribution (not shown) indicates pressure increase upstream of the plaque as the stenosis level increases. The pressure decreases rapidly as the velocity gradient increases on the upstream segment. The opposite effects occur downstream of the plaque where the pressure increases as the velocity gradient decreases. Also, in the case with 70% stenosis, the pressure remains negative on the downstream part until it recovers towards the outlet of the vessel. The minimum pressure is not located on the tip of the stenosis but slightly on the downstream side.

The corresponding distribution of shear stress (SS) for 20%, 40% and 70% stenosis as a function of X is presented in Fig. 4.2. The parameter X on the horizontal coordinate represents the longitudinal distance along the solid-liquid interface. The vertical thick lines represent the location of the symmetric vertical plane (SP) through the stenosis.

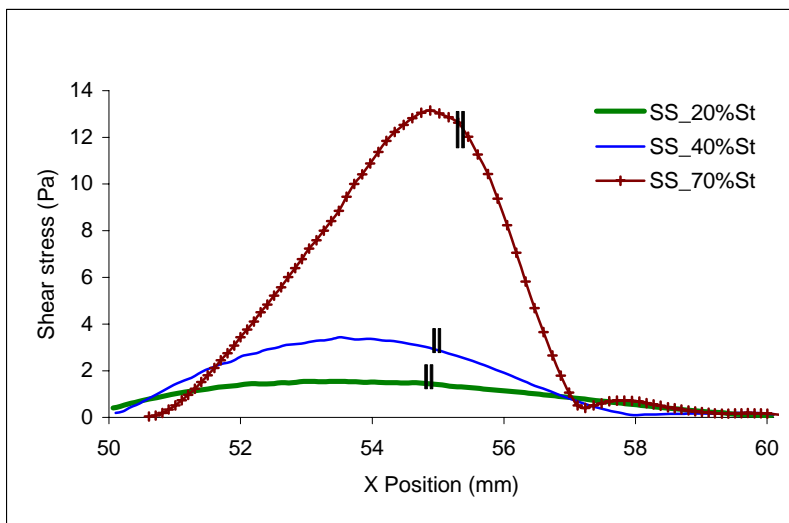


Figure 4.2: Endothelial shear stress (SS) distribution along the solid-liquid interface for different stenosis levels

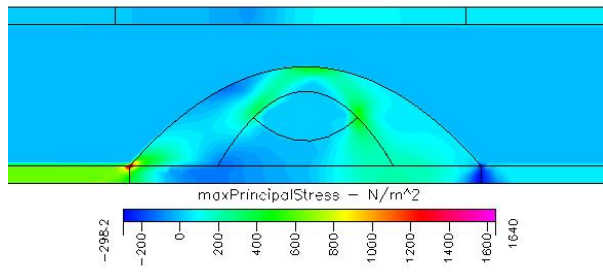
Figure 4.2 shows that the shear stress increases with the stenosis level at the upstream side of the plaque and its maximum occurs just before the symmetric vertical plane. The wall shear stress rises monotonically to a maximum in the upstream section, and then drops to the lowest value before oscillating to a constant value. The location where the stress drops from the maximum is quite distinct for the stenosis levels above 40%.

The shear stress increases at the upstream side of the lesion is due to the flow acceleration resulting from channel reduction. The predicted sharp drop in the shear stress distribution and the minimum value after the drop have been observed previous studies [3,4]. The minimum stress following the drop is located at the re-attachment point downstream of the symmetric vertical plane.

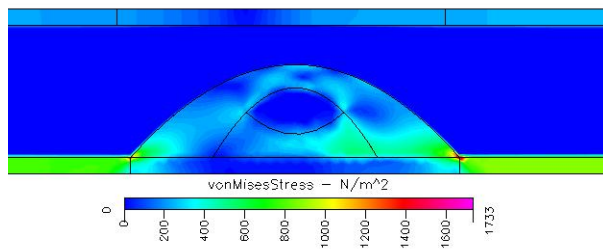
4-3-2 Structural Analysis

The predicted representative stress contour plots from structural analysis are illustrated in Figure 4.3. The plots presented in the figure are the contours of maximum principal stress (MPS) (a) and Von Mises stress (VMS) (b) for the 70% stenosis model. These parameters describe the total stresses that a material endures for a given applied pressure. Figure 4.3-a shows that plaque undergoes compressive and tensile stress predominantly in the upstream section. Under the same hemodynamic conditions, Fig. 4.3-b shows coexistence of low and high Von Mises stress (VMS) bands in the stenosis. The lowest VMS contours are located in the lipid pool as expected and

areas scattered adjacent to the lipid core. The figure illustrates the effect of lipid pool on biomechanical stress distribution in the stenotic plaque.



(a)



(b)

Figure 4.3: (a) Maximum Principal Stress (MPS) and (b) Von Mises Stress (VMS) band plots

Figure 4.4 shows the maximum principal stress (MPS) and Von Mises stress (VMS) for 20% (a) and 70% (b) stenosis levels. The horizontal axis X represents the distance along the solid-liquid interface. The interface considered in these plots are located just within the fibrous cap to fully account for the structural effects, and stretches from the proximal to the distal ends of the stenosis ($X=50.1\text{mm}$ to 60.1mm). The vertical axis represents the predicted structural stress obtained in N/m^2 . The vertical thick line represents the location of the symmetric vertical plane (SP) passing through the stenosis.

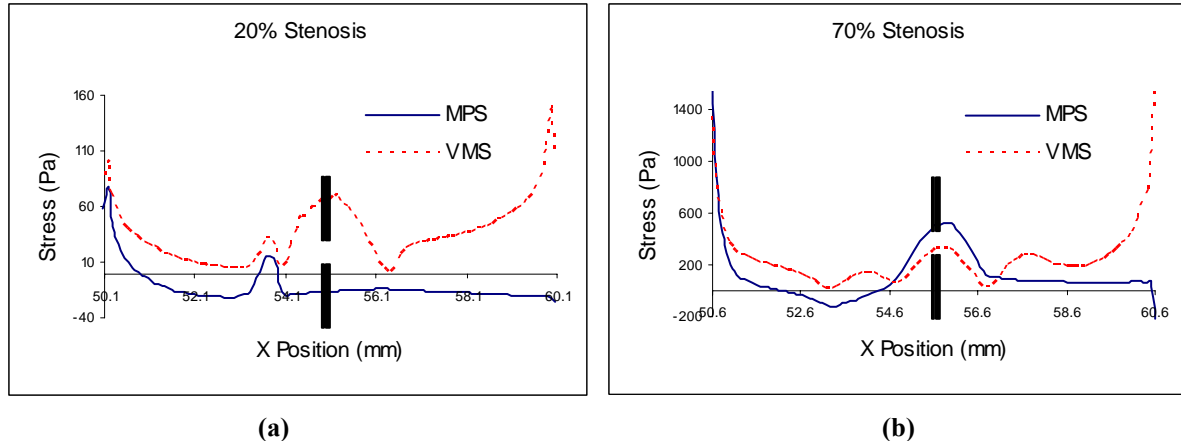


Figure 4.4: Maximum Principal Stress (MPS) and Von Mises Stress (VMS) distributions

These results indicate that within the fibrous cap the MPS starts with high positive values at the proximal end of the stenosis and subsequently drops rapidly to negative values. The initial high values are due to stress continuity between the upstream disease-free arterial wall and the diseased segment. The incoming flow compresses the plaque proximally while the upstream wall segment is under tension. This compression produces the observed negative MPS. Peaks of MPS extension are also evident in the model. The main MPS peak for 70% stenoses (stenosis higher than 30% not shown in this paper) is located on the SP, and upstream of the SP for 20% stenosis. This trend is due to the lipid pool reaction to the external compression. The MPS increases with stenosis severity on the SP due to the low pressure above the plaque. Specifically, the lesion sustains important compression on its upstream side and deforms on its top where there is less resistance in order to balance the surrounding forces. The drop in the MPS curve at the end of the vessel is associated with the compression of the disease-free artery wall distal of the stenosis.

The Von Mises stress (VMS) curves show three consecutive peaks: one on each side of the SP and one on the SP. The peaks on both sides of the SP increase with the stenosis severity while the peak on the SP is relatively high for 20% stenosis ($70 N/m^2$), decreases to ($25 N/m^2$) for 40% stenosis, and significantly rises (up to $\sim 350 N/m^2$) for 70% stenosis.

The Maximum shear stress (MSS) and lateral (reminiscent of circumferential) stress (SZZ) for different stenosis levels 20%, 40% and 70% are shown in Figure 4.5. The maximum shearing stress (MSS) is meant to describe the stress on the planes 45% away from the MPS plane, where the structural shear stress is maximal. The lateral or circumferential stress describes the stress in the direction perpendicular (out-of-plane) to the model. The horizontal axis represents the ratio X/D as explained earlier. The vertical axis represents the structural stress obtained in N/m^2 .

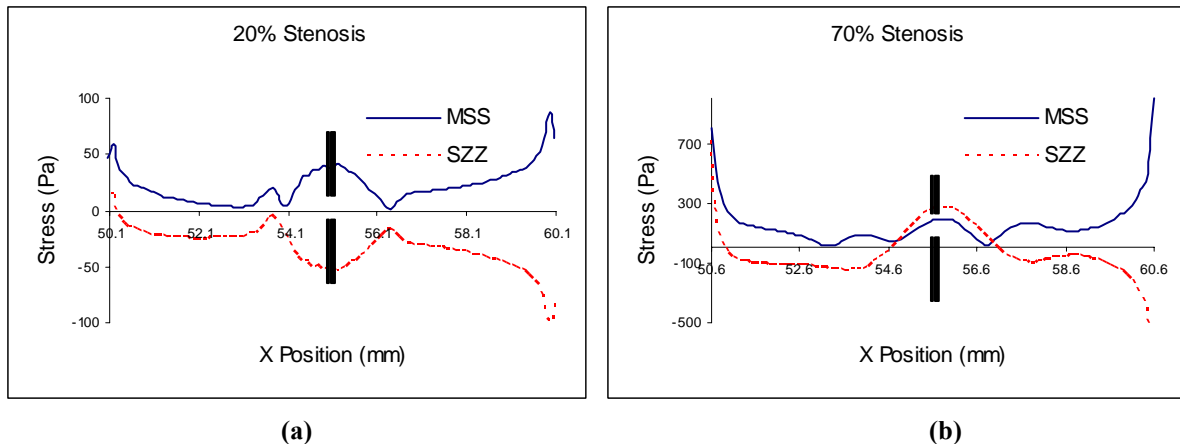


Figure 4.5: Maximum principal stress (MSS) and lateral (circumferential) stress (SZZ) distributions

These results indicate that as for MPS, the SZZ starts with high positive values and decrease to negative values. Like the MPS, the positive SZZ values are due to stress continuity between the upstream disease-free arterial wall and the diseased segment. Negative SZZ values are compressive stresses due to the internal pressure obliquely distributed over the diseased segment unlike the case on the disease-free segments where they are radial. On both sides upstream and downstream of the diseased segment, SZZ acts in opposite directions. A peak of SZZ extension identified with positive value is also observed in the graph at the SP for stenosis greater than 30 % levels. It is important to note that similar to the MPS curve, SZZ rises with stenosis severity on the symmetric vertical plane.

Similar to what have been previously shown in the Von Mises stress (VMS) results, the maximum shear stress (MSS) curve exhibits three consecutive peaks; one on each side of the SP and one on the SP. The peaks on both sides of the SP increase with the stenosis severity, while the peak on the SP is relatively high for mild stenosis (20% stenosis), decreases for moderate stenosis (30%-50% stenosis) and significantly rises for severe stenosis (70% stenosis).

The results presented in Fig.4.5 are quite similar to those in Fig. 4.4, and the similarities will be used as an alternative means to support our assumptions, and to validate the implication of our results; These issues are addressed in the following section.

4-3-3 Fluid Structure Interaction (FSI)

4-3-3-1. Stress Normalization

In this section we attempt to establish appropriate FSI index γ to characterize plaque potential to rupture. The parameters identified for investigation are the stress ratios R_1 and R_2 . R_1 is the endothelial shear stress normalized by the maximum principal stress (SS/MPS), and R_2 is the shear stress normalized by the Von Mises Stress (SS/VMS). Figure 4.6 shows the distributions of the stress ratios R_1 and R_2 .

Our choice of normalizing the endothelial fluid shear stress by the structural stresses stems from the following three reasons. First, several studies have shown that shear stress and structural stress play important roles in plaque disruption [1,3,4,12]. Second, the successive compression and extension of structural stress distribution in the plaque as observed in the previous section (4-3-2). Third, analogy to the mechanism of buckling in material failure studies [5,6,13] with internal pressure in our vessel model related to compressive pressure in the buckled material, and shear stress in our vessel related to perturbation (transverse force) in the material.

The ratio distributions presented in Figure 4.6 are for 20% (Figure 4.6-a) and 70% (Figure 4.6-b) stenosis levels. The distance X is measured along the solid-liquid interface and D is the nominal diameter of the normal artery segment proximal to the lesion.

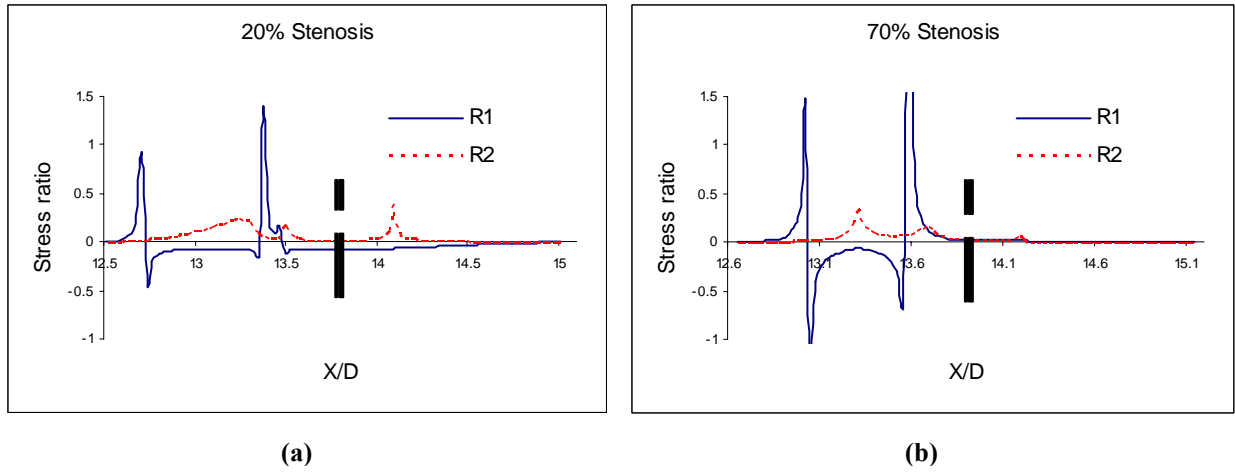


Figure 4.6: Stress ratio R_1 and R_2 distributions

The results indicate that the stress ratio R_1 has multiple positive and negative peaks. These peaks are located where R_1 is infinite (discontinuous). This trend is expected since the maximum principal stress (MPS) is zero at these locations. R_1 is negative between the two infinities prior to the mid-plane SP due to the compressive MPS. Between the peak prior to and on the SP, R_1 is low and positive for moderate (40%) and severe (70%) stenoses but remains negative for mild stenosis (20%). After the SP, only R_1 for 40% stenosis displays a discontinuity again and changes sign at approximately 1/3 the distance from the base of the lesion, downstream of the SP.

The stress ratio R_2 curves have two peaks upstream of the SP and one downstream. The first peak is more interesting to investigate for three reasons. First, it occurs on the shoulder where

plaques are most likely to rupture [7,8], second its base is larger than the others, and third, it varies with the stenosis severity. A closer look at both ratios, show that at the location of the first peak of R_2 , the ratio R_1 changes with the stenosis level. The implication of this trend will be described in more detail later in this section.

The stress ratios R_3 and R_4 distributions are presented in Fig. 4.7. R_3 is the ratio of wall shear stress to maximum shear stress (SS/MSS), and R_4 is the ratio of wall shear stress to lateral (circumferential) stress (SS/SZZ). Similar to the cases above, the ratio distributions presented below are for stenosis levels: 20% and 70%, corresponding to Fig. 4.7-a and 4.7-b, respectively. The details of the data and for the ratios have been presented in the previous sections (4-3-1 & 4-3-2)

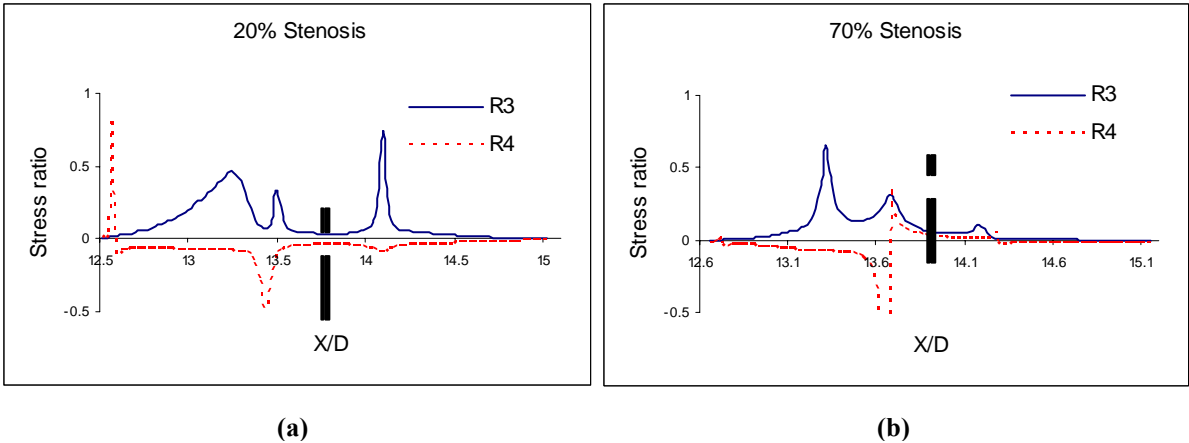


Figure 4.7: Stress ratio distributions R_3 and R_4

The results in the figure indicate that similar to R_1 , the R_4 distribution exhibits multiple positive and negative peaks. These peaks are located where R_4 is infinite (discontinuous). This trend is clearly expected since lateral (circumferential) stress (SZZ) is zero at these locations. Between the two R_4 infinities prior to the mid-plane SP, R_4 is negative due to the compressive SZZ. At the vicinity of the SP, R_4 remains almost unchanged and close to zero. After the SP, R_4 for moderate (40 %) and severe (70%) stenosis levels becomes discontinuous again and changes sign at approximately 1/3 the distance from the base of the lesion, downstream of the SP.

The stress ratio R_3 curves have similarities to R_2 and the characteristics cited previously for R_2 can be applied to R_3 . In addition, at the location of the first peak of the ratio R_3 , the stress ratio R_4 changes with the stenosis level. This result as well will be described in more detail later in the following section.

4-3-3-2. Summary: FSI Indices

The fluid structure interaction parameters that we computed to characterize stenotic plaque rupture are summarized in Fig. 4.8. The horizontal axis represents the stenosis range, and the vertical axis represents the monitored stress ratio. Specifically, the plots represent the values of R_1 and R_4 at monitored locations (R_{1_mon} and R_{4_mon} respectively) for stenosis levels of 20%, 30%, 40%, 50% and 70% stenosis. The monitored locations are the X/D locations where the first

R_2 and R_3 maximum values occur upstream of the mid plane (SP) in Figs. 4.6 and 4.7 respectively. These locations are selected because they are situated on the plaque shoulder where plaque rupture most likely occurs, and the magnitude of the stress ratio varies with stenosis severity, thus,

$$R_{1_mon} = \left| R_1 \left\{ \left(\frac{X}{D} \right)_{R_2_{Max}} \right\} \right|, \quad (4.1)$$

$$R_{4_mon} = \left| R_4 \left\{ \left(\frac{X}{D} \right)_{R_3_{Max}} \right\} \right|. \quad (4.2)$$

The monitored R_1 and R_4 values are presented in Fig. 4.8 below for comparison.

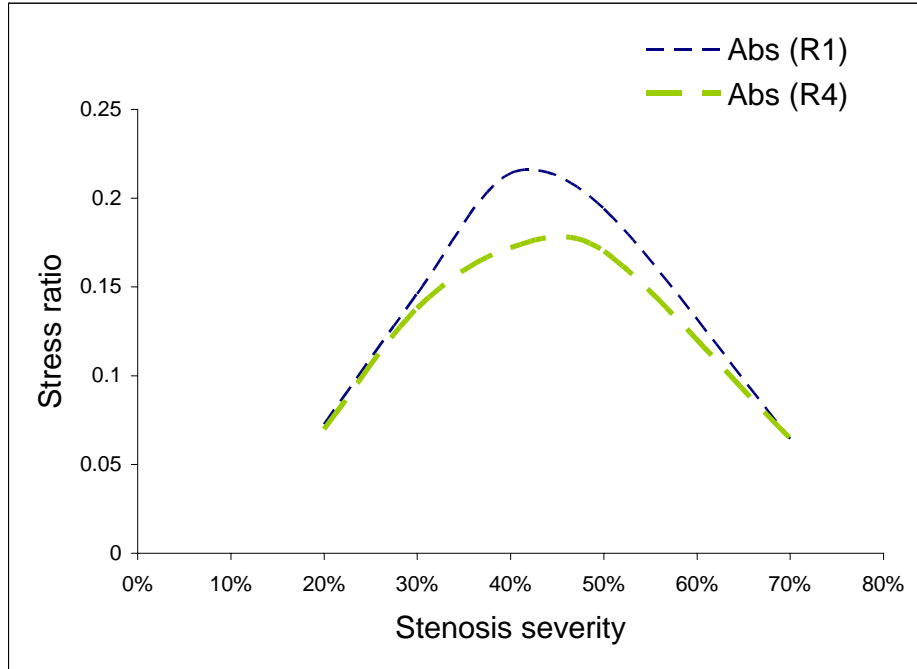


Figure 4.8: FSI indices R_{1_mon} (or γ) and R_{4_mon} as a function of stenosis rate

The results show that the two indices predicted to characterize plaque rupture R_{1_mon} (or γ) and R_{4_mon} exhibit the same trend, but R_{1_mon} is consistently larger than R_{4_mon} . In general, the predicted FSI indices are small for both mild (e.g. 20%) and severe (e.g. 70%) stenosis. Interestingly these indices reach a maximum between the extreme stenosis levels at approximately 40%-45% stenosis rate. This stenosis range could be considered at risk to rupture and is consistent with medical observation suggesting that nearly 68% of myocardial infarction patients had less than 50% stenosis [9,10,11]. In other words, the results indicate that the FSI indices investigated here could serve to characterize plaque rupture. It is worth noting that plaques typically remain asymptomatic until the stenosis level exceeds about 70% of the lumen

[9,11]. The results presented here suggest that lipid-laden plaques of about 40-45% stenosis may be at risk to sudden rupture of the fibrous cap.

By carefully monitoring the stress ratio R_1 or R_4 at the location of maximum stress ratio R_2 or R_3 respectively, an experimental study can be devised to establish the stability value of R_{1_cr} or R_{4_cr} (critical value) for atheroma rupture. These critical stress ratios combine the interaction of flow and structural parameters on plaque characteristics, and are referred here to as the flow-structure interaction (FSI) stability indices.

The FSI indices need to be associated with the plaque location where the stress ratios become infinite in order for the indices to be meaningful. Specifically, If there is no discontinuity in either R_1 or R_4 distribution, the plaque is likely stable. By the same token, if there is discontinuity in R_1 or R_4 and their magnitude at the location of maximum R_2 or R_3 respectively is smaller than a threshold value (to be determined experimentally), then the plaque is likely stable. Otherwise the plaque is deemed unstable.

4-4- Closing Remarks

Our results show that structural stresses (MPS, MSS, VMS, and SZZ) increase with the stenosis levels. In order to establish a critical index of plaque rupture, we use the analogy of the investigated system to buckling of thin-walled cylinder subjected to radial pressure [13]. Specifically, we normalized the endothelial shear stress (SS) obtained from the flow model by

the above structural stresses for analysis. We predicted the parameters R_1 and R_2 (or alternatively R_3 and R_4), expressing the ratio of endothelial fluid shear stress to Maximum Principal stress and Von Mises stress (or the ratio of endothelial fluid shear stress to maximum structural shear stress and lateral stress) in the plaque, respectively. We found that monitoring the R_1 values (or alternatively, R_4 values) at the vicinity of its discontinuity, specifically on the plaque shoulder at the location where the ratio R_2 (or R_3) distribution is maximum, predicts that stenosis levels in the range 40%-45% are most at risk to rupture. This observation is consistent with the clinically observed critical stage of lipid-laden plaques [9,10,11].

These findings are quite encouraging since, in spite of the simplifying assumptions made, they are consistent with the fact that plaques often rupture at moderate severity [10,11]. Further validation of this critical index would require further studies that relax some of the assumptions made, coupled with systematic experimentation and validation.

4-5- References

- [1] Hu, Z., 2000, "In ViVo Characterization of Human Coronary Artery Flow," Ph.D. thesis, Northeastern University, Boston, MA.
- [2] Lindmark E., 2002, "Leukocytes and Coronary Artery Disease : Experimental and Clinical Studies" Technical Report From the Faculty of Medicine 1110, Acta Universitatis Upsaliensis, Uppsala.
- [3] Nosovitsky, V., Ilegbusi, O., Jiang J., Stone, P., Feldman, L., 1997, "Effects of the Curvature and Stenosis-Like Narrowing on Wall Shear Stress in Coronary Artery Model with Phasic Flow," Computers and Biomedical Research, **30**, pp. 61-82.
- [4] Tang, D., Yang, C., Kobayashi, S., Ku, D., 2004, "Effect of a Lipid Pool on A Stress/Strain Distributions in Stenotic Arteries: 3-D Fluid-Structure Interactions (FSI) Models," J. Biomech. Eng.,**126**, pp. 363-370
- [5] Nicholson, D., 2003, Finite Element Analysis, Thermomechanics of Solids, CRC Press, Florida. pp. 185-194, Chap. 14.
- [6] Vable, Madhukar, 2002, Mechanics of Materials, Oxford University Press, New York, Chap. 10.
- [7] Huang, H., Virmani, R., Younis, H., Burke, A., Kamm, R., Lee, *et al.*, 2001, "The Impact of Calcification on the Biomechanical Stability of Atherosclerotic Plaques," Circulation, **103**, pp. 1051–1056.
- [8] Shah, P., 1997, "Plaque Disruption and Coronary Thrombosis: New Insight into Pathogenesis and Prevention", Clin. Cardiol., **20**(suppl. II), pp. II-38-II-44
- [9] Sorof, S., 2004, "Intravascular Atheroma Monitoring: Past, Present and Future of identifying Vulnerable Plaques," Applications in Imaging - Cardiac interventions, pp. 34-39
- [10] Falk, E., Shah, P., Fuster, V., 1995, "Coronary Plaque Disruption," Circulation, **92**, pp. 657-671
- [11] Fuster V, Badimon J, Chesebro JH, et al. " Plaque rupture, Thrombosis, and Therapeutic Implications", Haemostasis. 1996; 26(suppl 4): 269-284.

- [12] Yamagushi T, Kobayashi T, Liu H, “ Fluid-Wall interactions in the Collapse and Ablation of an Atheromatous Plaque in Coronary Arteries”, Proc. Third World Congress of Biomechanics, (1998) p. 20b
- [13] Fred B. Seely, James O. Smith,“Advanced Mechanics of Materials” John Wiley & Sons, Inc., second Edition 1965, pp.585-625

5. EFFECT OF BLOOD PRESSURE ON FSI INDEX OF PLAQUE RUPTURE

5-1- Overview

High blood pressure (HBP) is one of the risk factors of heart attack and stroke. Indeed, over 65,000,000 people have been estimated to this condition in the United States. Although HBP is routinely diagnosed on visits to the physicians, its direct influence on cardiovascular diseases has not been systematically quantified. The numerous studies listed in the literature review (Section 2) present diverse models of the stenotic artery but none directly quantify the direct effect of blood pressure. More studies are therefore needed to fully account for the incidences of varying high blood pressure on atherosclerotic plaque rupture. We will introduce in this section, a new approach to understanding of these issues by using non-linear material properties for the arterial wall, and non-Newtonian flow on two-dimensional models of stenosed to a coronary arteries. A small lipid pool and varying stenosis severities are considered. In order to simulate the effect of blood pressure on plaque stability, we imposed a range of pressure levels at the inlet relative to the outlet of the arterial segment in the fig. 3.1. In effect, we imposed varying pressure drop per unit length in the segment. The pressure drop considered ranged from 500 Pa to 1500 Pa over the 160 mm arterial segment length corresponding to Inlet pressure of 1000 Pa to 2000 Pa. These values translate to 7.5 mm Hg to 15 mm of Hg and are on the order of 10% of the physiological diastolic blood pressure. It should be noted that normal blood pressure ranges up to 120/80 mm Hg (systole/Diastole), prehypertension is from 120/80 to 139/90 mm Hg and hypertension is over 140/90 mm Hg. It should be remembered that these values are consistent with those expected in

coronary arteries according to the American Heart Association[1].We investigate the flow, structure and Fluid-Structure Interaction effects by predicting the velocity, pressure, and fluid and structural stress patterns, and the effect of high pressure on these parameters. The computational results are analyzed using FSI index of plaque rupture we established in the section 4. The following section describes in detail the methodology employed.

5-2- Formulation

The geometrical model presented in Fig 3.1 was extended distally to 100 mm to account for the flow disturbance due to high internal pressure. The extension allows flow to recover after passing through the diseased area location of high shear stress and vortices.

A set of 35 (5x7) arterial segments representing stenosed coronary arteries are considered, each with a total length of 160 mm. These models are divided into five groups with stenosis levels of 20%, 30%, 40%, 50% and 70%, ranging from native (20%) to severe (70%) cases. The eccentricity is assumed to be 100% in all cases to reflect common diseased arteries. For each group, seven (7) different pressure drops (P_d) are investigated: 500 Pa, 700 Pa, 750 Pa, 850 Pa, 950 Pa, 1250 Pa and 1500 Pa. These pressure drops over the 160 mm model length in effect represent the imposed inlet pressure over the reference outlet pressure. The corresponding pressure drops per unit length are 3125 Pa/m, 4375 Pa/m, 4687 Pa/m, 5312 Pa/m, 5937 Pa/m, 7812 Pa/m and 9375 Pa/m respectively.

Although the blood flow velocity can be zero, its pressure can never be zero [2]. Therefore, we assume that all models have a reference 500 Pa at the outlet. The normal blood pressure in the aorta is typically less than 120 /80 mm of Hg (or 16,000/10,700 Pa) for systolic and diastolic pressures respectively [1]. The diameter of coronary arteries, the largest at the end diastolic pressure, is typically 10% of the aorta. Thus, we have chosen inlet pressure that give average

pressures within the arterial segment relative to the aorta diastolic pressure on the order of their diameter ratio. Specifically, the set of inlet pressures is 9.4 – 18 % and 6.2 – 12 % of the normal diastolic and systolic pressures respectively in the aorta. The inlet pressures used are summarized on Table 5.1.

Table 5.1 Blood pressure values used at inlet of arterial segment

	Case 1	case 2	case 3	case 4	case 5	case 6	case 7
Inlet pressure							
(Pa)	1000	1200	1250	1350	1450	1750	5000
Pressure drop							
(Pa)							
per 160 mm model length	500	700	750	850	950	1250	1500

The inlet and outlet pressures are prescribed as indicated in Table 5.1 and represented mathematically as:

$$p|_{x=0} = p_{inlet} = \text{varies } 1000 \sim 2000 \text{ Nm}^{-2}, \quad (5.1)$$

$$p|_{x=l} = p_{out} = 500 \text{ Nm}^{-2}, \quad (5.2)$$

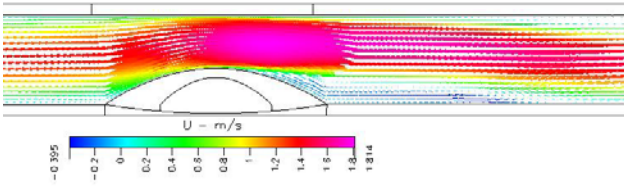
where p is the pressure.

5-3- Results

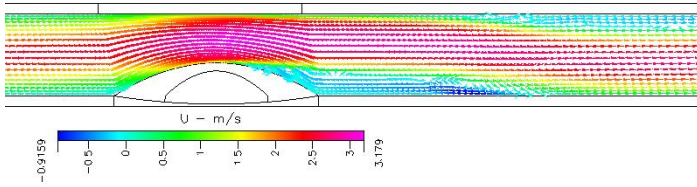
This study has 2 major components. The first is to investigate the impact of pressure on arterial segments with critical stenosis level. The second is to investigate the effect of pressure on the fluid-structure interaction (FSI) index γ of rupture established in section 4. These two objectives will be addressed in the following presentation of the computed results.

5-3-1 Fluid-Flow Analysis

Representative flow pattern predicted for 40% and 70% stenosis are shown in Figs. 5.1 & 5.2. for $\Delta P_L = 3125$ Pa/m and $\Delta P_L = 5937$ Pa/m. The 40% stenotic models (Fig. 5.1), have been chosen to represent the vulnerable plaque as observed in previous studies [3,4] and established in section 4. The 70% stenotic model (Fig. 5.2) represents the severe situation.



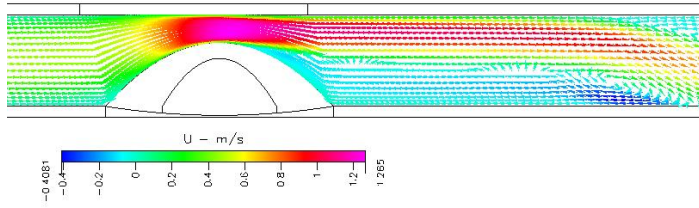
(a) 40% Stenosis, $\Delta P_L = 3125 \text{ Pa/m}$



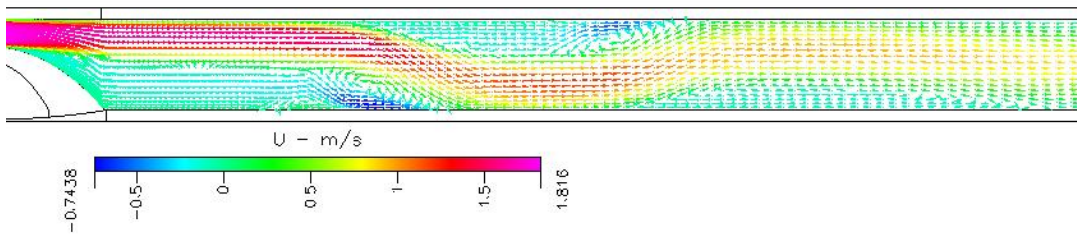
(b) 40% Stenosis, $\Delta P_L = 5937 \text{ Pa/m}$

Figure 5.1: Flow velocity and flow re-circulations for 40% stenosis

The figures show that a flow re-circulation occurs distal to each stenosis and the Reynolds number increases with increasing pressure. Also, the length of first recirculation zone increases with the increase of the pressure drop (fig. 5.1), as well as the increase of the stenosis severity (figs. 5.1 & 5.2). In addition, secondary recirculations appear downstream of the first (Fig. 5.2). These findings correlate with previous studies on stenotic arterial models [5,6]. In particular, plaques with stenosis in the range $30 < St < 60\%$ have been observed to exhibit one secondary recirculation zone while those above 60% have two secondary recirculation zones [5]. The number of these mini (2^{nd}) zones also increases with the Reynolds number (bore with increase in the imposed favorable pressure).



(a) 70% Stenosis, $\Delta P_L = 3125$ Pa/m



(b) 70% Stenosis, $\Delta P_L = 3125$ Pa/m

Figure 5.2: Flow velocity and flow re-circulations for 70% stenosis

The recirculation is important because it impacts the deposition of atherogenesis constituents such as low-density lipoproteins (LDL) in the lumen. The deposition is mediated by both the low shear stress (SS) and the increased residence time of the constituents in the recirculation zone [7,8]. The resident time increases with the size of the recirculation vortex.

The predicted endothelium shear stress distribution for 40% stenosis is presented in Fig. 5.3. for two representatives ΔP_L (3125 Pa/m to 5937 Pa/m). The parameter X/D on the horizontal coordinate represents the dimensionless distance along the arterial wall (solid)-blood (liquid) interface. The vertical dash line represents the symmetric plane (SP) passing through the stenosis

throat. In this section, we monitor the location of maximum shear stress which ranges from about $X/D = 13.6$ to 13.9 depending on ΔP_L . That monitored location is upstream of the SP on the plaque shoulder.

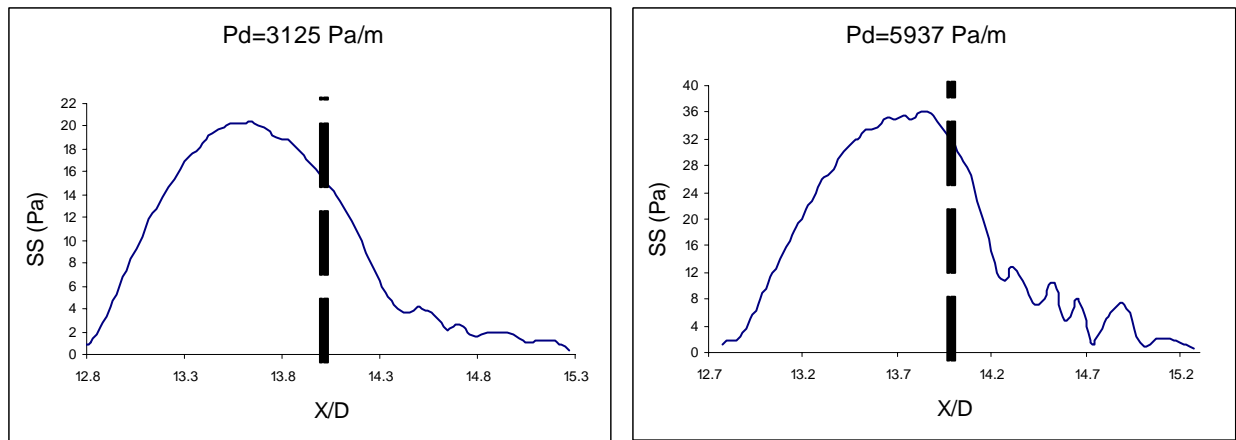


Figure 5.3: Endothelial Shear stress distribution along the solid-liquid for 40 % Stenosis

The predicted maximum shear stress occurs upstream of the segment throat (SP). It varies from 20.4 N/m^2 to 41.8 N/m^2 over the pressure gradients considered. The increase in maximum shear stress averages about 15% per 625 Pa/m increase in ΔP_L . The shear stress distribution downstream of the SP oscillates due to the mini-recirculation vortices that develop within the recirculation zone at high arterial pressure.

5-3-2 Structural Analysis

The structural stress distributions in the vessel are presented in Figs. 5.4 & 5.5 for selected pressure gradients ($\Delta P_L = 3125 \text{ Pa/m}$ and 5937 Pa/m). Figure 5.4 shows the maximum principal stress (MPS) and, Fig. 5.5 shows the Von Mises stress (VMS). The lipid pool is located symmetrically within the plaque and represented by the small oval within the stenosis.

Figure 5.4 shows that the tensile and compressive MPS values increase with pressure. MPS is highly compressive at the stenosis shoulders and tensile at the throat, around the symmetrically placed lipid pool. The transitions from compressive to extensive stresses are abrupt, which may weaken the fragile stenosis envelope and ultimately provoke rupture of the fibrous cap.

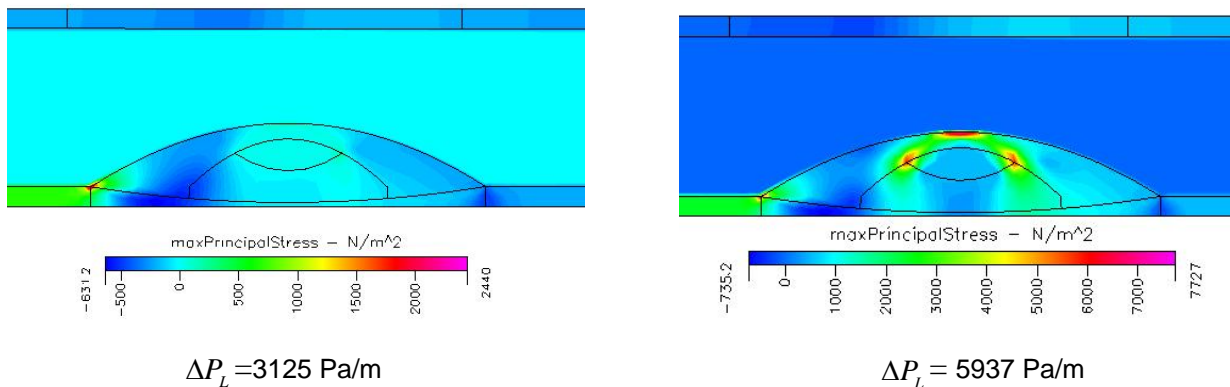


Figure 5.4: Maximum principal stress (MPS) distribution within the plaque for 40% St., and for $\Delta P_L = 3125 \text{ Pa/m}$ and $\Delta P_L = 5937 \text{ Pa/m}$

Figure 5.5 shows that the Von Mises stress (VMS) also increases with the increase in pressure. However, in contrast to the MPS, the VMS is higher at the proximal end and base of the stenosis and steadily decreases towards the surface. The VMS is lower on the stenosis shoulders than the throat. In addition, the VMS concentrate around the lipid pool as observed in previous publication [9,10,11]. This result indicates that cholesterol accumulation may have an impact on atherosclerotic plaque rupture.

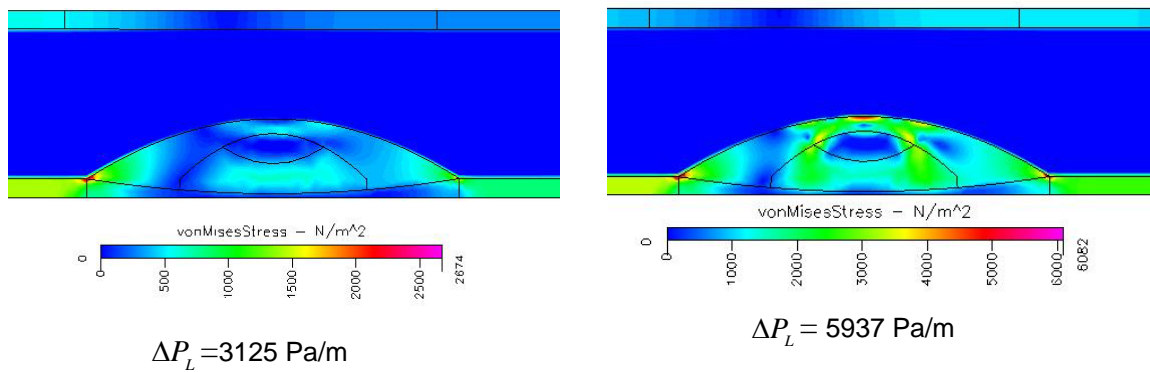


Figure 5.5: Von Mises stress (MPS) distribution within the plaque for 40% St., and for $\Delta P_L = 3125 \text{ Pa/m}$ and $\Delta P_L = 5937 \text{ Pa/m}$.

Figure 5.6 shows plots of the MPS and VMS for 40% stenosis along the solid-liquid interface for which our previous studies indicate high potential for plaque rupture [12]. Although we considered pressure drops in the range $\Delta P_L = 3125 \text{ Pa/m}$ to 9375 Pa/m , only four representative cases (from $\Delta P_L = 3125 \text{ Pa/m}$ to $\Delta P_L = 5937 \text{ Pa/m}$) have been shown in Fig. 5.6 for brevity.

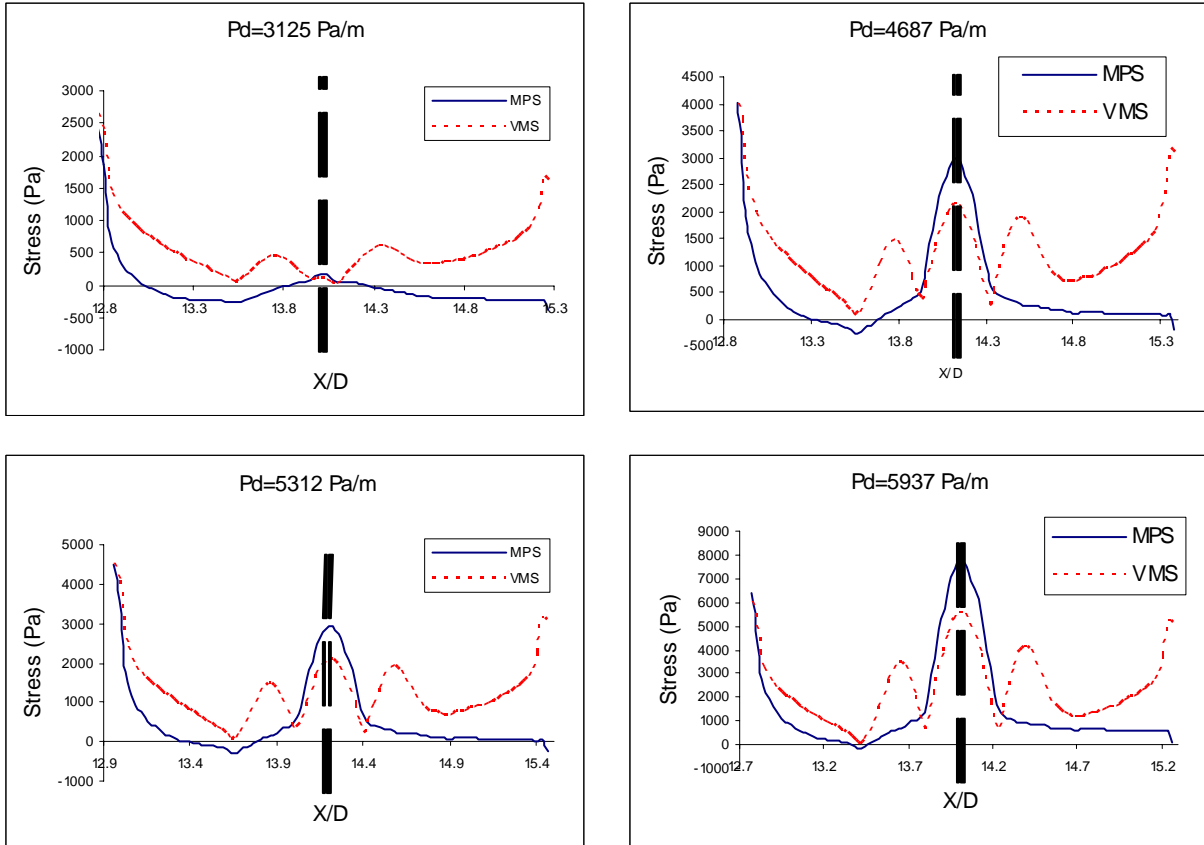


Figure 5.6: Maximum principal stress (MPS) and Von Mises stress (VMS) for 40% stenosis.

The MPS distribution follows the same pattern as in the previous sections (4-3-2), namely, compressive and extensive MPS which rise with increase in pressure. The stenotic arterial segment undergoes extension at the symmetric plane (SP) increases with pressure. The rate of increase of MPS is lowest for ΔP_L in the range of 4687 Pa/m to 5312 Pa/m. Although not presented here, we found that the mild (20%) and severe (70%) Stenotic models exhibit compressive stress at this location. The compression is maintained for the mild stenosis model even for pressure drops above 5952 Pa/m. In contrast, compression is observed on the severe

stenosis model for pressure drops of less than 3333 Pa/m. For mild stenosis, a peak stress extension is observed on the plaque shoulders on each side of the symmetric plane SP. These peaks are maintained throughout the range of pressure drops considered

In general, the Von Mises stress (VMS) curves on Figure 5.6 have three consecutive peaks, one on each side of the SP and one on the SP. These peaks increase with the increase pressure. The rate of increase of VMS is higher on the SP than on either side of the SP.

5-3-3 Fluid Structure Interaction (FSI)

The predicted stress ratios R_1 and R_2 for a range of pressure drop along the segment are presented in Figure 5.7. R_1 is the ratio of shear stress to maximum principal stress (SS/MPS), and R_2 is the ratio of shear stress to Von Mises Stress (SS/VMS). Two representative pressure drops cases $\Delta P_L = 3125$ Pa/m and $\Delta P_L = 5937$ Pa/m are presented in the figure.

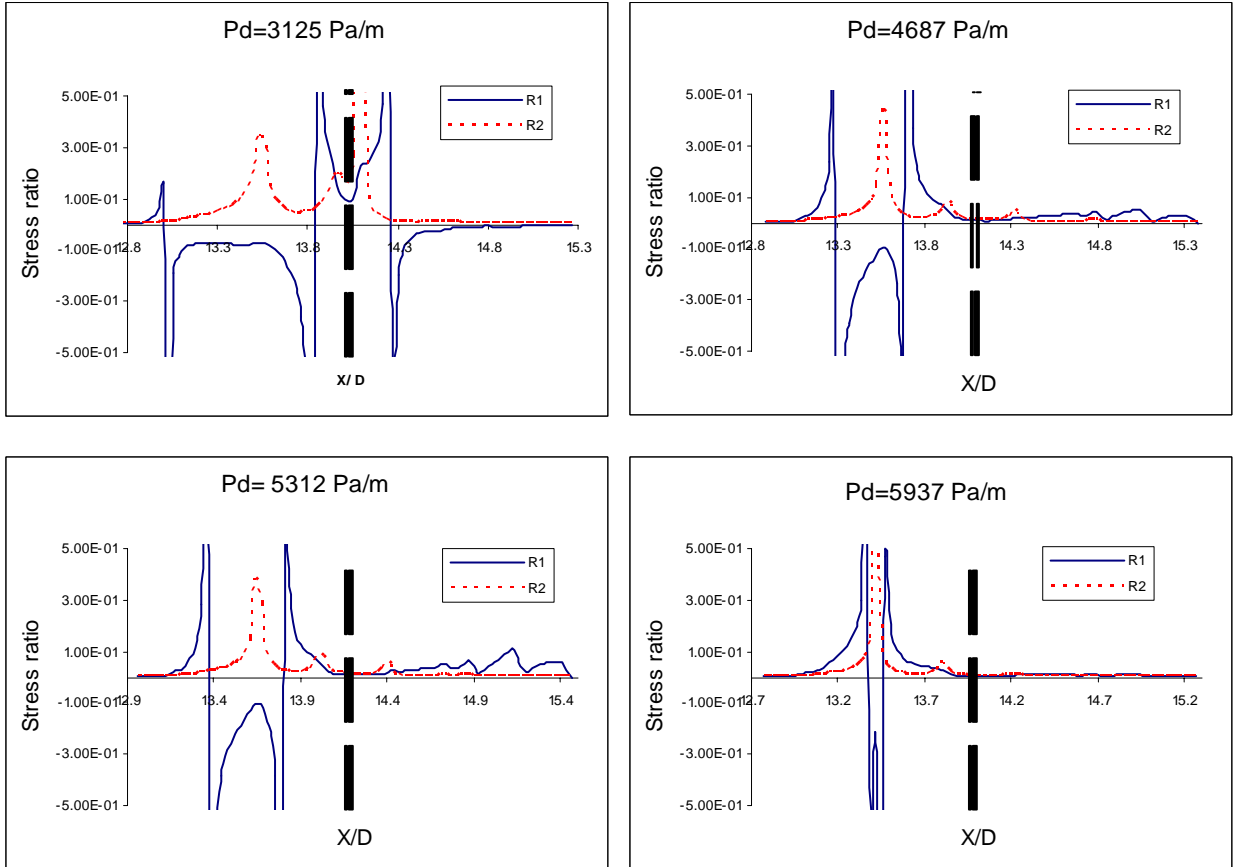


Figure 5.7: Stress ratios R_1 and R_2 along the segment for 40 % Stenosis.

The R_1 distributions are similar for all the pressure drops considered. Each plot exhibits multiple positive and negative peaks which occur as R_1 value approaches infinity. The negative and positive values of R_1 are due to the compressive and extensive MPS, respectively. Two important characteristics are observed on the left side of the symmetry plane, SP. First, between the two consecutive R_1 infinities, the magnitude of R_1 appears to progressively increase relative to the

horizontal reference axis as the pressure increases. Second, the two consecutive R_1 infinities seem to close up, reducing the region that is subjected to compressive stress. This reduction may contribute to the weakening of the plaque. Although not shown in Fig. 5.7, we also observed that the rate of closure of the R_1 infinities is less pronounced on the mild and severe stenotic models than the 40% stenosis presented here.

The R_2 plots exhibit two positive peaks on the left side of the SP and one on the right. Unlike the R_1 plots, the predicted values of R_2 at the first peak oscillates between 0.34 and 0.67 over the pressure drop range 3125 Pa/m to 5937 Pa/m.

5-3-4 Effect of Pressure Drop on FSI Index

The computed Fluid structure interaction parameters are plotted as function of the stenosis rate and pressure drop ($\Delta P_L = 3125$ Pa/m to 7812 Pa/m) in Fig. 5.8. The horizontal coordinate represents the stenosis rate and the vertical axis represents the stress ratio R_1 monitored at the X/D location of the first maximum of R_2 at the proximal side of the symmetry plane, SP. This value can be expressed as:

$$R_{1_mon} = \gamma = R_1 \left[\left(\frac{X}{D} \right)_{R_2_Max} \right]. \quad (5.3)$$

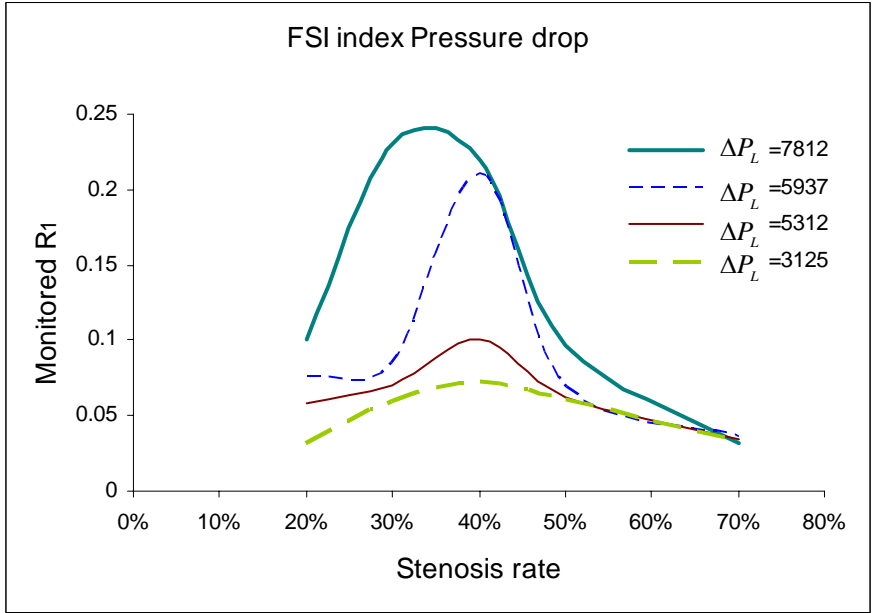


Figure 5.8: The FSI index as a function of stenosis rate and pressure

The predicted FSI index is low for both mild (20%) and severe (70%) stenoses and increases monotonically between them to reach a maximum at about 30%-40% stenosis. This result is consistent with the findings of Falk et al [3] that nearly 68% of patients with myocardial infarction had less than 50% stenosis. There is a dramatic increase in the FSI value at 40% stenosis for pressure drop above 5312 Pa/m. This increase may be attributed to the non-uniform deformation of the stenotic model as the lipid pool is subjected to high arterial pressure (as indicated by the biomechanical stress variations in Figs. 5.5, 5.6 & 5.7).

It should be noted that the plaques that are most likely to rupture (i.e. with high R1) remains at about 40% stenosis level for pressure drops below 5937 Pa/m. For higher pressure drops suggestive of hypertensive state, the range of propensity to rupture progressively shifts towards low stenosis levels. In other words, high pressure appears to render otherwise stable plaques vulnerable to rupture. This finding is consistent with clinical observations that high blood pressure contributes to plaque disruption [1,10,14,15]. It is however important to note that although the 20% plaque may rupture due to high arterial pressure, it does not contain enough cholesterol to provoke arterial clog.

5-4- Closing Remarks

Stenosis stress distribution is critical in the process of understanding the mechanism of plaque rupture. The ultimate purpose of this research is to provide the physician a useful tool to accurately assess critical conditions of arterial disease. Changes in the geometrical and structural parameters are pivotal for plaque stability. Our results suggest endothelial shear stresses and biomechanical stresses are affected by changes in the arterial pressure. While the endothelial shear stress generally increases with pressure, the variation in the structural stresses depends on the specific location within the plaque area.

The stress ratios R_1 and R_2 are affected by the arterial pressure. Specifically, the two successive infinities of R_1 upstream of the throat plane SP seems to close up with increase in pressure drop. This result implies a reduction in the section of the plaque that is subjected to compressive stress at high pressure, which may weaken the plaque.

Investigation of the effect of pressure on plaque rupture shows that 40% stenosis remains the most susceptible to rupture. However, other plaques which otherwise were less critical at normal blood pressure ($< 40\%$) enter the threshold of vulnerability to rupture at high pressures. These results suggest that high arterial pressure may indeed accelerate early atherosclerotic plaque disruption, consistent with clinical observations that high blood pressure contributes to acute cardiovascular events [1,14].

5-5- References

- [1] American Heart Association, American Stroke Association, “Heart Disease and Stroke Statistics” 2005 update
- [2] Mohan, D. and Melvin. Failure properties of passive human aortic tissue. I. Uniaxial tension tests, *J. Biomech.*, 1982, 15 (11). 887-902
- [3] Richardson P. D, Davies M.J, Born D. V. R, “Influence of plaque configuration and stress distribution on fissuring of coronary atherosclerotic plaques”, *The lancet*, Oct 21, 1989
- [4] Prediman K. Shah, “Plaque disruption and Coronary Thrombosis: New Insight into Pathogenesis and Prevention”, *Clin. Cardiol.* Vol. 20(suppl. II), II-38-II-44 (1997)
- [5] Lee R.T, 2000, “Plaque stabilization: the role of lipid lowering”. *International Journal of Cardiology*, 74, S11–S15.
- [6] Griffith, M. D., Hourigan, K. and Thompson, M.C., “ Numerically Modelling Blockage Effects on the Flow Between Flat Plates”, 15th Australasian Fluid Mechanics Conference, 13-17 December 2004
- [7] Neofytou, P., Driskakis, D., “ Non-Newtonian Flow Instability in a Channel with a Sudden Expansion”, *J. Non-Newtonian Fluid Mech.* 2003, 111. 127-150.
- [8] A. U. Coskun, Y. Yeghiazarians,, et al. “ Reproducibility of Coronary Lumen, Plaque, and Vessel Wall Reconstruction and of Endothelial Shear Stress Measurements in Vivo in Humans”, *Catheterization and Cardiovascular Interventions* 60:67-78 (2003)
- [9] Erling Falk, Prediman K. Shah, Valentin Fuster, “ Coronary Plaque Disruption”, *Circulation.* 1995; 92: 657-671
- [10] Chen G C , Loree, H M, Kamm R D, Fishbein M C, Lee T R, “ Distribution of Circumferential Stress in Ruptured and Stable Atherosclerotic Lesions: A structural Analysis with Histopathological Correlation”, *Circulation.* (1993); 87: 1179-1187
- [11] Huang H., Virmani R., Younis H., Burke A.P., Kamm R.D., and Lee R.T.,2001, “The impact of calcification on the biomechanical stability of atherosclerotic plaques”. *Circulation*, 103, 1051–1056.
- [12] Davies J M, “ A Macro and Micro View of Coronary Vascular Insult in Ischemic Heart Disease”, *Circulation* (1990); 82 (suppl II): II-38-II-46

- [13] Yamagushi T, Furuta N, Nakayama T, Kobayashi T, “Computations of the Fluid and Wall Mechanical Interactions in Arterial Diseases” 1996 Advances in Bioengineering, ASME BED (1995) ;31: 197-198
- [14] Yamagushi T, Kobayashi T, Liu H, “ Fluid-Wall interactions in the Collapse and Ablation of an Atheromatous Plaque in Coronary Arteries”, Proc. Third World Congress of Biomechanics, (1998) p. 20b
- [15] Ku, N. David, “ Blood Flow in Arteries”, Ann. Rev. Fluid Mech., 1997, 29:399-434

6. EFFECT OF PLAQUE COMPOSITION ON FSI INDEX OF PLAQUE RUPTURE

6-1- Overview

Although thin fibrous cap and large necrotic core are common features of ruptured plaques, the relation between these plaque components, coronary calcification and structural stress has not been thoroughly explored. In this section, we investigate the impact on coronary plaque rupture of fibrous cap thickness, lipid pool size and location, and calcium deposit. Physiologically realistic models of stenosed human coronary arteries with bilinear material properties are used to represent non-linear elastic properties of the diseased artery wall. The flow and stress/strain analyses are performed simultaneously. A flow–structure interaction (FSI) index γ of plaque rupture is computed by normalizing the predicted shear stress by the structural stresses.

6-2-Formulation

We consider a diseased artery model to be similar to that illustrated in Fig. 6.1. This model comprises of a channel with an obstruction representing a stenosis. The upper layer of stenosis, made of fiber and collagen, constitutes the fibrous cap. In Figure 6.1, $L = 210$ mm and $L_s = 10$ mm represent the artery and stenosis length, respectively. The model used in this study has 40% stenosis level in the range for which previous studies investigation in section 4 have shown to be highly prone to rupture .

The arterial interior nominal diameter D_i is 4 mm, and the segment proximal to the plaque is 100 mm. This segment enables the flow to be fully developed before the plaque. A similar length of straight segment is provided distal to the plaque to allow some flow recovery before the outlet. The diseased segment length is 10 mm and the wall thickness is 0.5 mm.

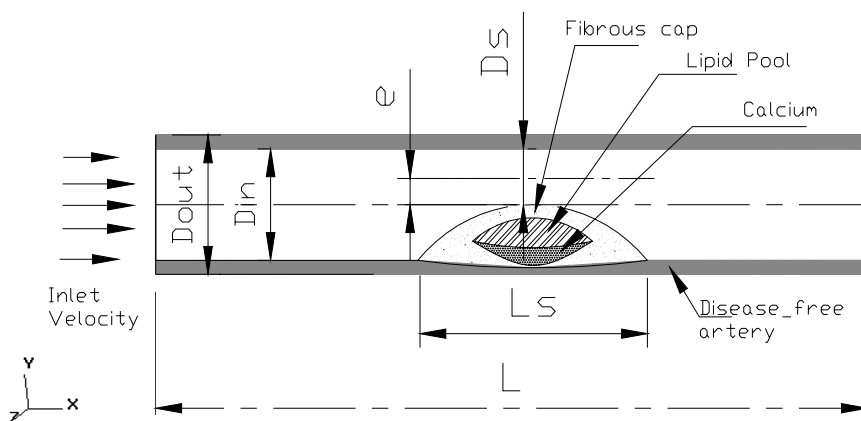


Figure 6.1: Schematic representation of stenosed artery model

A set of 5 cases were investigated for fibrous cap thickness and 4 for each of the other characteristics: lipid pool size, lipid pool location and calcium size. The fibrous cap thickness ranged from $25 \mu m$ to $300 \mu m$ with 42 % combined volume of lipid pool and calcium. For the study of lipid pool location, the fibrous cap thickness was assumed constant $t=100 \mu m$, the lipid pool volume approximately 16% of total volume of stenosis. The center of lipid core was varied from $X= 102.5$ mm to 107.5 mm in a stenosis that stretched from $X=100$ mm to 110 mm. In the cases investigating effect of lipid pool and calcium volume, the volume rates ranged from 24 % to 80% of the total stenosis volume, and the fibrous cap thickness was assumed constant at $100 \mu m$ and uniform throughout the diseased segment. The summary of the different cases investigated and values of varying parameters is presented in table 6.1.

Table 6.1 Cases investigated versus parameter values

Investigated cases	FC thickness (μm)	LP Location (mm)	LP Volume rate (%)	Ca Volume rate (%)
Fibrous cap (FC)	25 - 300	105	33	9
Lipid Pool (LP) Location	100	102.5 - 107.5	16	-
Lipid Pool Volume	100	105	24 - 80	-
Calcium (Ca) Volume	100	105	-	24 - 80

6-3- Results

The major characteristics of plaque composition affecting the stress distributions are fibrous cap thickness, lipid pool location, lipid pool and calcium volumes. All these factors are considered in this study.

6-3-1- Fluid-Flow Analysis

The typical predicted flow pattern in the lumen is presented in Fig. 6.2. The increase in diameter proximal to the diseased segment is due to the boundary conditions allowing limited radial swelling of the arterial wall under flow pressure.

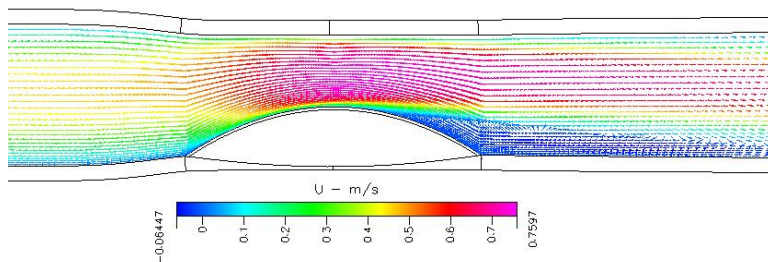


Figure 6.2: Typical flow velocity and flow re-circulations

The velocity profile is parabolic upstream of the stenosis for all the cases considered. The velocity increases within the constricted section above the stenosis with a maximum value of 0.76 m/s. A small re-circulation vortex develops in the lee region of the stenosis.

The recirculation is important because it impacts the deposition of atherogenesis constituents such as low-density lipoproteins (LDL) in the lumen. The deposition is mediated by both the low shear stress (SS) and the increased residence time of the constituents in the recirculation zone [2,3]. The resident time increases with the size of the recirculation vortex.

Figure 6.3 shows a typical distribution of endothelial shear stress (SS) from the proximal to the distal ends of the stenosis. The data used are: fibrous cap thickness, lipid pool location, lipid pool volume and calcium volume. The parameter X on the horizontal coordinate represents the position on X axis of points along the solid-liquid interface, starting from the proximal end (X=100.2 mm) to the distal end (X=110.2 mm). The vertical line represents the location of a symmetric vertical plane (SP) passing through the stenosis throat.

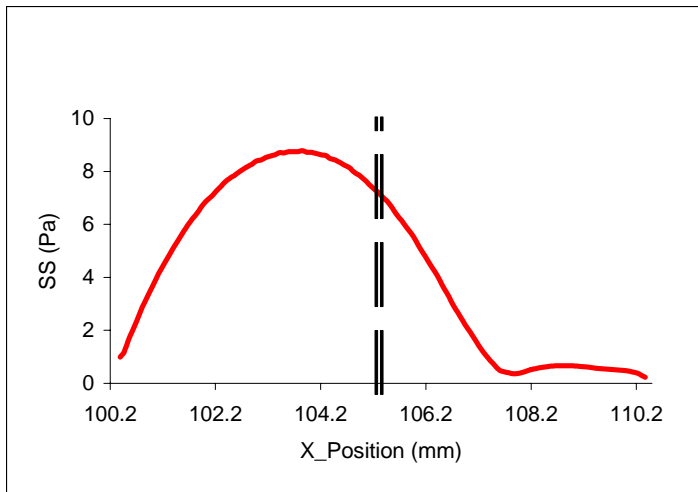


Figure 6.3: Endothelial Shear Stress (SS) plots for different stenosis rates

The predicted wall shear stress rises monotonically to a maximum upstream of the SP, and drops to the lowest value downstream before settling to a fairly constant value towards the outlet of the arterial segment. The observed trend in the wall shear stress distribution is generally consistent with previous studies [4,5]. The maximum shear stress (SS) is predicted on the plaque shoulder slightly upstream of the SP. This result is consistent with clinically observed location of plaque rupture [6,3,7,8].

6-3-2. Structural Analysis

6-3-2-1 Effect of Fibrous Cap Thickness

Typical structural stress distributions in the stenotic artery are presented in fig. 6.4 for Maximum principal stress (MPS) and in Fig. 6.5 for Von Mises stress (VMS) Two values of fibrous cap (FC) thickness, $t=50\ \mu\text{m}$ and $t=300\ \mu\text{m}$ are shown. (The results for intermediate values not shown for brevity). These results describe the total stresses that a material endures for a given applied pressure.

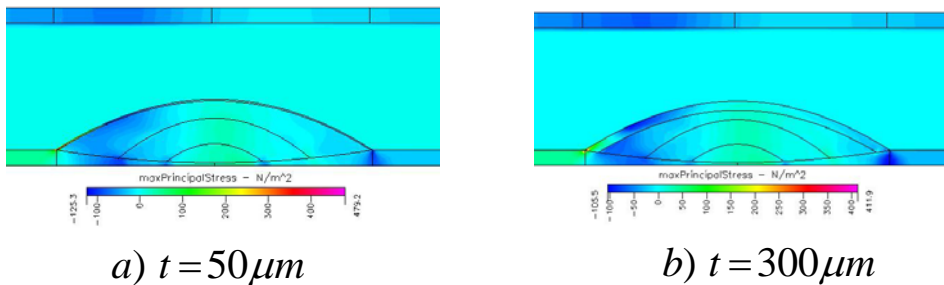


Figure 6.4: Maximum Principal Stress (MPS) distributions for different Fibrous cap thickness, t

Figure 6.4 shows that the maximum MPS decreases as the fibrous cap thickness increases. The highest MPS values are located within the mid section of the stenosis. They are approximately $100\ \text{N}/\text{m}^2$ for the thin fibrous cap (Fig. 6.4-a), and $50\ \text{N}/\text{m}^2$ for the thick one (Fig. 6.4-b). There is a succession of extensive and compressive stresses upstream of the plaque shoulder which may contribute to fibrous cap vulnerability to rupture for the specific plaque component investigated. It is worth noting that compressive stresses are higher in thin fibrous cap than thick one.

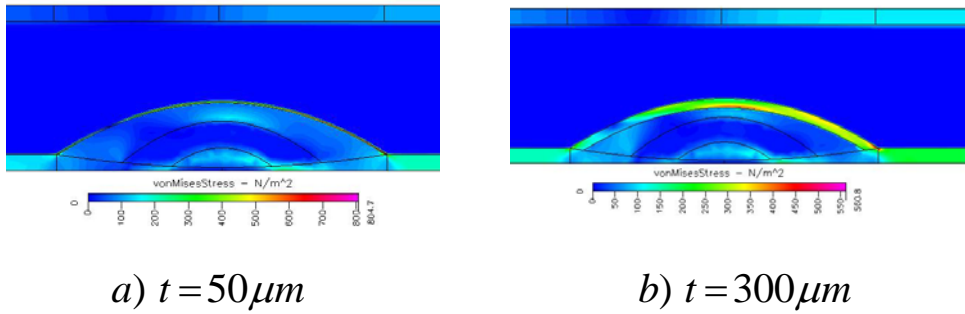


Figure 6.5: Von Mises Stress (VMS) distributions for different Fibrous cap thickness, t

Figure 6.5 shows that the maximum VMS decreases as the fibrous cap thickness increases. The highest VMS magnitudes are located within the FC, precisely at the stenosis throat and downstream of the SP. The VMS values at these locations are approximately $500 N/m^2$ for the thin fibrous cap (Fig. 6.5-a) and $350 N/m^2$ for the thick one (Fig. 6.5-b). On the plaque shoulder, upstream of the SP for all cases, there is a sharp drop in VMS magnitude expressing a discontinuity in fibrous cap deformation. This VMS drop may affect plaque vulnerability to rupture similar to the MPS results.

The stress distributions predicted from structural analysis are presented in Fig. 6.6. The figure shows the maximum principal stress (MPS) and Von Mises stress (VMS) for fibrous cap thickness ranging from $t=25\mu m$ to $300\mu m$. The horizontal axis X represents the longitudinal length along the solid-liquid interface, from the proximal to the distal ends of the stenotic ($X=100.3$ mm to 110.3 mm). The vertical coordinate represents the structural stress obtained in N/m^2 . The vertical double dash line represents the location of the vertical plane through the

throat (SP). The plaque characteristics employed are 40% stenosis enclosing 42 % of lipid pool volume and the various fibrous cap thicknesses as stated earlier.

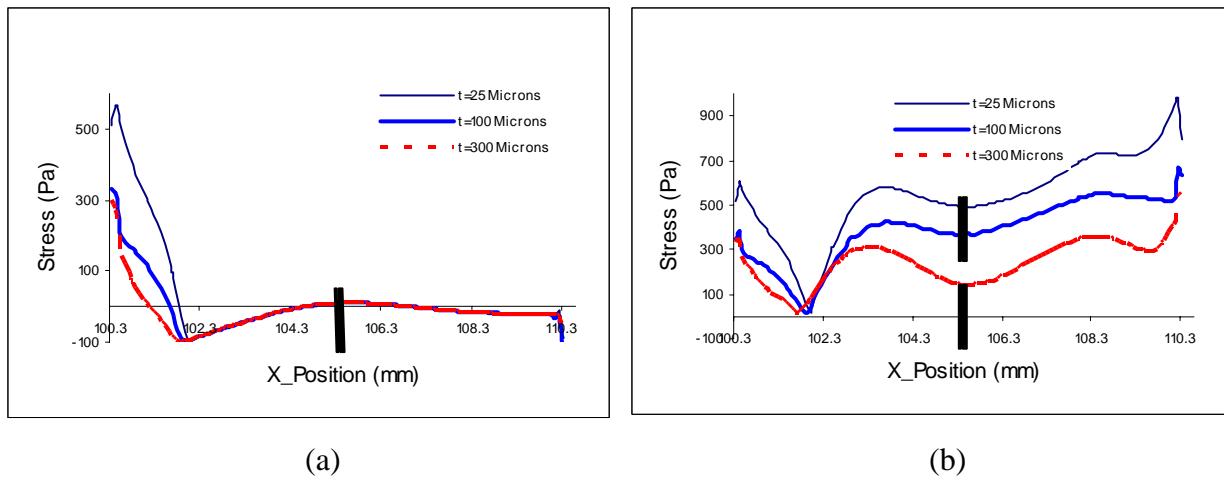


Figure 6.6: Maximum Principal Stress (MPS) (a) and Von Mises Stress (VMS) (b) distributions for different fibrous cap thickness, $t = 25 \mu m$, $100 \mu m$ and $300 \mu m$

These results indicate that within the fibrous cap, the MPS starts with high positive values at the proximal end of the stenosis and drops rapidly to negative value upstream of the SP, and then increase to a positive local maximum at the symmetric plane. The high initial value varies with fibrous cap thickness from approximately $550 N/m^2$ for $t = 25 \mu m$ to $300 N/m^2$ for $t = 300 \mu m$. The initial value is due to stress continuity with the disease-free arterial segment stretched under luminal pressure. The MPS decreases steadily in the FC downstream to the minimum (negative) values. At the latter location, the plaque undergoes compressive maximum principal stresses. The positive MPS located at the stenosis throat (SP) indicates that the plaque

undergoes extensive stresses. In general, the MPS is observed to vary with fibrous cap thickness only within the initial (1/6) section of the stenosed segment.

The Von Mises Stress (VMS) curves show two consecutive lobes or local maxima on each side of the SP. In general, the VMS decreases as the fibrous cap thickness increases. Also there is a common minimum VMS, independent of FC thickness that is located in the middle of the initial 1/3 of the stenosed segment. The minimum VMS has the same location as the minimum compressive stress shown in the MPS distribution of Fig. 6.6-a.

It is worth noting that, the highest VMS values are predicted to occur in the downstream part of the stenosis SP. Previous findings have however indicated that 60-70 % of plaque rupture occurs on the upstream of plaque shoulder [9,3,10,11]. Thus the present results indicate there is no direct correlation between plaque disruption and high VMS. A more consistent representation will be presented in subsequent sections on flow-structure interaction.

6-3-2-2 Effect of Lipid Pool Location

In this section, the lipid pool volume, representing approximately 16 % of the stenosis total volume is kept constant and the location of the lipid zone center is shifted horizontally within the stenosis from upstream to downstream (Fig. 6.7). The location of lipid pool center ranges from 102.5 mm to 107.5 mm. the fibrous cap thickness is kept constant ($t=100 \mu m$).

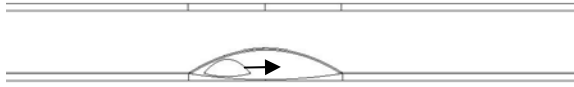
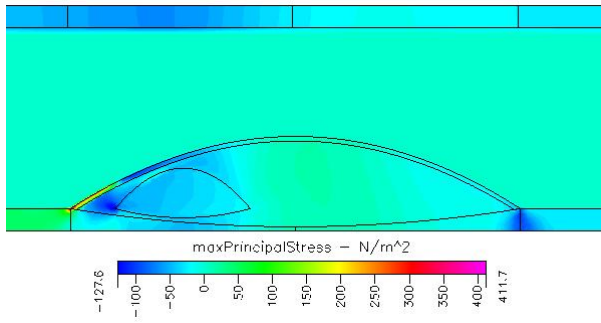


Figure 6.7: Model of stenosis. Direction of LP shifting in the stenosis (Arrow)

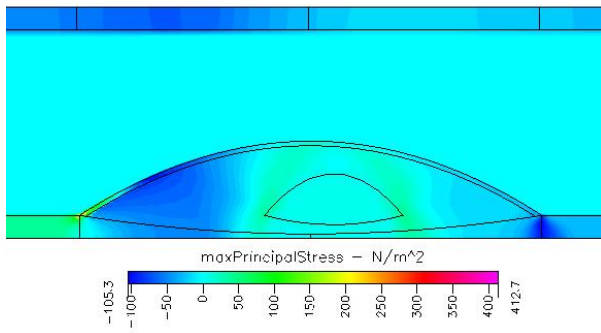
The structural stress distribution results are presented in Fig. 6.8 for Maximum principal stress (MPS) and in Fig. 6.9 for Von Mises stress (VMS). The results in each case are for models with lipid pool center located at 102.5 mm, 105.5 mm, and 107.5 mm.

Figure 6.8 shows that, in the first 1/3 section of the stenosis, the MPS is negative. Thus the stenosis undergoes compression there. We observe that the lipid pool located eccentric, in the upstream part of the stenosis exacerbates compressive stresses, but there is little impact when the lipid pool is centered or eccentric in the downstream part.

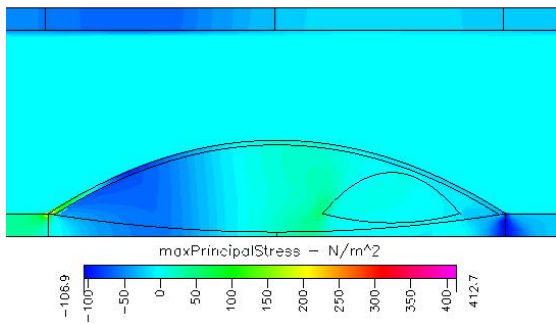
Figure 6.9 shows that highest VMS values are located downstream of the stenosis SP, and the maximum value increases as the lipid pool is shifts downstream and gets closer to the fibrous cap. There is a spot of high VMS on the upstream part of stenosis when the lipid pool is in the vicinity (Fig. 6.9-a). The results show that VMS distribution in the fibrous cap correlates with the lipid pool location.



(a)

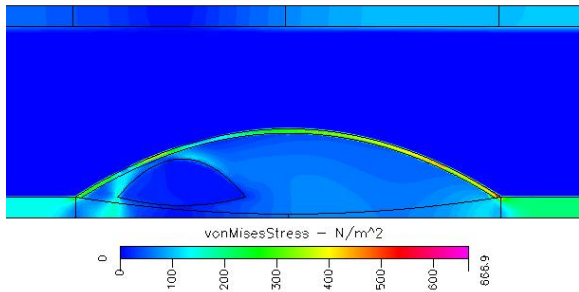


(b)

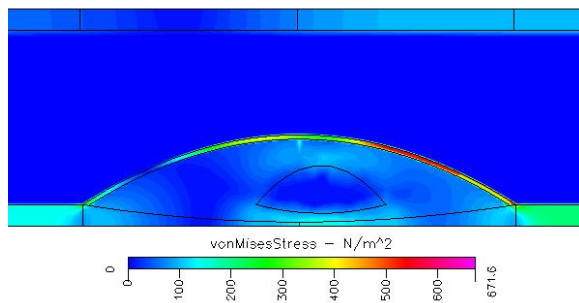


(c)

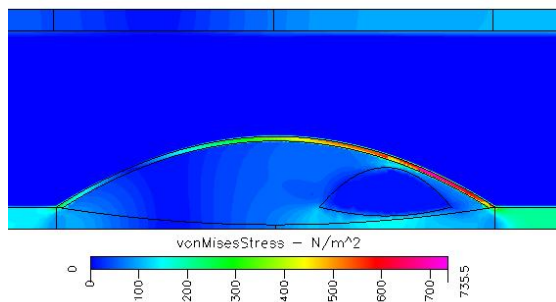
Figure 6.8: Maximum Principal Stress (MPS) distributions for models with different lipid pool positions: 102.5 mm (a), 105.5 mm (b) and 107.5 mm (c)



(a)



(b)



(c)

Figure 6.9: Von Mises Stress (VMS) distributions for different lipid pool location 102.5 mm (a), 105.5 mm (b) and 107.5 mm (c).

Figure 6.10 shows the predicted maximum principal stress (MPS) (Fig.6.10-a) and Von Mises stress (VMS) (Fig. 6.10-b) along the segment for models with lipid pool positions ranging from

102.5 mm to 107.5 mm. The horizontal axis X represents the distance from the inlet, of points selected along the segment. The SP is represented by the vertical lines in the figures.

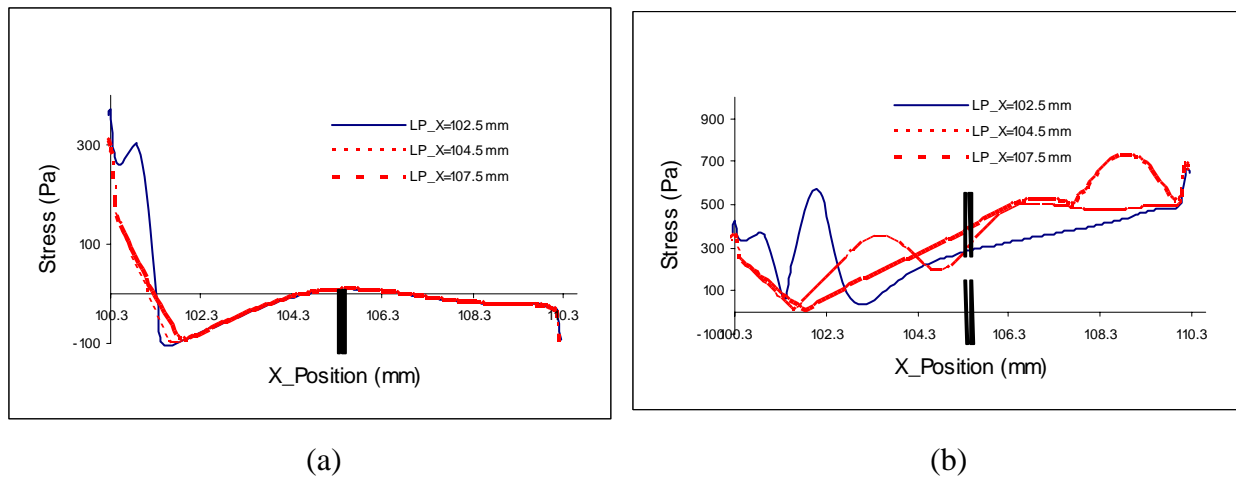


Figure 6.10: Maximum Principal Stress (MPS) (a) and Von Mises Stress (VMS) (b) distributions for different lipid pool location in 40% stenosis model

The MPS results are similar to those presented for the study of fibrous cap thickness in Fig. 6.6-a. However, there is a peak of MPS in the initial 1/6th in the stenosed segment (i.e. plaque shoulder) when lipid pool is located there. That stenosis segment is highly sensitive to the presence of the lipid pool and is the location where most plaques rupture. Therefore, MPS and lipid pool location may play important role in plaque disruption.

The VMS results show that the two lobes described in the previous section (Fig 6.6-b) are also present here. The magnitudes and locations of these VMS local optima seem to vary with lipid pool location. Specifically, the lobes are squeezed in the upstream section of the stenosis SP as the lipid pool is located eccentrically there. Then their magnitudes increase and they move along the stenosis as the lipid pool shifts downstream. The changes in local VMS optima as the lipid

pool location changes may underlie the cause of some plaque rupture at the stenosis throat rather than the plaque shoulder.

6-3-2-3 Effect of Lipid Pool / Calcium Size

Using 40% stenosis model with fibrous cap thickness of $100\ \mu\text{m}$, Fig. 6.11 shows the distribution of maximum principal stress (MPS) and Von Mises stress (VMS) in the fibrous cap for lipid pool volume rate of 24% and 80%.

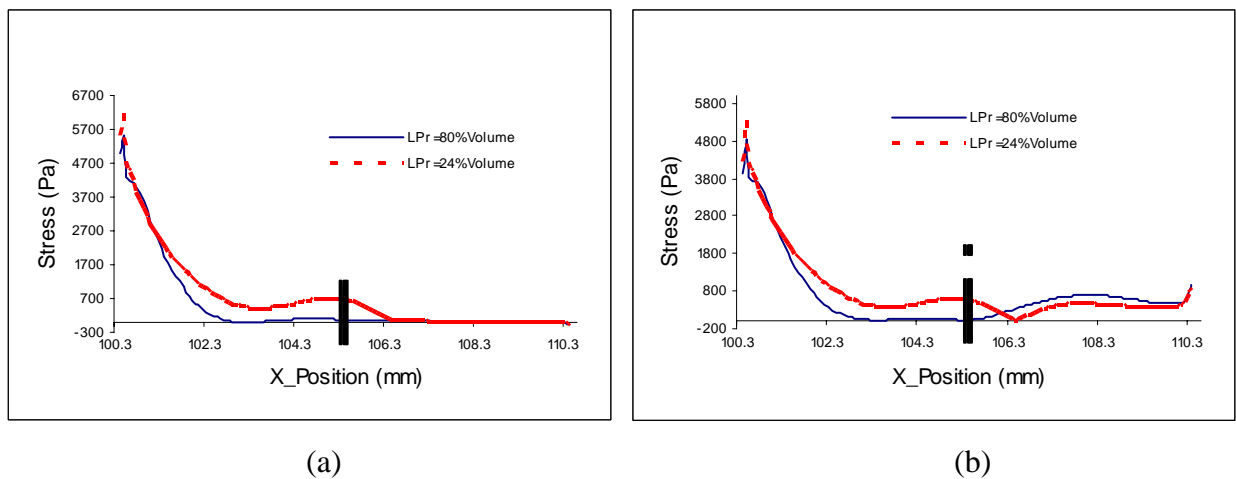


Figure 6.11: Maximum Principal Stress (MPS) (a) and Von Mises Stress (VMS) (b) distributions for different lipid pool volume rate (LPr)

The results indicate that MPS and VMS follow the same trend for both lipid pool volumes considered. The stresses are highest at the proximal part of the stenosis and drop rapidly as we progress towards the throat plane (SP). Subsequently, the change in their magnitudes is small

towards the end stenosis. The high initial value increases with relative lipid pool value. There is a local maximum for both MPS and VMS at the SP. The local maximum decreases as the lipid pool increases. That local maximum is followed by another downstream for the VMS, whereas the MPS decreases and becomes constant over the 1/3 stenosis segment.

The MPS and VMS distributions for models with calcium are presented in Fig. 6.12. Two volumes of calcium relative to plaque volume are considered. These distributions display the same patterns as those with lipid pool in the previous Fig. 6.11. In these cases, the mechanical stresses are high upstream and decrease steadily toward the downstream section of the stenosis. With the exception of the model with 80 % relative calcium volume in which the MPS and VMS are clearly low in the middle of the upstream stenosis segment, the results for other relative volumes investigated (42%, 64%) are similar.

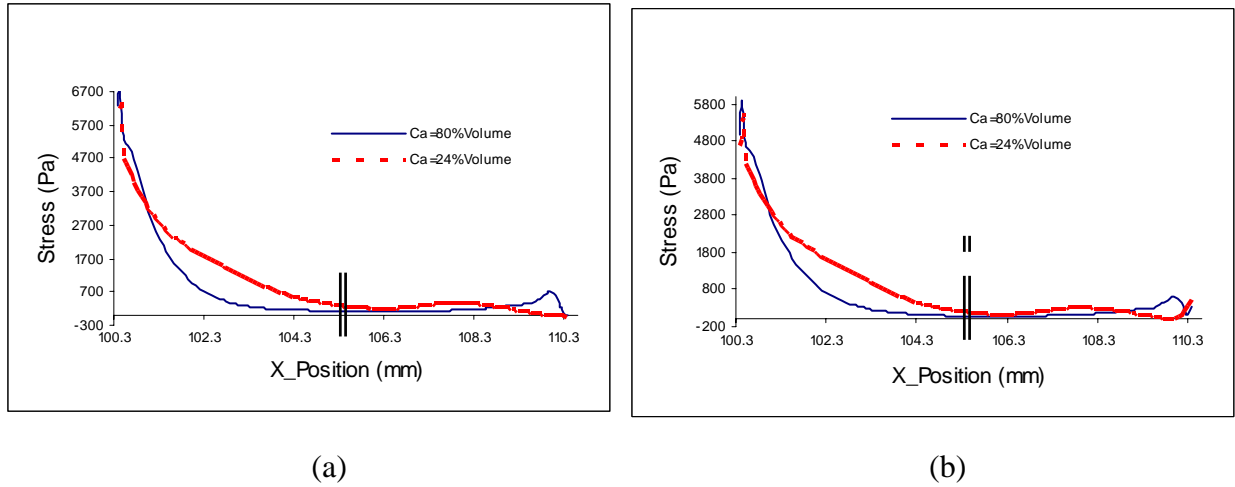


Figure 6.12: Maximum Principal Stress (MPS) (a) and Von Mises Stress (VMS) (b) distributions for for different calcium volume rates

6-3-3. Fluid Structure Interaction (FSI)

6-3-3-1. Stress Ratios

In this section, stress ratios R_1 and R_2 established in previous study are used to characterize plaque susceptibility to rupture. R_1 is the ratio of endothelial shear stress to maximum principal stress and R_2 is the ratio of endothelial shear stress to Von Mises Stress. Figures 6.13 – 6.16 shows the typical distributions of the stress ratios for various plaque characteristics (Fig. 6.13. fibrous cap thicknesses, $t=25 \mu m$ and $300 \mu m$, Fig. 6.14. lipid pool locations $X=102.5$ mm and 107.5 mm, Fig. 6.15. lipid pool volume rates, $LPr = 24\%$ and 80% , and Fig. 6.16. calcium

volume rates $Ca = 24\%$ and 80%). The ratio distributions presented here are for 40% stenosis models. The distance X is measured along the solid-liquid interface and D is the nominal diameter of the normal artery segment proximal to the lesion. The vertical mid plane of the lesion between the proximal and the distal ends is represented by the vertical double dash lines.

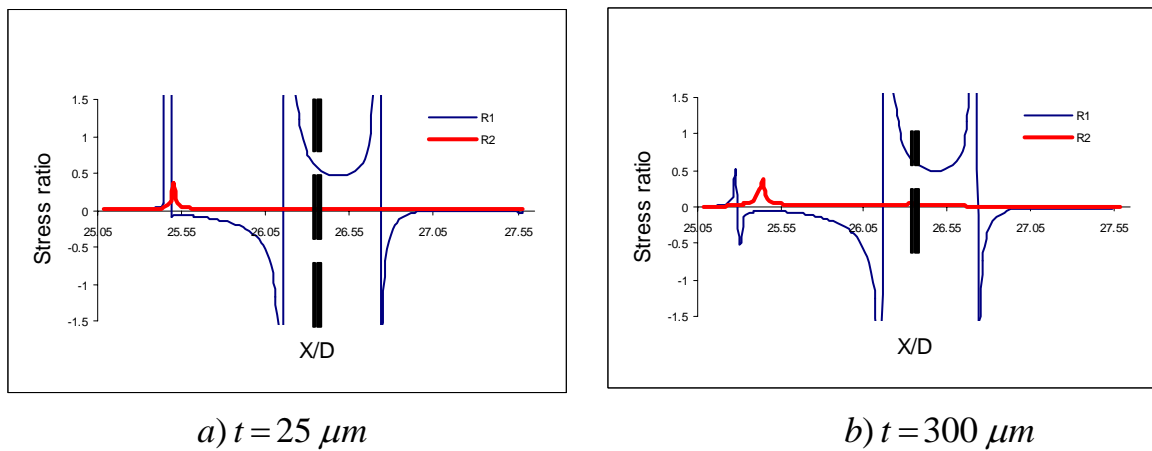


Figure 6.13: Typical Stress Ratio R_1 and R_2 for two fibrous cap thicknesses, t .

Using 40% stenosis models with 42% lipid pool and varying fibrous cap thicknesses, the results presented in Fig. 6.13 indicate that the stress ratio R_1 has multiple positive and negative peaks. These peaks are located where R_1 is infinite. R_1 is negative between the two infinities prior to the mid-plane SP due to the compressive MPS. At the SP, R_1 reaches a local minimum but remains positive. After the SP, at approximately the last $1/3$ section of the lesion, R_1 shows another discontinuity, then remains negative towards the distal end of the stenosis.

The stress ratio R_2 curve has one peak upstream of the SP. That peak is interesting because it occurs on the shoulder where plaques are most likely to rupture [3,9,10,11]

Investigation of R_1 at the location where the ratio R_2 is maximal shows that the magnitude of R_1 decreases as the fibrous thickness increases (Fig. 6.13 - a & b). In other words, the thicker the fibrous cap the stable the plaque. This result is consistent with previous studies [4,7,11] and will be described in more detail later in this section.

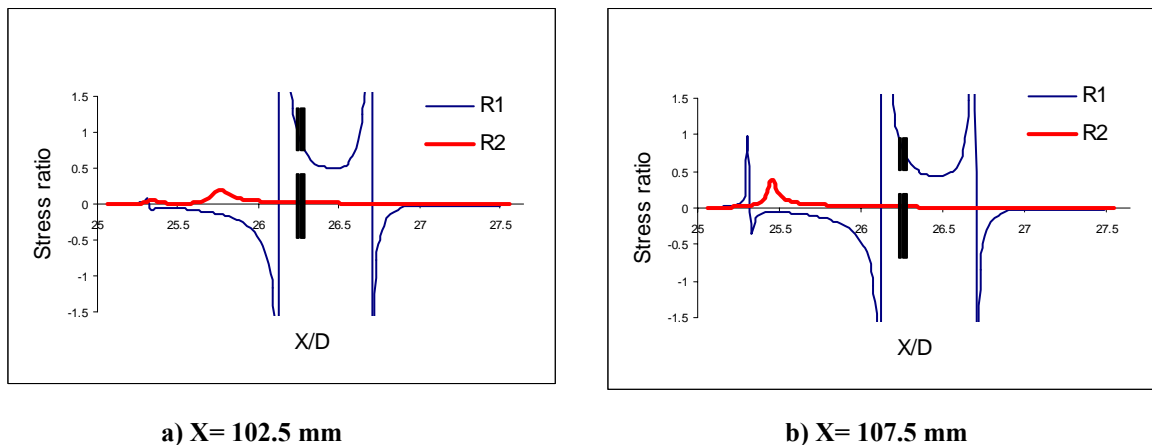


Figure 6.14: Typical Stress Ratio R_1 and R_2 for two lipid pool locations, X.

Using 40% stenosis model with 16 % lipid pool volume and fibrous cap thickness $t=100\ \mu m$, the results of variation of lipid pool locations (Fig. 6.14) display the same trend as those for fibrous cap with the exception that local R_2 maximum is now closer to the SP. Monitoring R_1 at the location where R_2 is maximal shows that R_1 magnitude decreases rapidly as the lipid pool shifts from the proximal to the distal end of the lesion. The decrease is particularly significant as

LP shifts away from the fibrous cap on the proximal part and increases slightly as the LP gets closer to the fibrous cap on the distal end of the stenosis

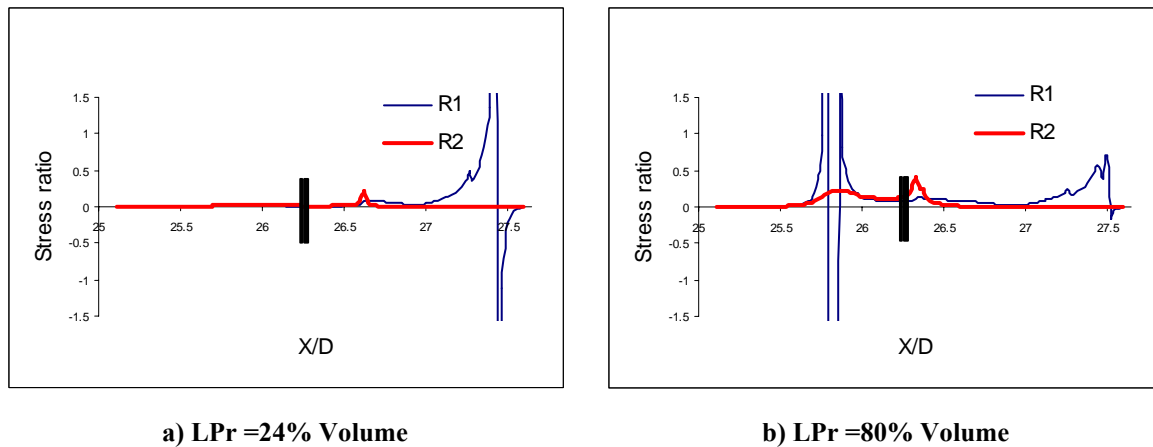


Figure 6.15: Typical Stress Ratio R_1 and R_2 for two lipid pool volume rates, LPr

For 40% stenosis model with fibrous cap thickness $t=100\ \mu\text{m}$, the results with varying lipid pool size show that small lipid pool rate the ratios R_1 and R_2 are similar upstream of the stenosis plane (SP) (Fig. 6.15-a), whereas in the Fig. 6.15-b, the R_2 distribution has two maxima, one on each side of the SP. The maximum located on the plaque shoulder (before the SP) increases with relative lipid pool volume, LPr. Similarly, at the monitored location, the R_1 distribution increases with LPr. In addition, and more importantly, on the stenosis proximal, R_1 is discontinuous for large LPr (80%) which is not the case for the smaller LPr (Fig 6.15-a). This discontinuity may cause plaque disruption. Subsequently, at locations in the downstream section of the stenosis, R_1 displays other discontinuities in all the cases investigated.

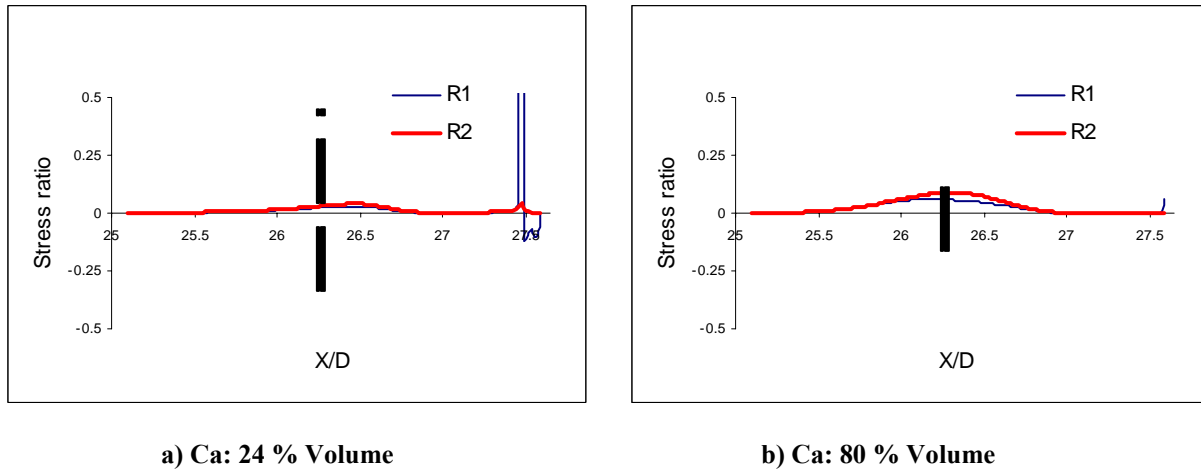


Figure 6.16: Typical Stress Ratio R_1 and R_2 for two calcium volume rates, Ca

When the lipid pool is replaced by calcium (Fig. 6.16) and the other parameters kept unchanged, R_1 and R_2 are symmetrically distributed about the SP and increase with calcium ratio. The steady continuity of the ratio R_1 distribution over the stenosis may indicate stability of calcium-rich plaques.

6-3-3-2. Summary: FSI Indices

The fluid structure interaction index that was computed to characterize the stenotic plaque rupture is summarized in Figs. 6.17, 6.18 and 6.19. The horizontal axis in each figure represents the fibrous cap thickness (Fig.6.17), lipid pool positions (Fig. 6.18) and volume ratios of lipid pool or calcium (Fig. 6.19). The vertical axis in each case represents the FSI index γ , which is

the stress ratio R_1 at the monitored location, specifically, the X/D where the ratio R_2 is maximum.

The effect of variation of fibrous cap thickness is presented in Fig.6.19. The predicted FSI distribution can be divided into three parts based on the slopes. The first and third parts are characterized by high slope, and comprise plaques with FC thickness of $25 \mu m$ - $100 \mu m$ and $200 \mu m$ - $300 \mu m$. The middle second part is characterized by low slope with FC thickness in the range $100 \mu m$ to $200 \mu m$. The FSI index γ decreases as the plaque fibrous cap thickness increases. This result is reasonable and consistent with clinical studies indicating that thinner fibrous caps are more prone to rupture [7,12,10].

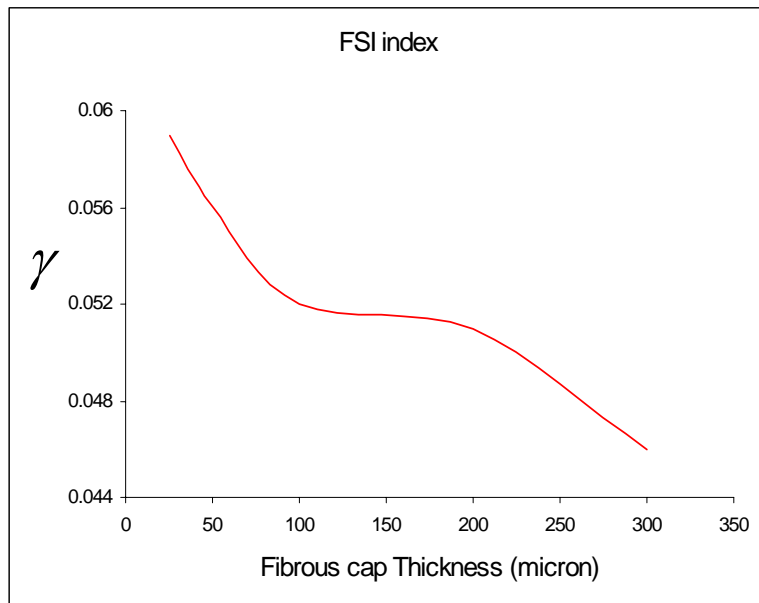


Figure 6.17: FSI index γ as a function of fibrous cap thickness

Figure 6.18 summarizes the effect on FSI index γ of varying the location of the lipid pool. The magnitude of γ decreases rapidly as the lipid location shifts from the proximal to the distal part of the stenosis. It reaches the minimum when the center of the lipid pool zone is located symmetrically at the SP plane passing through the throat. Subsequently, as the lipid pool shifts closer to the fibrous cap downstream, the magnitude of γ increases but only slightly. The results indicate that, lipid pool will have greater impact on plaque rupture when located closer to the fibrous cap at both ends of the stenosis. The impact on plaque rupture is however higher when it is located in the upstream than the downstream part of the stenosis. The results are with clinical findings that most plaques (60%-70%) rupture at the upstream part of the stenosis and contain eccentric necrotic core.

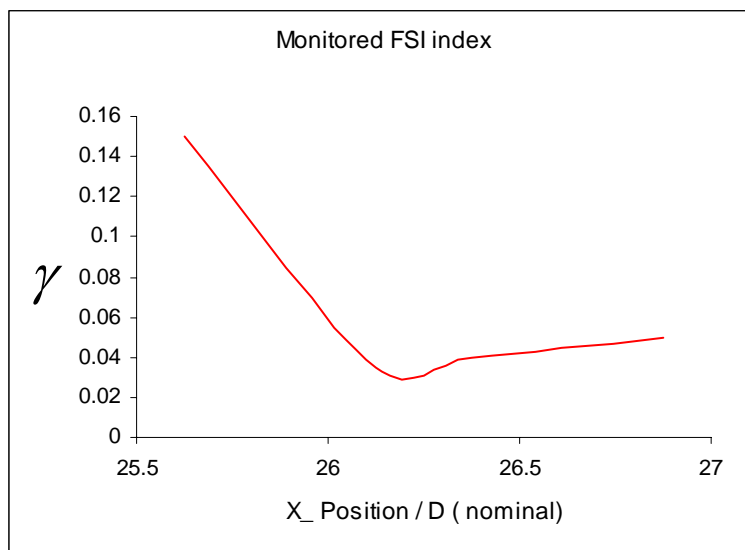


Figure 6.18: FSI index γ as a function of lipid pool location within the stenosis

The results summarizing the effects of relative lipid pool volume Φ_{lp} and relative calcium volume Φ_{Ca} are presented in Fig. 6.19. These results show that γ increases with lipid pool volume as observed in previous clinical studies [6,7]. It is important to note that the rate of increase of γ is highest when γ exceeds 60%, in the consensus of clinical observations [7,13]. When the lipid pool is replaced by calcium, γ increases with relative calcium volume (Φ_{Ca}) but at much lower rate than that for lipid pool. The results suggest that lipid-rich plaques are more susceptible to rupture than those filled with calcium deposit. In addition, Calcium deposits may indeed slow down the cataclysm effects of lipid pool in the lesion. Such effect of calcium is attributed to its high elastic modulus capable to withstand large part of pressure coming from hemodynamic force otherwise supported by the fibrous cap only when plaque is filled with lipid pool.

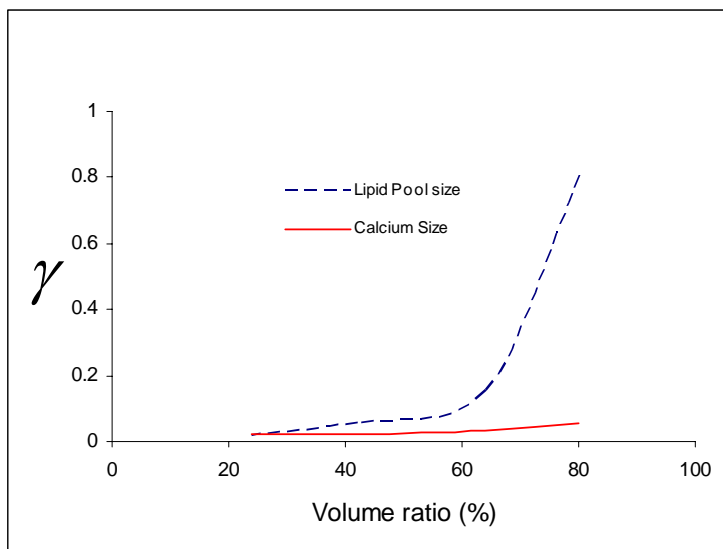


Figure 6.19: FSI index γ as a function Lipid pool / Calcium percentage of total stenosis volume

6-4- Closing Remarks

Stress distributions within the arterial wall and lesion are important in understanding the plaque disruption mechanism. Areas of high biomechanical stress are important diagnostic tools in determining the plaques that are prone to rupture. Calcification and lipid pool are commonly found in atherosclerotic lesions, and their presence is associated with poor disease prognosis. By using the methodology presented in this study of examining the relationship between fibrous cap thickness, necrotic core, calcium deposits and biomechanical stress distribution in the plaque and combining with conventional imaging tools (MRI, CT scan, OCT) plaques that are susceptible to rupture may be identified.

For models with relative lipid pool volume higher than 50% of stenosis, the distribution of stress ratio R_1 show discontinuities on the plaque shoulder which may be responsible for plaque disruption. On the other hand, in models with calcium, the stress ratio at the monitored location is continuous and symmetrically distributed about the symmetric plane (SP).

Our findings suggest that FSI index γ can be used to predict the propensity of a plaque to rupture. Indeed, γ decreases as the fibrous cap thickness increases which is consistent with clinical studies that found that thin fibrous caps are more prone to rupture than thick ones [4,7,10,12]. In addition, γ predicts that plaque susceptibility to rupture is affected by its embedded lipid pool, size and location. In particular, a plaque is more prone to rupture when the lipid pool is large and located closer to the fibrous cap at the proximal end of stenosis. The extent

of vulnerability is much higher for plaques with relative lipid volume greater than 60% of stenosis. Our results demonstrate that the presence of calcium does not correlate directly with plaque rupture. In fact, calcium deposits within the stenosis may slow down fibrous cap tearing by hardening the lesion. These results are consistent with previous studies [6]

The results presented here have potential implication in the evaluation and intervention of coronary events. For instance, clinical intervention on identified calcified lesions may not be as significant as preventing lipid-rich plaques to rupture. Our findings are consistent with the relative success of lipid lowering therapies in the prevention of plaque disruption [1]. Lipid lowering by reducing the volume of the necrotic core dramatically decreases the biomechanical stress to be withstood by the fibrous cap.

6-5- References

- [1] Vaughan C.J., Gotto AM Jr., Basson CT, “ The Evolving Role of Statins in the Management of atherosclerosis”, J Am Coll Cardiol. 2000; 35: 1-10
- [2] Zhenjun Hu “In ViVo Characterization of Human Coronary Artery Flow”, Ph.D. Thesis, Northeastern University 2000
- [3] Lindmark Eva, 2002, “ Leukocytes and Coronary Artery Disease: Experimental and Clinical Studies”, Doctoral Thesis, Acta Universitatis Upsaliensis, Uppsala
- [4] D. Tang, C. Yang, S. Kobayashi, D. N. Ku, “Effect of a Lipid Pool on A Stress/Strain Distributions in Stenotic Arteries: 3-D Fluid-Structure Interactions (FSI) Models” J. Biomech. Eng.,126, 2004, pp. 363-370
- [5] Nosovitsky A. V., Ilegbusi J. O., Jiang J., Stone H. P., Feldman C. L., 1997, “Effects of the Curvature and Stenosis-Like narrowing on Wall Shear Stress in
- [6] Huang H., Virmani R., Younis H., Burke A.P., Kamm R.D., and Lee R.T.,2001, “The impact of calcification on the biomechanical stability of atherosclerotic plaques”. Circulation, 103, 1051–1056.
- [7] Shah, K. Predima, 2003, “Mechanisms of Plaque Vulnerability and Rupture”, Journal of the American College of Cardiology, 41,(4), 15S-22S
- [8] Kamm, R. D., Pedley, T.J., “ Flow in Collapsible Tubes: A Brief Review”, Journal of Biomechanical Engineering, August , 111, 177-179 (1989)
- [9] Hall et al., Ann. Biomed. Eng.volume, 26 (1):28-36, 1998
- [10] Erling Falk, Prediman K. Shah, Valentin Fuster, “ Coronary Plaque Disruption”, Circulation. 1995; 92: 657-671
- [11] Ross R., 1999, “Atherosclerosis – an Inflammatory Disease” N. Engl J Med. (340); 2:115-126.
- [12] R. Virmani, F.D. Kolodgie, A.P. Burke, A. Farb and S. M. Schwartz, 2000, “Lessons From Sudden Coronary Death: A Comprehensive Morphological Classification Scheme For Atherosclerotic Lesions “, Arteriosclr Thromb Vasc Biol. 20, 1262–1275.

- [13] Suzanne A. Sorof, “Intravascular Atheroma Monitoring: Past , Present and Future of identifying Vulnerable Plaques”, 2004, Applications in Imaging. Cardiac interventions. pp 34-39

7. EFFECT OF VASCULAR REMODELING ON FSI INDEX

7-1- Overview

Despite extensive studies on plaque disruption, stenosis growth within the arterial walls has not been thoroughly examined. Indeed, more recently, clinical observations have shown that atherosclerotic lesions develop slowly and often remain clinically silent for many years [1, 2]. In this section, we will attempt to address this issue by investigating the flow, structure and Fluid-Structure Interaction effects and the impacts of these parameters on the FSI index of plaque rupture.

7-2- Formulation

In addition to the models described in the section (3-1), here, we consider both inward remodeling (IR) and outward remodeling (OR) with eccentric stenosis, different stenosis severities and a lipid pool in the plaque as illustrated in Figures 7.1. For the Inward Remodeling (IR) model, the stenosis grows from the inner surface towards the artery axis, such that the plaque simply lies over the intima. For Outward Remodeling (OR), the stenosis grows from the inner surface towards the outer surface, and the plaque encroaches on the arterial wall.

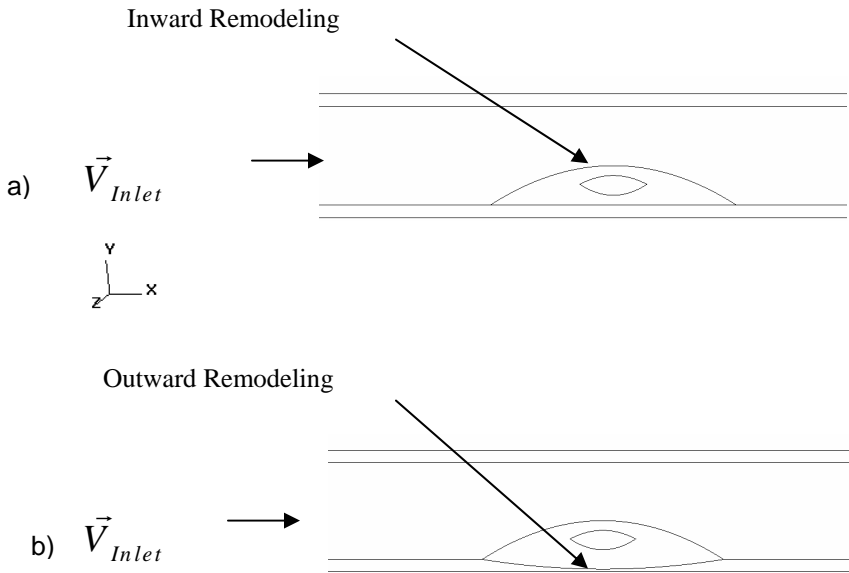


Figure 7.1: Schematic sketch of arterial segments with inward (a) and outward (b) remodeling

7-3- Results

7-3-1 Flow Analysis

Our computational results have shown there is no significant difference in shear stress and pressure distributions between inward and outward remodeling. This is not surprising since remodeling is associated directly with change in the material structure. In our outward remodeling model, the channel geometry remains unchanged in order to maintain the same

stenosis rate to permit comparison between the various cases considered. Thus, we will focus here on the results of structural analysis and fluid-structure interaction.

7-3-2 Structural Analysis

The stress distributions predicted from structural analysis are presented in Figure 7.2. The figure shows the maximum principal stress (MPS) and Von Mises stress (VMS) for 40% stenosis. Fig. 7.2-a presents results for inward remodeling (IR) cases, and Fig. 7.2-b presents those for outward remodeling (OR) cases. The horizontal axis X represents the point positions along on the solid-liquid interface. The vertical double dash represents the location of the symmetric vertical plane (SP) passing through the top of the stenosis.

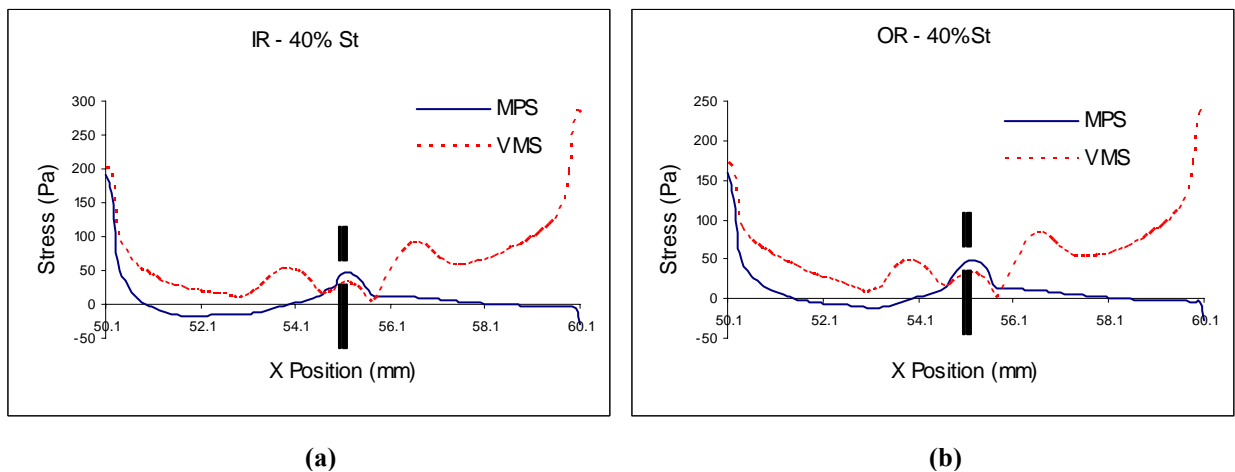


Figure 7.2: Maximum Principal Stress (MPS) and Von Mises Stress (VMS) distributions for Inward Remodeling (I.R.) and Outward Remodeling (O.R.) cases

The Figure presents the same trend as in the previous section (Establishing the FSI index: 4-3-2). Here, the MPS and VMS distributions of outward remodeling (OR) display similar trend to those of inward remodeling (IR). However, structural stresses of OR are smaller compared to those of IR. The reduction is attributed to the increase in the volume of the diseased segment due to outward remodeling. For VMS, the reduction varies from 1% to 13% on both sides of the SP and 3% to 6% on the stenosis throat. For MPS, it varies from 10% to 29% and 5% to 20% on the previously indicated locations respectively. Note that the highest percentage reductions for VMS and MPS pertain to moderate stenosis (~40%).

7-3-3 Fluid Structure Interaction Flow Analysis

7-3-3-1 Stress Ratios

In this section, we attempt to investigate outward and inward remodeling effects on plaque rupture using fluid-structure interaction (FSI) index that characterizes plaque. The parameters identified for investigation are the stress ratios R_1 and R_2 . The parameter R_1 is the ratio of shear stress to maximum principal stress and R_2 is the ratio of shear stress to Von Mises Stress. Figure 7.3 shows the distributions of the ratios R_1 and R_2 for 40% stenosis of inward remodeling (IR) on the left and outward remodeling (OR) on the right. The distance X is measured along the solid-liquid interface.

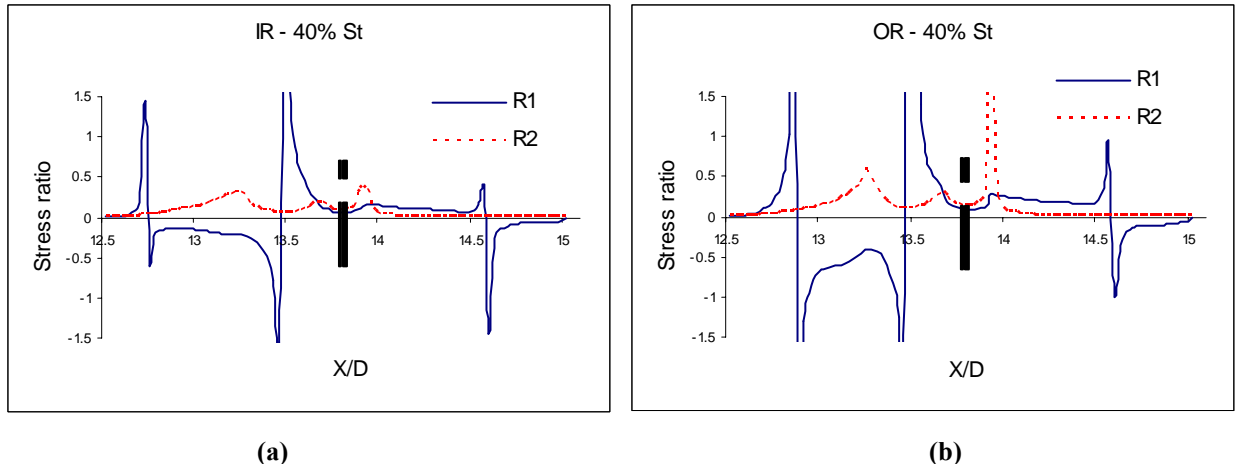


Figure 7.3: Ratios R_1 and R_2 with $P_{out} = 0$ Pa for Inward Remodeling (I.R.) and Outward Remodeling (O.R.) cases

The results for Inward Remodeling indicate that the stress ratio R_1 has multiple positive and negative peaks. These peaks are located where R_1 is infinite. This trend is expected since the Maximum Principal Stress (MPS) is zero at these locations. The parameter R_1 is negative between the two infinities prior to the mid-plane SP due to the compressive MPS. Between the peak before and on the SP, R_1 is low and positive for moderate ($\sim 40\%$) and severe ($\sim 70\%$) stenosis but remains negative for native ($\sim 20\%$).

The stress ratio R_2 curves have two peaks upstream of the SP and one downstream. We will focus on the first optimum because it occurs on the shoulder where plaques are most likely to rupture [3,4], and also the ratio R_1 changes with the stenosis level at the location.

Both ratios R_1 and R_2 of outward remodeling (OR) exhibit similar trends to the Inward remodeling (IR) plots on the left. However, in general, the ratios of OR are higher than their counterparts of IR. This result is due the decrease of structural stress in stenosed segment of OR as explained previously.

7-3-3-2 Summary: FSI Indices

The fluid structure interaction parameters that we computed to characterize the stenotic plaque vulnerability are summarized in Fig. 7.4. The horizontal axis represents the percentage stenosis, and the vertical axis represents the monitored stress ratio. Specifically, the plots represent the values of R_1 at monitored locations for stenosis levels of 20%, 30%, 40%, 50% and 70% stenosis. The monitored locations are X/D positions where the first R_2 maximum occurred upstream of the SP. The monitored R_1 values for both inward and outward remodeling are presented in Fig. 7.4 for comparison.

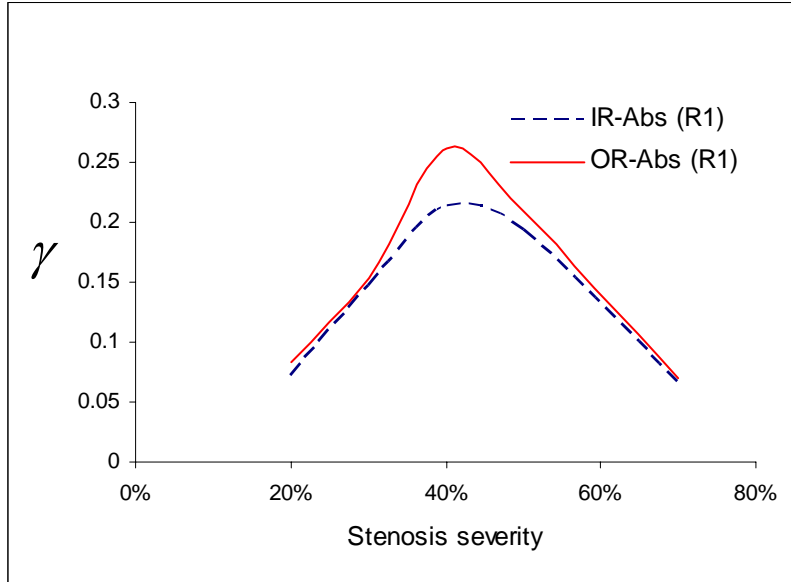


Figure 7.4: FSI index γ as a function of stenosis rate for OR and IR

The results show that the Fluid structure interaction (FSI) index γ for both cases (OR and IR) is low for mild (e.g. 20%) and severe (e.g. 70%) stenosis. Interestingly, this index reaches it's a maximum between these extreme stenosis levels, at approximately 40%-45% stenosis rate. Note that this stenosis range could be considered vulnerable to rupture as it is consistent with medical observations suggesting that most myocardial infarction patients have less than 50% stenosis [1,2].

An experimental study is greatly needed to establish the stability value of R_{1_CR} (Critical value)

The results also show that the FSI index γ for outward remodeling (OR) is consistently larger

than for inward remodeling (IR). This trend can be attributed to the reduction of structural stresses in stenosed segment for OR compared to that for IR.

7-4- Closing Remarks

The results show that Outward Remodeling (O.R.) and Inward Remodeling (I.R.) exhibit similar velocity and shear stress distributions. However, structural stress values are quantitatively different. Structural stresses are relatively smaller in OR than IR models. In order to establish the effect of OR on FSI index γ of plaque vulnerability to rupture, we used to the parameters R_1 and R_2 , and found that the FSI index γ gives the same trend as predicted in the previous section (4). Both OR and IR models show that stenosis levels in the range 40%-45% are most vulnerable to rupture. In addition, OR seem to slightly exacerbate plaque potential to rupture.

7-5- References

- [1] Erling Falk, Prediman K. Shah, Valentin Fuster, “ Coronary Plaque Disruption”, *Circulation*. 1995; 92: 657-671
- [2] Suzanne A. Sorof, “Intravascular Atheroma Monitoring: Past , Present and Future of identifying Vulnerable Plaques”, 2004, *Applications in Imaging. Cardiac interventions*. pp 34-39
- [3] Huang H., Virmani R., Younis H., Burke A.P., Kamm R.D., and Lee R.T.,2001, “The impact of calcification on the biomechanical stability of atherosclerotic plaques”. *Circulation*, 103, 1051–1056.
- [4] Kamm, R. D., Pedley, T.J., “ Flow in Collapsible Tubes: A Brief Review”, *Journal of Biomechanical Engineering*, August , 111, 177-179 (1989)

8. GENERAL CONCLUSION AND RECOMMENDATIONS

8-1- Overview

Analysis of fluid flow and structural dynamics of stenotic models of coronary arteries is crucial to understanding the process of plaque disruption and rupture. In the clinical studies, Falk et al. [1] show that 68 % of myocardial infarction (MI) patients have moderate stenoses (less than 50% stenosis), implying they had little or no symptom prior to heart attack. Prediman [4] suggests that disrupted plaques have a large, often eccentrically located, soft lipid-rich core that constitutes more than 40% of the plaque volume, and 50 to 60% of plaque disruptions occur on the shoulders of the plaque. In the stress analysis of plaque rupture, Huang et al.[7] demonstrate that the lipid pool size dramatically increases stresses but calcification does not decrease the mechanical stability of the coronary plaque.

A fluid-structure interaction (FSI) approach has been used by Tang et al. [8,9] considering the important role the arterial wall compliance and pulsatile blood flow in atheroma rupture [10]. The results show the occurrence of a pattern of maximum tensile stress and compressive stress in the stenotic section, and demonstrate that stress-strain distributions over the plaque are affected by lipid pool size, shape and location, fibrous cap thickness, and pressure. These findings are summarized in the Table 8.1. In spite of the intense interest on this subject, the diverse mechanisms responsible for destabilizing the fibrous cap and that lead to plaque disruption have not been systematically explored.

The ultimate goal of this research is to provide a physician with a useful tool to accurately assess critical determinants of arterial plaque rupture. Thus, this research uses numerical modeling to define for the first time, a flow-structure interaction (FSI) index γ for assessing the effects of plaque characteristics and patient-specific data on atherosclerotic plaque rupture. The controlling parameters were the inflow velocity, plaque size, material properties, stenosis shape, plaque composition and mechanical boundary conditions. The lipid pool model investigated allowed assessment of changes in stress response in the fibrous cap. The numerical results were obtained by using a commercial package (CFD ACE GUI-FSI). This package has been used and validated for similar biomedical systems [11,12].

In the following, we summarize the major conclusions of the study starting, with section (8.2) on the establishment of the Fluid-structure interaction (FSI) index γ of plaque rupture. Section (8.3) considers the effect of blood pressure on FSI index and section (8.4) involves the effect of plaque composition on FSI index. In section (8.5), the effect of plaque remodeling on FSI index is considered. Section (8.6) presents a table summarizing the result. Finally, section (8.7) describes the limitations and recommendations to improve the present study.

8-2- Establishing the Fluid- Structure Interaction (FSI) Index of Plaque Rupture

Our results show that structural stresses (Maximum principal stress, MPS, Maximum shear stress, MSS, Von Mises stress, VMS, and lateral stress, SZZ) increase with the stenosis levels. In order to establish a critical index of plaque rupture γ , we use the analogy of the investigated

system to buckling in material failure studies. Specifically, we normalized the endothelial shear stress (SS) obtained from the flow model by the above structural stresses for analysis. We predicted the parameters R_1 and R_2 expressing the ratio of endothelial fluid shear stress to Maximum Principal stress and Von Mises stress respectively, or alternatively, R_3 and R_4 , the ratio of endothelial fluid shear stress to maximum structural shear stress and lateral (reminiscent of circumferential) stress in the plaque respectively. We found that monitoring the R_1 values (or alternatively, R_4 values) at the vicinity of its discontinuity, specifically on the plaque shoulder at the location where the ratio R_2 (or R_3) distribution is maximum, predicts that stenosis levels in the range 40%-45% are most at risk to rupture. This observation is consistent with the critical stage of lipid-laden [1,2,3].

8-3- Effect of Blood Pressure on FSI Index

Our results suggest both the endothelial shear stresses and biomechanical stresses are affected by changes in the arterial pressure. While the endothelial shear stress generally increases with pressure, the variation in the structural stresses depends on the specific location within the plaque.

The stress ratios R_1 and R_2 are affected by the arterial pressure. Specifically, the two successive inflexions of R_1 upstream of the throat plane SP seems to close up with increase in pressure drop.

This result implies a reduction in the section of the plaque that is subjected to compressive stress at high pressure, which may weaken the plaque.

Investigation of the effect of pressure on plaque rupture shows that about 40%-45% stenosis range remains the most susceptible to rupture. In addition, other plaques which otherwise are less critical at normal blood pressure (< 40%) enter the threshold of vulnerability to rupture at high pressures. These results suggest that high arterial pressure may indeed accelerate early atherosclerotic plaque disruption; consistent with previous studies that high blood pressure contributes to acute cardiovascular events [13, 9].

8-4- Effect of Plaque Composition on FSI Index

Our findings suggest that FSI index γ can be used to predict the propensity of a plaque to rupture. Indeed, γ decreases as the fibrous cap thickness increases which is consistent with previous studies that found that thin fibrous caps are more prone to rupture than thick ones [2,3,4,6,9]. In addition, γ predicts that plaque susceptibility to rupture is affected by its embedded lipid pool, size and location. In particular, a plaque is more prone to rupture when the lipid pool is large and located close to the fibrous cap at the proximal end of stenosis. The extent of vulnerability is much higher for plaques with relative lipid volume above 60% of stenosis within the census of previous studies that suggest that disrupted plaques have large, eccentrically located, soft lipid-core core that constitutes more than 40% of plaque volume [4]. Our results demonstrate that the presence of calcium does not correlate directly with plaque rupture. In fact,

calcium deposits within the stenosis may slow down fibrous cap tearing by hardening the lesion. These results are consistent with clinical observations [7].

8-5- Effect of Artery Remodeling on FSI Index

Outward Remodeling (O.R.) and Inward Remodeling (I.R.) exhibit similar velocity and shear stress distributions. However, structural stress values are quantitatively different. Structural stresses are relatively smaller in OR than IR models. The FSI index γ predicts for both OR and IR models that stenosis levels in the range 40%-45% are most vulnerable to rupture. In addition, OR seems to slightly exacerbate plaque potential to rupture, consistent with ward et al. findings [5].

8-6- Summary of the Results

The findings of relevant literature and the results of the present study are summarized in the following Table 8.1.

Table 8.1 Summary of relevant literature and present study

Authors	Methods	Results
Falk et al. [1] (1995) Fuster et al. [2] (1996) Sorof[3] (2004)	Clinical Study: angiography studies	* 68 % of myocardial infarction (MI) patients have moderate stenoses (less than 50% stenosis), meaning they had no or little symptom prior to heart attack
Prediman S. [4] (1997)	Clinical Study: In vitro studies of intact and ruptured plaques	* Disrupted plaques have a large, often eccentrically located, soft lipid-rich core that constitutes more than 40% of the plaque volume. * 50 to 60% of plaque disruptions occur on the shoulders of the plaque
Ward et al. [5] (2000)	Clinical Study: In vivo intravascular Ultrasound and angiography studies	*Adequate outward remodeling may increase the risk of plaque rupture

Authors /Years	Methods	Results
Loree et al. [6] (1992)	Stress Analysis: -2D cross sectional models -Linear elastic material -Uniform pressure	* Increase of stenosis severity by increasing the fibrous cap thickness reduced the maximum circumferential stress
Huang et al [7] (2001)	Stress Analysis: -2D model -Mooney-Rivlin materials -more plaque constituents (fibrous cap thickness, lipid pool and calcium)	* Lipid pool dramatically increases stresses but calcification does not decrease the mechanical stability of the coronary plaque
Tang et al. [8,9] (2001 & 2004)	Fluid-structure interaction (FSI): -3D model -Mooney Rivlin materials -Lipid pool core	*Occurrence of pattern of maximum tensile stress and compressive stress in the stenotic section *Stress-strain distributions over the plaque are affected by lipid pool size, shape and location, fibrous cap thickness, and pressure
Teuma (2006) Present thesis	Fluid-structure interaction (FSI): -2D Longitudinal model -Bilinear materials -High Blood Pressure -Fibrous cap Thickness -Lipid pool volume & location -Calcium volume -Plaque remodeling	Establish a critical index of plaque rupture γ that predicts that: * Stenosis levels in the range 40%-45% are most at risk to rupture * High arterial pressure may indeed accelerate early atherosclerotic plaque disruption * Thin fibrous caps are more prone to rupture than thick ones * Plaque is more prone to rupture when the lipid pool is large (>60% stenosis volume) and located close to the fibrous cap at the proximal end of stenosis * Presence of calcium does not correlate directly with plaque rupture * Outward remodeling (OR) slightly exacerbates plaque potential to rupture

8-7- Recommendations

Endothelial Shear stress plays a pivotal role in platelet deposition and plaque growth. Structural stresses (Maximum principal stress, Von Mises stress and circumferential stress) are also important in understanding atherosclerotic plaque disruption. However, accurate computation of stress patterns in living tissues can be tricky because of the difficulty in quantifying the impact of geometry (morphology) and structural (material properties, etc.) variables. Changes in these variables have to be monitored and be accounted for in the interpretation of the results.

A number of simplifying assumptions were made in the study. The stenosis segment used were the two dimensional comprising the lipid pool, fibrous cap and calcium. Real plaques are more complex and contain additional features such as smooth muscle cells, microphage infiltration, etc. All materials used here were assumed to be homogenous and isotropic while a real artery wall is non-homogeneous, multi-layered and anisotropic. The flow was assumed to be steady and the lateral biomechanical stress acting as the hoop (circumferential) stress. Although these assumptions might have impacted the magnitude of the stresses, they were not expected to significantly affect the general trend of the stress distribution. In fact, the steady analyses may simulate the critical end diastolic stage of the cardiac cycle and the spatial biomechanical stress obtained in this study represents the complete spectrum of stress expected in 3-D model.

Validation of the critical index γ developed here would require further studies that relax some of the simplifying assumptions, coupled with systematic experimentation and validation. It should

also be applied to more of the known risk factors of cardiovascular disease including thin fibrous cap, large necrotic core, high blood pressure, smoking, high cholesterol levels, macrophages effects etc. Since FSI index γ is a function of multiple variables, future work can be modeled using optimization technique by investigating which combination of parameters may be critical to plaque rupture.

8-7- References

- [1] Falk, E., Prediman K. Shah, Valentin Fuster, “ Coronary Plaque Disruption”, *Circulation*. 1995; 92: 657-671
- [2] Fuster. V, Badimon J, Chesebro JH, et al. “ Plaque rupture, Thrombosis, and Therapeutic Implications”, *Haemostasis*. 1996; 26(suppl 4): 269-284.
- [3] Sorof. S., “Intravascular Atheroma Monitoring: Past , Present and Future of identifying Vulnerable Plaques”, 2004, *Applications in Imaging. Cardiac interventions*. pp 34-39
- [4] Prediman K. Shah, “Plaque disruption and Coronary Thrombosis: New Insight into Pathogenesis and Prevention”, *Clin. Cardiol*. Vol. 20(suppl. II), II-38-II-44 (1997)
- [5] Michael R. Ward, Gerard Pasterkamp, Alan C. Yeung, Cornelius Borst, “Arterial Remodeling: Mechanisms and Clinical implications”, *Circulation*. 2000; 102:1186-1191
- [6] Loree H M, Kamm Roger D, Stringfellow R G and Lee R T, “ Effects of Fibrous Cap Thickness on Peak Circumferential Stress in Model Atherosclerotic Vessels” , *Circulation Research*; (1992), Vol. 71, 4; 850-858
- [7] Huang H., Virmani R., Younis H., Burke A.P., Kamm R.D., and Lee R.T., 2001, “The impact of calcification on the biomechanical stability of atherosclerotic plaques”. *Circulation*, 103, 1051–1056.
- [8] Tang, D., Yang, C., Kobayashi, S., Ku, N.D., 2001, “Steady Flow and Wall Compression in Stenotic Arteries: A Three-Dimensional Thick-Wall Model with Fluid-Wall Interactions,” *Journal of Biomechanical Engineering*, 123, pp. 548–552
- [9] Tang, D., Yang, C., Kobayashi, S., Ku, N.D., 2004, “Effect of a Lipid Pool on A Stress/Strain Distributions in Stenotic Arteries: 3-D Fluid-Structure Interactions (FSI) Models” *J. Biomech. Eng.*, 126, pp. 363-370
- [10] Yamagushi T, Furuta N, Nakayama T, Kobayashi T, “Computations of the Fluid and Wall Mechanical Interactions in Arterial Diseases” 1996 *Advances in Bioengineering, ASME BED* (1995) ;31: 197-198
- [11] Johnston, M. B., Johnston, R. P., Corney, S., Kilpatrick, D., 2004, “ Non-Newtonian Blood Flow in Human Right Coronary Arteries: Steady State simulations,” *Journal of Biomechanics*, 37, pp. 709-720

[12] Kudriavtsev, V., Kawano, S., et al., “Numerical study on fluid-structure interaction in VFP artificial heart with jelly-fish valve”, Proceedings of FEDSM’03, 4th ASME JSME Joint fluids Engineering Conference, July, 2003

[13] American Heart Association, American Stroke Association, “Heart Disease and Stroke Statistics” 2005 update

APPENDIX
ANALYSIS OF UNSTEADY FLOW IN A CONSTRICTED
COLLAPSIBLE TUBE MODEL OF A DISEASED ARTERY

A-1- Summary

The unsteady flow in a collapsible tube model of a diseased artery is solved analytically. The novelty of our approach is that the set of governing equations is reduced to a single integro-differential equation in the transient state. The equation was solved using the finite difference method to obtain the pressure and compliant wall behavior. The analytical approach is less computer-intensive than solving the full set of governing equations. The predicted membrane deflection is quite large at low inlet velocity, suggesting possible approach to breakdown in equilibrium. As the transmural pressure increases with wall deflection, bulges appear at the ends of the membrane indicating critical stage of stability, consistent with previous studies. An increase in wall thickness reduces the wall deflection and ultimately results in its collapse. The collapse is due to breakdown in the balance of wall governing equation. An increase in internal pressure is required to maintain membrane stability.

A-2- Literature Review

A-2-1 Presentation of the Study

Vessels conveying fluids throughout the human body are elastic and deform primarily in response to the pressure exerted on them by the flow. Fluid flow in deformable thin-wall channels has been widely studied due to its practical relevance. For instance, such a flow situation can simulate flow in respiratory and urinary system. Analytical models can, in general, be used to study the interaction between the structure and fluid flow in coronary arteries, coronary disease growth and plaque vulnerability.

A compressive transmural pressure leads to the collapse of vessels. The vessels experiencing such a phenomenon are the vein above the heart, the coronary arteries during the systole and the airways during forced expiration [1]. The early theoretical investigations by Katz et al [2] and Conrad [3], despite reproducing flow characteristics, were unable to predict details of the wall deformation. Some deformable channels involve collapsing tube walls, and the channel experiences transverse displacements. In such cases, transverse displacements of an initial axisymmetric tube may result in a non-axisymmetric tube deformation. Such a process is illustrated in Fig. A.1. Flow in collapsible tubes have been thoroughly reviewed in Kamm and Pedley [4].

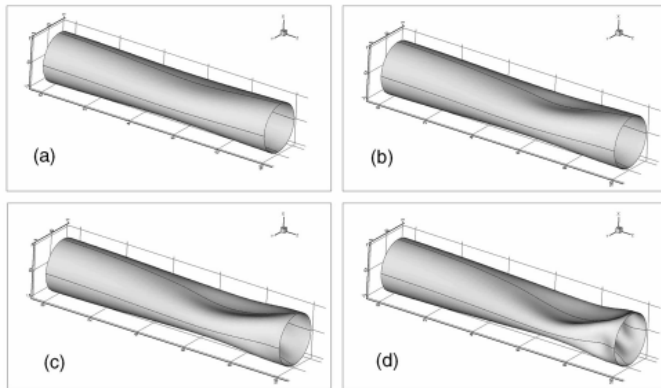


Figure A.1: 3D Collapse and buckling of a tube. External compression increases and tube wall progressively collapses from panel (a) to panel (d) [5]

There are many ways to model flow in collapsible channel with elastic wall behavior. The flow can be steady, with low Reynolds number and neglected inertia, meaning there is slow variation in the direction of the flow. Such a situation is also referred to as lubrication type flow [6]. Unsteady flow in which variations in the flow direction are significant is called Stokes type flow [6]. In this case, the Reynolds number is typically high and inertia is taken into consideration. The full Navier Stokes equations must be solved in such situation, requiring numerical analysis. The elastic channel walls are usually modeled using the membrane specifically thin-shell theory, with negligible bending stiffness.

In a recent publication [5], Grotberg and Jensen have summarized several methods of modeling flow in flexible tubes. Furthermore, observing that almost all vessels carrying fluids in the body are flexible, the significance of interactions between an internal fluid and wall deformation was established. Because fluid –structure interaction process involves a large range of flows – mechanical phenomena, they review recent advances in understanding the fundamental

mechanics of such an interruption, and discuss physiological applications including the cardiovascular system, the respiratory system and other parts of the body. The study is categorized into two parts. The first part describes the advances in single-phase flow in collapsible tubes and channels in regards of theory, experiment and biological applications. The second part is devoted to multiphase flows in flexible tubes. They conclude that despite intense investigations, the diverse mechanics generating instabilities in single-phase flow through a flexible tube remain only partially understood. Therefore, there is a need for more systematic investigations that will shed light on generic relationships and behaviors relevant to 3D experiments, and physiological applications carefully accounting for the mechanical properties of tissues.

The problem raised by fluid flow through flexible tubes with relatively thin walls is theoretically challenging and practically significant. The theoretical challenges are due to the interaction between the fluid flow and the elastic channel walls. Thus, fluid flow and structural parameters have to be computed simultaneously. In addition, the boundary conditions cannot be completely defined in advance, due to the continuously evolving boundary. The practical significance of these problems are considerable, in particular in bioengineering and biomedical because of their pivotal role in describing fluid flow in living organs including cardiovascular, respiratory, urinary systems [5].

A-2-2- One Dimensional Analysis

Diverse situations can be encountered in fluid flow in collapsible channels. Such situations have been extensively studied. Shapiro [7] investigated one-dimensional model of steady flow in a partially collapsed thin-walled tube. The model depends only on axial coordinate x and time t . The relationship between cross sectional area and transmural pressure difference is characterized by a “tube law” [7], which describes the tube’s deformation. $p_m(x) - p_{ext} = \mathfrak{R}[A(x)]$, where $p_m(x)$ is the local transmural pressure and $A(x)$ the local cross sectional area. The study analyses the effects of friction, lengthwise variations in external pressure, variations in elevation, wall stiffness, and mechanical properties. It assumes that the breakdown of steady flow correlates with the fall to zero of longitudinal tension in the tube walls. The studies of 1D models as that of Shapiro [7] contribute to note that the steady flow cannot exist in a collapsible tube under flow velocity as high as the speed of propagation of small amplitude pressure waves. Under these conditions, phenomenon of choking and unsteady takes place.

A-2-3- Two Dimensional Analysis

In order to analyze more realistic models of the problem while avoiding the complexities and computational requirements of fully three-dimensional equations, several authors have investigated the two-dimensional equations of the collapsible tube problem [8,9,10,11]. The zero

Reynolds number steady flow or finite Reynolds number unsteady flow, in which part of rigid wall was replaced by an elastic membrane, was considered.

Pedley [12] investigated that assumption (the breakdown of steady flow [7]) using lubrication theory in a symmetric 2-D channel. Membrane theory was used to define the collapsible part of the tube. The resulting non-linear ordinary differential equations were solved numerically. The results suggest that reducing the longitudinal tension in the channel wall causes it to become more deformed for the same flow rate and external pressure. Therefore, the wall slope is predicted to be significant when the downstream tension is very small.

Similarly, Djordjevic et al. [13] conducted a 2-D study of two cases of steady, viscous flow in a collapsible channel. The first case involved low Reynolds number or lubrication type flow, and the second case treat relatively high Reynolds number or boundary layer type flow. The elastic channel wall behavior was modeled by a geometrically non linear Karman shell theory. In each case, a single integro-differential equation is derived to describe the wall configuration. The governing equation was numerically solved using finite difference method. The results of wall configuration based on control parameters variations presented in Fig. A.2 show that steady flow exists in all the cases. The wall configuration depends on the control parameters.

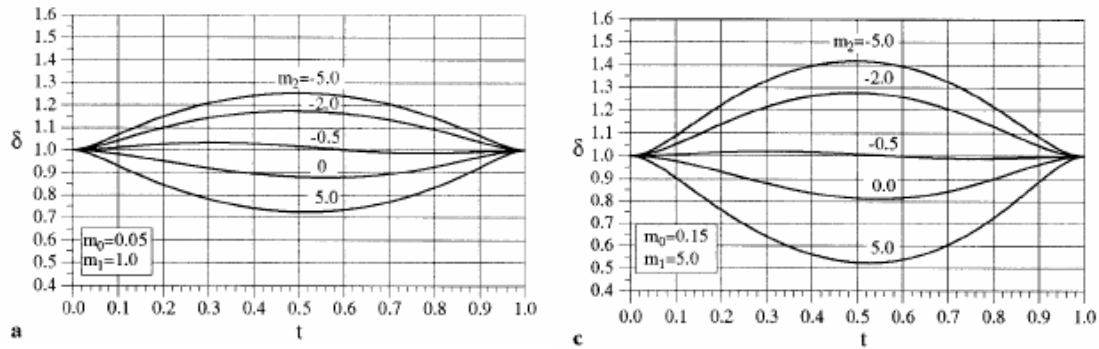


Figure A.2: Wall motion using the lubrication flow theory for different control parameters [13], Note that, t the non-dimensional coordinate of the collapsible channel and δ the non-dimensional position inside the collapsible segment channel. The parameter m_o is related to the wall thickness, m_1 to the segment length, m_2 to the pressure at the inlet.

A-2-4- Thee Dimensional Analysis

Studies on collapsible tube have evolved in modeling more complex situations; the steady deformations of the fully three dimensional system were developed [14,15]. The tube wall was modeled as a circular cylindrical shell and geometrically non linear shell theory was used to model its large non-axisymmetric deformation (post buckling). The fluid flow was modeled using lubrication theory assuming low Reynolds numbers and a small wall slope in the direction of the flow.

Heil [1] investigated the problem of viscous flow in an elastic tube. The elastic wall behavior of the tube was modeled using geometrically non-linear shell theory. Finite element methods were used to solve the fluid-structure interaction associated with the steady 3-D Stokes equations

governing the slow viscous flow. The lubrication theory satisfactorily predicts the flow traction and it is computationally easier to handle than the full Navier-Stokes equations. The computational predictions were supported by experiments.

In general, if a fluid flows through a flexible channel and induces oscillation of the conduit walls, this could be a source of atherosclerotic stretch, lasting as long as the flow continued at a sufficient speed and, eventually the fibrous cap may rupture. Pedley [16] investigated this mechanism using flow through collapsible arteries. More recently, using perturbation and numerical methods, Shankar and Kumaran [17], examined the drag reduction in gel-lined tubes and other surfaces. The fluid was considered Newtonian and two models were studied. On the first model, the flexible wall was represented as a spring-backed, plate-membrane-type wall and, the second model used an incompressible viscoelastic solid of finite thickness. Asymptotic analysis in the limit of high Reynolds number for Couette flow passing through the flexible tube indicates that the wall modes are always stable if the plate-membrane wall move only normal to its surface and are unstable when a tangential deformation occurs. In addition, using scaling analysis, they show that the wall mode instability under high Reynolds number depends only on the velocity gradient of the base flow at the wall. Similar results are found with a second model of flow passing through a viscoelastic medium, indicating that instability is independent of the wall model used to represent the flexible wall.

Different models of flow in tubes have been addressed with the pivotal parameter being the transmural pressure, defined as the pressure differential between external and internal pressure. If

this pressure differential is negative the channel experiences internal pressure, giving it, a spherical shape. If the pressure differential is positive the model walls collapse. Models with spherical shape have been studied by Shah and Humphrey [18]. The study investigated specific mechanics responsible for the genesis, enlargement, and rupture of intracranial saccular aneurysm. Based on previous studies suggesting that the elastodynamics may be important, and assuming that intracranial saccular aneurysm is dynamically unstable in response to pulsatile loads, the equation of motion was derived for an idealized sub-class of saccular aneurysm. This equation for the first time accounts for three important characteristics of the elastodynamics: finite strain, nonlinear elastic behavior of the wall, and possible reactive effects due to the cerebral spinal fluid that often surrounds aneurysms. The numerical predictions indicate that the sub-class of lesions is dynamically stable, both in response to periodic pressure and against perturbations to such stability.

A-2-5- Organization of the Analytical Study

Due to the complexity of the equations governing the fluid flow and wall configuration, many previous researchers have studied steady flow problems in order to reduce the number of control parameters [7,12,16]. Other studies considering unsteady flow problems employed finite element method to solve the governing equations [1,10]. Application of finite element method in the type of problem considered is complicated by the variety of competing factors including interpolations at the nodes of discretized elements, strain-displacement relation, stress-strain calculation, element equilibrium equations, global equilibrium equations, etc ... [20].

In this study we consider a 2-D model of collapsible tube to investigate coronary artery flow. Specifically, we study the effects of peristaltic flow through a geometrically non-linear elastic tube, whose walls deform due to the transient transmural pressure. The arterial wall motions result in strong fluid-structure interaction.

Unsteady 2D Stokes equations will be used to analyze the fluid flow under lubrication-type theory. The analytical solutions for the problem yield in an integro-differential equation. This governing equation will be solved by finite-difference numerical method. Control parameters such as inlet velocity, transmural pressure and wall thickness will be derived and used to illustrate the flow characteristics and predict wall motions.

A-3- Method

A-3-1- Overview

In this section, the unsteady interaction of fluid flow and structure in a collapsible channel is solved analytically. Transmural pressure distribution on the channel wall is determined from lubrication theory. The non linear Karman plate theory is used to express the wall elastic behavior. A single integro differential equation is derived for the first time, governing the membrane behavior in the transient state. The equations for pressure and compliant wall are solved using finite difference methods. This analytical approach differs from the relatively expensive application of finite element method as in previous studies.

A-3-2- Geometry

Consider an idealized symmetrical diseased artery (Figs. A.3 & A.4) through which an incompressible, viscous fluid is flowing. This 2-D model is inspired from Djordjevic and Vukobratovic's [13] model where the flow is assumed to be fully developed at the entrance $x^* = 0$ of the segment and remains laminar throughout. Thus the velocity profile in the segment is independent of Reynolds number. The artery wall configuration is driven by stresses acting on the surface. The elastic wall configuration is assumed to be a plate. Thus both wall inertia and fluid inertia are represented in the calculation.

We employ lubrication theory, assuming small wall slope and negligible wall inertia [12,13]. The segment has length l^* comprising parallel compliant walls with elasticity modulus E . In Fig. A.3, x^* and y^* are the Cartesian coordinates, $u^*(x^*, y^*, t^*)$ and $v^*(x^*, y^*, t^*)$ are the velocity components in x^* and y^* directions, respectively, and $p^*(x^*, y^*, t^*)$ is the pressure. The parameters ρ , ν and p_a are the density, kinematic viscosity and ambient or external pressure respectively. The parameter p_o is the constant entrance pressure at $x^* = 0$, u_o the average entrance velocity, $\delta^*(x^*, t^*)$ the arbitrary position of the channel wall with respect to direction x^* and time t^* , and $\alpha(x^*, t^*)$ is the angle between the bending wall and the principal axis x^* . The asterisks (*) denotes dimensional parameters that will be nondimensionalized later.

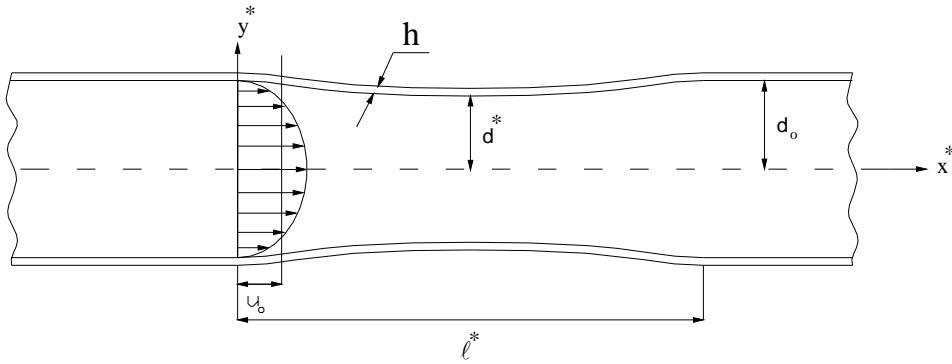


Figure A.3: 2-D model of collapsible channel

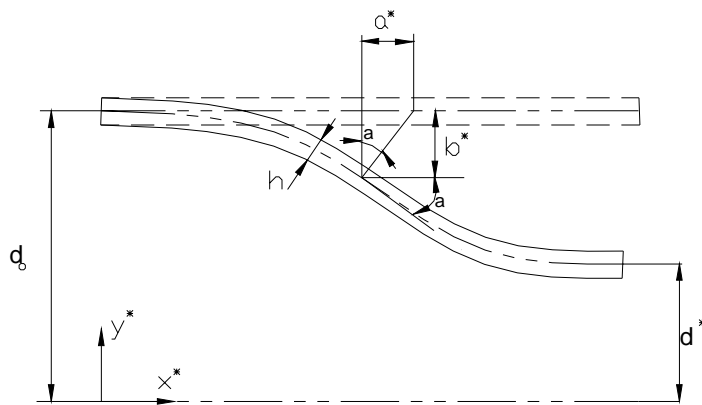


Figure A.4: Segment of channel wall

A-3-3- Governing Equations – Fluid Flow

The incompressible pulsatile flow is modeled using time-dependent, Navier-Stokes equations for Newtonian fluids coupled with the continuity equation. The equations are non-dimensionalized using u_o, δ_o, p_o and t_o as scales for velocities, lengths, pressure and time, respectively. The non-dimensional equation can be expressed thus:

$$\frac{1}{\sqrt{\varepsilon}} \frac{\partial u}{\partial t} + u \frac{\partial u}{\partial x} + v \frac{\partial u}{\partial y} = -Eu \frac{\partial p}{\partial x} + \frac{1}{Re} \left(\frac{\partial^2 u}{\partial x^2} + \frac{\partial^2 u}{\partial y^2} \right), \quad (\text{A.1})$$

$$\frac{1}{\sqrt{\varepsilon}} \frac{\partial v}{\partial t} + u \frac{\partial v}{\partial x} + v \frac{\partial v}{\partial y} = -Eu \frac{\partial p}{\partial y} + \frac{1}{Re} \left(\frac{\partial^2 v}{\partial x^2} + \frac{\partial^2 v}{\partial y^2} \right), \quad (\text{A.2})$$

$$\frac{\partial u}{\partial x} + \frac{\partial v}{\partial y} = 0, \quad (\text{A.3})$$

Where the nondimensional parameters $x = x^*/\delta_o$, $y = y^*/\delta_o$, $u = u^*/u_o$, $v = v^*/u_o$, $t = t^*/t_o\sqrt{\varepsilon}$, $t_o = \delta_o/u_o$ is the time scale, $Eu = p_o/\rho u_o^2$, and $Re = u_o\delta_o/\nu$ are Euler number and Reynolds number, respectively. $\delta_o/l^* \ll 1$, $\alpha_{\max} \ll 1$, The transmural pressure p is

$$p(x, y, t) = \frac{p_a - p^*(x^*, y^*, t^*)}{p_o}, \quad (\text{A.4})$$

where p_o and p_a are the reference and atmospheric pressures respectively.

The above Navier-Stokes equations will be simplified using the following assumptions: the stenosed segment of the channel is relatively long, ($\delta_o/l^* \ll 1$), and the maximum angle of the slope of the stenosis with respect to the x^* -axis $\alpha_{\max} \ll 1$. The latter two conditions imply slow change of the internal diameter of the channel along the principal axis. The relatively small inclination of the stenosis implies that all the physical quantities related to the structure will be subject to very small variation in the direction of the principal axis. The flow is assumed to be fully developed throughout the channel. Thus the velocity component in the flow direction is large compared to the traverse component.

We translate slow variations by introducing a slow coordinate $\xi = \varepsilon x$ and we write the transverse velocity component in the form $v = \varepsilon V(\xi, y, t)$, where $V = O(1)$ and $0 < \varepsilon \ll 1$ will be defined later. We also assume that $\delta_o/l^* = O(\varepsilon)$ and $\alpha_{\max} = O(\varepsilon)$, $p(x, y, t)$, the space and time-varying transmural pressure (outer atmospheric pressure minus inner fluid pressure) is much smaller than the reference pressure p_o which is of the order 10^5 Pa according to Kobayashi et al [22]. We assume that the transmural pressure is transmitted through the wall alone. This condition can be formulated as $p = \varepsilon^n P(\xi, y, t)$, $P = O(1)$, where the parameter $n > 1$ will be defined later.

In terms of the new parameters, the Navier-stokes and continuity equations become

$$\frac{1}{\sqrt{\varepsilon}} \frac{\partial u}{\partial t} + \varepsilon \left(u \frac{\partial u}{\partial \xi} + V \frac{\partial u}{\partial y} \right) = -\varepsilon^{n+1} Eu \frac{\partial P}{\partial \xi} + \frac{1}{\text{Re}} \left(\varepsilon^2 \frac{\partial^2 u}{\partial \xi^2} + \frac{\partial^2 u}{\partial y^2} \right), \quad (\text{A.5})$$

$$\frac{\varepsilon}{\sqrt{\varepsilon}} \frac{\partial V}{\partial t} + \varepsilon^2 \left(u \frac{\partial V}{\partial \xi} + V \frac{\partial V}{\partial y} \right) = -\varepsilon^n Eu \frac{\partial P}{\partial y} + \frac{\varepsilon}{\text{Re}} \left(\varepsilon^2 \frac{\partial^2 V}{\partial \xi^2} + \frac{\partial^2 V}{\partial y^2} \right), \quad (\text{A.6})$$

$$\frac{\partial u}{\partial \xi} + \frac{\partial V}{\partial y} = 0. \quad (\text{A.7})$$

We consider the flow to be lubrication-type i.e. the fluid is flowing with a very slow motion and frictional forces are larger than inertial forces. The latter assumption implies that Reynolds number is low. In order to exploit the lubrication approximation, we make the following substitutions into equations (A.5,A.6,A.7).

$$\frac{1}{Eu} = \varepsilon^{n+1}, \quad \frac{1}{\text{Re}} = \lambda = O(\varepsilon^k), \quad (\text{A.8-a,b})$$

where $0 < k < 1$ and $Re = O(1)$.

Keeping terms of up to order ε^2 , we obtain

$$\frac{1}{\sqrt{\varepsilon}} \frac{\partial u}{\partial t} + \varepsilon \left(u \frac{\partial u}{\partial \xi} + V \frac{\partial u}{\partial y} \right) = -\frac{\partial P}{\partial \xi} + \lambda \frac{\partial^2 u}{\partial y^2} + O(\varepsilon^2), \quad (\text{A.9})$$

$$\sqrt{\varepsilon} \frac{\partial V}{\partial t} = -\frac{1}{\varepsilon} \frac{\partial P}{\partial y} + O(\varepsilon^2), \quad (\text{A.10})$$

$$\frac{\partial u}{\partial \xi} + \frac{\partial V}{\partial y} = 0. \quad (\text{A.11})$$

Equations (A.9,A.10,A.11) have to be solved subject to the boundary conditions

$$y = \delta(t, \xi): u = 0, V = \frac{\partial \delta^*}{\partial t^*} = \frac{1}{\varepsilon^{\frac{3}{2}}} \frac{\partial \delta}{\partial t}, \quad (\text{A.12})$$

$$y = 0: \frac{\partial u}{\partial y} = \frac{\partial^3 u}{\partial y^3} = \frac{\partial^4 u}{\partial y^4} = \dots = 0, V = 0. \quad (\text{A.13})$$

Our main goal is to obtain the nondimension pressure distribution P in the channel wall. In order to achieve this goal, we first solve Equation (A.9) for P thus:

$$P(t, \xi, y) = \hat{P}(t, y) - \int_0^\xi \left\{ \lambda \frac{\partial^2 u}{\partial y^2} - \frac{1}{\sqrt{\varepsilon}} \frac{\partial u}{\partial t} - \varepsilon \left(u \frac{\partial u}{\partial \xi} + V \frac{\partial u}{\partial y} \right) \right\} d\xi, \quad (\text{A.14})$$

where $\hat{P}(t, y)$ is an arbitrary function of integration.

Taking into account the small ratio of radius to length, and the parabolic profile along the flow direction, we assume that fluid velocity in the horizontal direction is given by

$$u(\xi, y, t) = \frac{3}{2} U \left(1 - \frac{y^2}{\delta^2} \right), \quad (\text{A.15})$$

where $U(t, \xi)$ is the cross-sectional average velocity. The latter is calculated as follows. First, we integrate the continuity Equation (A.11) from 0 to y and obtain

$$V(t, \xi, y) = -\frac{3}{2} \frac{\partial U}{\partial \xi} \left(y - \frac{y^3}{3\delta^2} \right) - \frac{y^3}{\delta^3} \frac{\partial \delta}{\partial \xi} U + \bar{C}(t, \xi), \quad (\text{A.16})$$

where K is an arbitrary function of integration.

By imposing the relevant boundary conditions on V i.e. Eqs(A.12,A.13), we find

$$\bar{C}(t, \xi) = 0, \quad (\text{A.17})$$

and

$$\frac{1}{\varepsilon^2} \frac{\partial \delta}{\partial t} + \frac{\partial U}{\partial \xi} \delta + \frac{\partial \delta}{\partial \xi} U = 0. \quad (\text{A.18})$$

Thus

$$U = \frac{1}{\delta} \left(\alpha(t) - \frac{1}{\varepsilon^2} \int_0^{\xi} \delta_t(t, z) dz \right), \quad (\text{A.19})$$

where α is an arbitrary function of integration and δ_t denotes $\partial \delta / \partial t$.

Next we substitute Eqs (A.15), (A.16) and (A.19) back into Eq. (A.14) giving:

$$P(t, \xi, y) = \hat{P}(t, y) - \int_0^{\xi} \left\{ \begin{array}{l} \lambda \left(-3U \frac{y}{\delta^2} \right) - \frac{1}{\sqrt{\varepsilon}} \left[\frac{3}{2} \frac{\partial U}{\partial t} \left(1 - \frac{y^2}{\delta^2} \right) + 3 \frac{y^2}{\delta^3} \frac{\partial \delta}{\partial t} U \right] \\ \frac{3}{2} U \left(1 - \frac{y^2}{\delta^2} \right) \left(\frac{3}{2} \frac{\partial U}{\partial t} \left(1 - \frac{y^2}{\delta^2} \right) + 3 \frac{y^2}{\delta^3} \frac{\partial \delta}{\partial t} U \right) \\ + \left(-\frac{3}{2} \frac{\partial U}{\partial \xi} \left(y - \frac{y^3}{3\delta^2} \right) - \frac{y^3}{\delta^3} \frac{\partial \delta}{\partial \xi} U \right) \left(-3U \frac{y}{\delta^2} \right) \end{array} \right\} d\zeta. \quad (\text{A.20})$$

In order to determine $\hat{P}(t, y)$, we solve Eq. (A.10) for P . Then, we substitute the P obtained into Eq.(A.20) and find after some manipulations,

$$\hat{P}(t, y) = \int_0^{\xi} \left\{ \begin{array}{l} \lambda \left(-3U \frac{y}{\delta^2} \right) - \frac{1}{\sqrt{\varepsilon}} \left[\frac{3}{2} \frac{\partial U}{\partial t} \left(1 - \frac{y^2}{\delta^2} \right) + 3 \frac{y^2}{\delta^3} \frac{\partial \delta}{\partial t} U \right] \\ \frac{3}{2} U \left(1 - \frac{y^2}{\delta^2} \right) \left(\frac{3}{2} \frac{\partial U}{\partial t} \left(1 - \frac{y^2}{\delta^2} \right) + 3 \frac{y^2}{\delta^3} \frac{\partial \delta}{\partial t} U \right) \\ + \left(-\frac{3}{2} \frac{\partial U}{\partial \xi} \left(y - \frac{y^3}{3\delta^2} \right) - \frac{y^3}{\delta^3} \frac{\partial \delta}{\partial \xi} U \right) \left(-3U \frac{y}{\delta^2} \right) \end{array} \right\} d\zeta - \varepsilon^2 \int_0^y \frac{\partial V}{\partial t} dy' + \check{P}(t) \quad (\text{A.21})$$

where $\check{P}(t)$ is an arbitrary function of t .

Finally, by substituting Eq. (A.21) back into Eq. (A.20) and solving the resulting equation, we obtain the general form of the pressure distribution written as

$$P(t, \xi, y) = \check{P}(t) + \varepsilon^{\frac{3}{2}} \left[\begin{aligned} & \frac{3}{2} \frac{\partial^2 U}{\partial t \partial \xi} \left(\frac{y^2}{2} - \frac{y^4}{12\delta^2} \right) + \frac{y^4}{4\delta^3} \frac{\partial \delta}{\partial t} \frac{\partial U}{\partial \xi} - \frac{3}{4} \frac{y^4}{\delta^4} \frac{\partial \delta}{\partial t} \frac{\partial \delta}{\partial \xi} U \\ & + \frac{y^4}{4\delta^3} \frac{\partial^2 \delta}{\partial t \partial \xi} U + \frac{y^4}{4\delta^3} \frac{\partial U}{\partial t} \frac{\partial \delta}{\partial \xi} \end{aligned} \right]. \quad (\text{A.22})$$

The nondimensional pressure distribution over the stenosed surface ($y = \delta$) is then:

$$P(t, \xi, y = \delta) = \check{P}(t) + \varepsilon^{\frac{3}{2}} \left[\begin{aligned} & \frac{5}{8} \frac{\partial^2 U}{\partial t \partial \xi} \delta^2 + \frac{\delta}{4} \frac{\partial \delta}{\partial t} \frac{\partial U}{\partial \xi} - \frac{3}{4} \frac{\partial \delta}{\partial t} \frac{\partial \delta}{\partial \xi} U \\ & + \frac{\delta}{4} \frac{\partial^2 \delta}{\partial t \partial \xi} U + \frac{\delta}{4} \frac{\partial U}{\partial t} \frac{\partial \delta}{\partial \xi} \end{aligned} \right], \quad (\text{A.23})$$

where U is given by Eq. (A.19) and $\check{P}(t)$ is an arbitrary function.

By substituting Eq. (A.19) into Eq. (A.23) we finally obtain the pressure distribution over the stenosed surface as

$$P(t, \xi, \delta) = \check{P}(t) + \frac{1}{4} \varepsilon^{\frac{3}{2}} \left\{ \begin{aligned} & \left[\frac{5}{2} \frac{\partial^2}{\partial t \partial \xi} \left[\frac{1}{\delta} \left(\alpha(t) - \frac{1}{\varepsilon^{\frac{3}{2}}} \int_0^\xi \delta_i(t, z) dz \right) \right] \delta^2 + \delta \frac{\partial \delta}{\partial t} \frac{\partial}{\partial \xi} \left[\frac{1}{\delta} \left(\alpha(t) - \frac{1}{\varepsilon^{\frac{3}{2}}} \int_0^\xi \delta_i(t, z) dz \right) \right] \right] \\ & - \frac{3}{\delta} \frac{\partial \delta}{\partial \xi} \frac{\partial \delta}{\partial t} \left(\alpha(t) - \frac{1}{\varepsilon^{\frac{3}{2}}} \int_0^\xi \delta_i(t, z) dz \right) + \frac{\partial^2 \delta}{\partial t \partial \xi} \left(\alpha(t) - \frac{1}{\varepsilon^{\frac{3}{2}}} \int_0^\xi \delta_i(t, z) dz \right) \\ & + \delta \frac{\partial \delta}{\partial \xi} \frac{\partial}{\partial t} \left[\frac{1}{\delta} \left(\alpha(t) - \frac{1}{\varepsilon^{\frac{3}{2}}} \int_0^\xi \delta_i(t, z) dz \right) \right] \end{aligned} \right\} \quad (\text{A.24})$$

Note that pressure is evaluated at points which happen to be also the limits of integration.

Therefore, care must be taken when choosing the numerical method to evaluate Equation (A.24).

Here, we define a new variable

$$F = \alpha(t) - \frac{1}{\varepsilon^{\frac{3}{2}}} \int_0^{\xi} \delta_t(t, z) dz, \quad (\text{A.25})$$

such that F is completely defined by

$$\begin{cases} \frac{\partial F(t, \xi)}{\partial \xi} = -\frac{1}{\varepsilon^{\frac{3}{2}}} \frac{\partial \delta(t, z)}{\partial t} \\ F(0, t) = \alpha(t) \end{cases} . \quad (\text{A.26})$$

A-3-4- Governing Equations – Artery Wall

The artery wall configuration is driven by hemodynamic stresses acting on its surface. The elastic wall configuration is solved as a plate. We start by applying Newton's second law of motion to the surface element presented in Fig A.4.

$$\sum \vec{F} = M \vec{V}, \quad (\text{A.27})$$

where M and \vec{V} are mass and acceleration vector respectively.

The transverse component (Y) of Equation (A.27) is equivalent to

$$\tau_w \sin(\alpha) dx^* - (F + dF) \sin(\alpha + d\alpha) + F \sin(\alpha) - (p_a - p^*) dx^* + V + dV - V = h\rho dx^* \frac{d^2 b^*}{dt^{*2}}, \quad (\text{A.28})$$

where τ_w is the shear stress over the inner face of the wall and ρ the material density

$$F = \sigma_x^* h, \quad V = -\frac{dM}{dx^*}, \quad M = \int_{-\frac{h}{2}}^{\frac{h}{2}} \sigma_x^* y^* dy^*, \quad \sigma_x^* = \frac{E}{1-\nu^2} \varepsilon_x^*, \quad (\text{A.29-a,b,c,d})$$

Based on the Karman's non linear shell theory [21], Djordjevic and Vukabratovic [13] show that the finite strain component in the axial direction is written as

$$\varepsilon_x^* = \frac{da^*}{dx^*} + \frac{1}{2} \left[\left(\frac{da^*}{dx^*} \right)^2 + \left(\frac{db^*}{dx^*} \right)^2 \right]. \quad (\text{A.30})$$

We assume that α is small. Hence $\tan \alpha = -\frac{db^*}{dx^*}$, $\sin(\alpha) \cong \alpha$ and $\sin(\alpha + d\alpha) \cong \alpha + d\alpha$. The

latter approximation converts Equation (A.28) into

$$-\tau_w \frac{db^*}{dx^*} + \frac{Eh}{1-\nu^2} \frac{d^2 b^*}{dx^{*2}} \varepsilon_x^* - \frac{Eh^3}{12(1-\nu^2)} \frac{d^4 b^*}{dx^{*4}} - (p_a - p^*) = h\rho \frac{d^2 b^*}{dt^{*2}} + h.o.t, \quad (\text{A.31})$$

where the abbreviation *h.o.t* stands for Higher Order Terms. We may recast Equation (A.31) into

$$T \frac{d^2 b^*}{dx^{*2}} - D \frac{d^4 b^*}{dx^{*4}} - \tau_w \frac{db^*}{dx^*} - (p_a - p^*) = h\rho \frac{d^2 b^*}{dt^{*2}} + h.o.t, \quad (\text{A.32})$$

where $D = \frac{Eh^3}{12(1-\nu^2)}$ and $T = \frac{Eh}{1-\nu^2} \varepsilon_x^*$ are the bending stiffness and the longitudinal tension

respectively.

The axial component (X) of the equation of motion is

$$\begin{aligned} & -F \cos(\alpha) + (F + dF) \cos(\alpha + d\alpha) - \tau_w \cos(\alpha) dx^* + (p_a - p^*) \sin(\alpha) \\ & = h\rho \frac{d^2 a^*}{dt^{*2}} dx^* + h.o.t \end{aligned} \quad (A.33)$$

Using the fact that α is small we obtain

$$\frac{dT}{dx^*} - \tau_w + (p_a - p^*) \frac{\partial b^*}{\partial x^*} = \rho h \frac{d^2 a^*}{dt^{*2}}. \quad (A.34)$$

Now, we proceed to non-dimensionalizing of the Equations (A.31) and (A.32) by introducing the non-dimensional variables

$$x = \frac{x^*}{\delta_o}, \quad a = \frac{a^*}{\delta_o}, \quad b = \frac{b^*}{\delta_o}, \quad a = \varepsilon A(t, \xi), \quad \xi = \varepsilon x, \quad t = \frac{1}{\sqrt{\varepsilon}} \frac{t^*}{t_o}, \quad t_o = \frac{\delta_o}{u_o} \quad (A.35-a - g)$$

In terms of the new variables, we have

$$\varepsilon_\xi = \varepsilon^2 \left[\frac{dA}{d\xi} + \frac{1}{2} \left(\frac{\partial b}{\partial \xi} \right)^2 \right] + O(\varepsilon^4). \quad (A.36)$$

Equations (A.31) and (A.32) become respectively,

$$\begin{aligned} \varepsilon^4 \frac{E}{1-\varrho^2} \frac{h}{\delta_o} \left[\frac{dA}{d\xi} + \frac{1}{2} \left(\frac{\partial b}{\partial \xi} \right)^2 \right] \frac{\partial^2 b}{\partial \xi^2} - \frac{E\varepsilon^4}{12(1-\varrho^2)} \left(\frac{h}{\delta_o} \right)^3 \frac{\partial^4 b}{\partial \xi^4}, \\ -\varepsilon^n P(t, \xi, y) p_o = \varepsilon^n p_o \frac{h}{\delta_o} \frac{d^2 b}{dt^2} + O(\varepsilon^{n+1}) \end{aligned} \quad (\text{A.37})$$

and

$$\varepsilon^3 \frac{E}{1-\varrho^2} \frac{h}{\delta_o} \frac{\partial}{\partial \xi} \left[\frac{dA}{d\xi} + \frac{1}{2} \left(\frac{\partial b}{\partial \xi} \right)^2 \right] + O(2p_o \varepsilon^{n+1} \frac{h}{\delta_o}) = 0. \quad (\text{A.38})$$

The integration of Equation (A.38) yields

$$\frac{dA}{d\xi} + \frac{1}{2} \left(\frac{\partial b}{\partial \xi} \right)^2 = K(t). \quad (\text{A.39})$$

Thus

$$\int_0^L \left(\frac{\partial b}{\partial \xi} \right)^2 d\xi = 2K(t)L. \quad (\text{A.40})$$

where L is the nondimensional wall length.

Using the dominant balance in (A.37), we set

$$\varepsilon^4 \frac{E}{1-\mathcal{G}^2} \frac{h}{\delta_o} = \varepsilon^n p_o. \quad (\text{A.41})$$

Recall also that

$$Eu = \frac{p_o \delta_o^2 \lambda^2}{\rho v^2} = O(1). \quad (\text{A.42})$$

Equations (A.41) and (A.42) imply that

$$n = -\left(1 + \frac{\ln Eu}{\ln \varepsilon}\right), \quad \varepsilon = \left[\frac{\rho v^2 (1-\mathcal{G}^2)}{Eh\delta_o \lambda^2}\right]^{\frac{1}{5}}. \quad (\text{A.43-a,b})$$

Using Equation (A.40), Equation (A.28) can be rewritten as

$$K \frac{\partial^2 b}{\partial \xi^2} - \frac{1}{12} \left(\frac{h}{\delta_o}\right)^2 \frac{\partial^4 b}{\partial \xi^4} - P = \frac{h}{\delta_o} \frac{d^2 b}{dt^2}. \quad (\text{A.44})$$

Recalling that $b = \delta - 1$, Equation (A.44) may be transformed further to

$$K \frac{\partial^2 \delta}{\partial \xi^2} - \frac{1}{12} \left(\frac{h}{\delta_o} \right)^2 \frac{\partial^4 \delta}{\partial \xi^4} - P = \frac{h}{\delta_o} \frac{\partial^2 \delta}{\partial t^2}, \quad (\text{A.45})$$

or equivalently

$$-m_1^2 \delta^{(IV)} + m_2 \delta^{(III)} - m_3 = 12m_1 \ddot{\delta}, \quad (\text{A.46})$$

where the superscripts and the overdot stand for differentiation with respect to ξ and t

$$m_1 = \frac{h}{\delta_o}, \quad m_2 = 12K, \quad m_3 = 12P. \quad (\text{A.47-a-c})$$

In the next section, we show the numerical methods used to solve the governing equations for fluid flow Eq. (A.24) and artery wall Eq. (A.46).

A-3-5- Numerical Solution

The main issue with the wall governing equation (A.47) in the transient state is solving a single differential equation with two unknowns, including transmural pressure distribution P and wall deflection δ . Computation of the wall shape (wall deflection) at the next time step proceeds as follows. Knowing the wall shape at the initial time step (deflection distribution δ at the initial

time), we solve the equation of the transmural pressure Eq.(A.24) for P . Then, at the next time step we solve the wall governing equation (A.45) for δ under the assumption that the time step Δt is small enough to apply $P|_{t=n} \approx P|_{t=n+1}$. Next, given the updated solution for δ , we can find the corresponding updated P , and so on until the final iteration in time.

A numerical method used for solving the transmural pressure equation (A.24) and governing equation (A.45) was finite differencing method [23,24]. Specifically, the arterial wall was discretized into segments. Next, a node was placed between two consecutive segments. More than 100 nodes were distributed over the wall length. Then incremental numerical calculations were applied at each node.

For the differential terms included in the transmural pressure Equation (A.24) and governing Equations (A.45), forward and central schemes [23] were used to solve time and space dependent terms respectively. Also, the trapezoidal rule [24] was utilized for solving the integral term Equation (A.25). The numerical code has been tested for steady flow by increasing the number of nodes and comparing with results from different methods (Djordjevic et al. [13] and Luo et al. [10])

The solution procedure is initialized with the definition of the shape of the stenotic arterial wall with a small slope in fulfillment of the lubrication theory. Next, with the imposed boundary conditions and numerical schemes in place, the transmural pressure is solved first at all the nodes of the wall. The matrix containing the transmural pressure at each node is inserted into the

governing Equation (A.45). Then the latter equation is solved for all the nodes at once using implicit Thomas algorithm method [23]. The results obtained provided the new location distribution of nodes at the current time step. Finally, the arterial wall new configuration is used to update the initial configuration for the next time step and so on. The solution process continues in time until the input number of steps is achieved or the model becomes unstable. The model stability is controlled by Courant number C , defined as $U_{\max} * \Delta t / \Delta x < C$, where $C=1$ and U_{\max} is the maximum flow velocity. All the computation are performed using Matlab 6.5 software.

A-4-Results

In this section, we present results and discuss how they vary with the control parameters, including inlet velocity U_0 , inlet transmural pressure tP and arterial wall thickness h . Meanwhile we keep fix other parameters such as Model length L , Elastic modulus E , fluid viscosity, μ and density ρ . The input data utilized in this study are presented on table A.

Table A. Input data utilized in this study.

Parameters	Length- L-mm	Radius - δ_o - mm	Inlet velocity- Uo-m/s	Reynold number- Re	Inlet Transmural pressure-tP Pa	Kinematic viscosity- ν - m^2/s
Values	100	3	0.1 – 0.3	3.2 – 9.6	180 - 210	$3.6*10^{-6}$
Parameters	Elasticity Modulus- E- N/m^2	Poisson ratio- \mathcal{G}	Wall initial deflection	Wall thickness -h-mm	Reference pressure- Po-Pa	Fluid Density- $\rho - kg.m^{-3}$
Values	$5.6* 10^5$	0.49	10%	0.7 -0.9	10^5	1100

In order to compare our results with those obtained Djordjevic et al. [13] on steady state cases, we applied at the tube inlet a parabolic profile velocity (A.15). The figure A.5 presents the plot of the time dependent cross sectional average velocity $U(t, \xi)$ (A.19) calculated at the inlet and $\frac{1}{2}$ distance of the model length. We chose to apply oscillatory flow velocity in order to simulate an oscillatory blood flow. Also, it is worth noting that average velocity not only varies with respect to time but also with respect to space as fluid flows through the constricted segment of the channel.

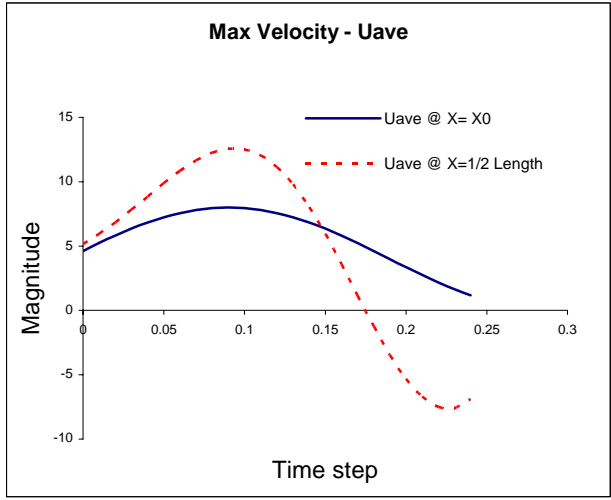


Figure A.5 Average velocity profile of pulsatile flow applied at the inlet and 1/2 distance of the model length.

A-4-1- Variation of the Inlet Velocity

Figure A.6 present the wall deflection for inlet velocity U_0 ranged from 0.1 to 0.3 m/s corresponding to Reynolds number ranged from 3.2 to 9.6. well within the condition prescribed for lubrication theory. The other parameters such as transmural pressure at the inlet $tP=180$ Pa, Wall thickness $h=0.8$ mm, are kept constant.

In the figure, the amplitude of wall deflection is reduced as the inlet velocity U_0 increases. The increase of initial velocity implies increase Reynolds number which is followed by the decrease of pressure. This reduction is due to the decrease of transmural pressure, $p = \varepsilon^n P(\xi, y, t)$ Eq. (A.4) directly associated to U_0 through the parameters n and ε (A.43-a,b). Fig. A.6-a shows the membrane deflection is the highest as we move close to its half length. This trend was also found by Djordjevic et al. [13] and Luo& Pedley [10,19]. In this case, the magnitude of transmural pressure (presented in fig. A.8–b) and wall oscillation and suggest possible closeness to breakdown in the equilibrium. Fig. A.6, b&c , show the wall deflection is higher upstream half of the channel than downstream due to the effect of internal pressure acting more that side of the membrane. These latter results are commonly found when parameters are correctly chosen.

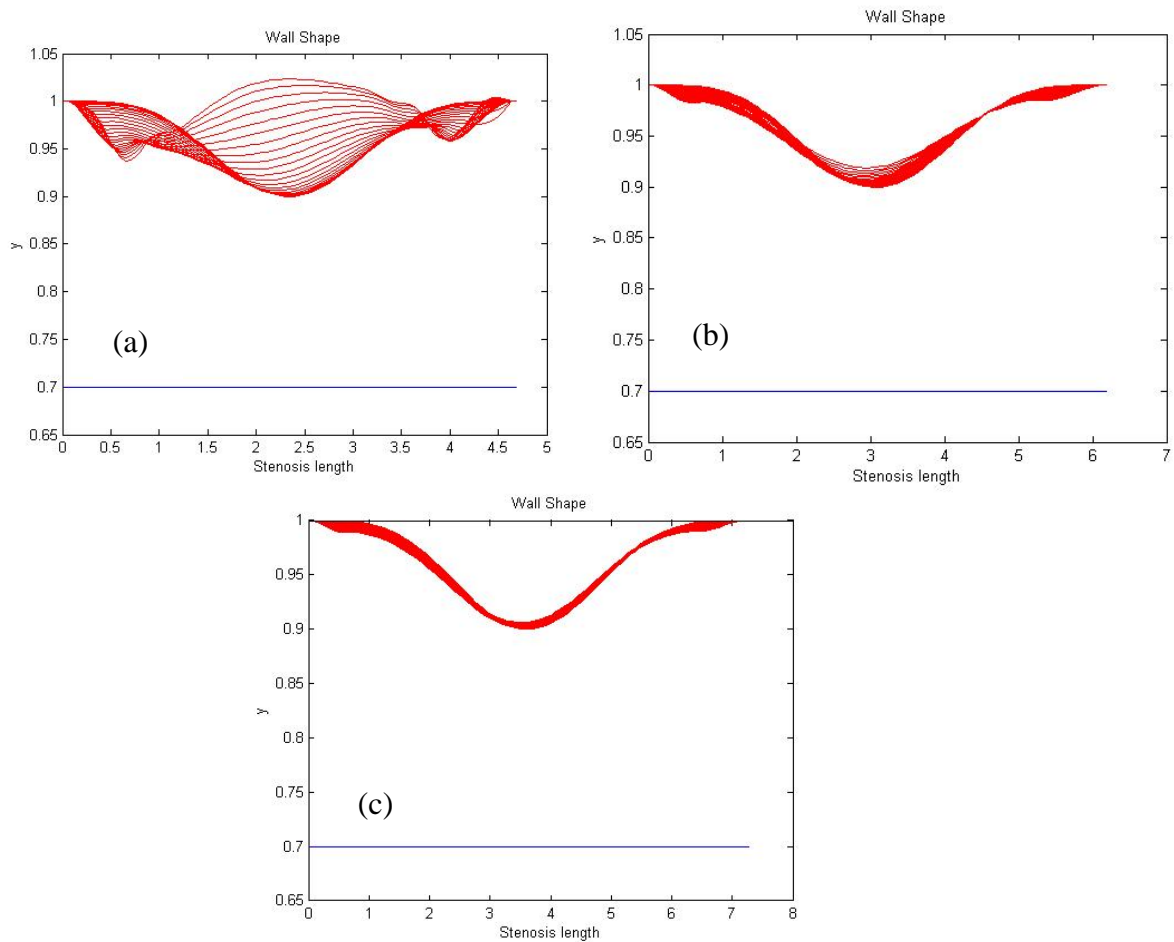


Figure A.6: Wall shape as the inlet velocity U_0 increases from 0.1m/s (a) to 0.2m/s (b) to 0.3m/s (c).

A typical velocity distribution is presented in figure A.7. It shows that flow velocity has a parabolic profile through out the channel and it reaches its maximum at the centerline in the area the tube is constricted.

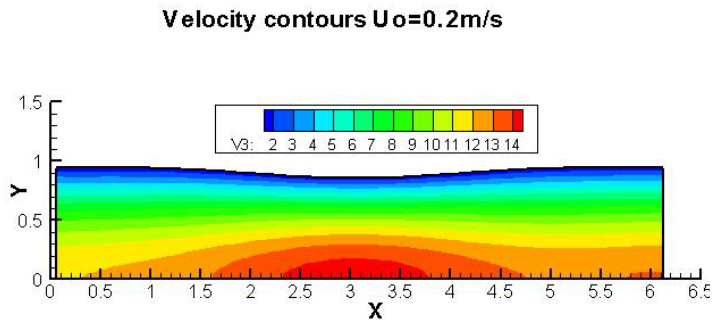


Figure A.7: Typical velocity profile at time $t=0.1$ shows that the flow is fully developed throughout the channel

The increase of inlet velocity U_0 is balanced by the reduction of transmural pressure as shown in Fig. A.8-b. As pressure reduces, so does the wall deflection. Therefore, reduction of wall deflection leads to the reduction of the shear stress as shown in Fig. A.8-a. The magnitude of the shear stress is the highest upstream close to tough of membrane, then it slightly reduces as the flow moves towards the model outlet. In the other hand, transmural pressure drops rapidly after passing the tough of the membrane. The drop is due to the channel expansion, then pressure start to increase again owing to flow recovery. It is worth noting that the abrupt oscillations show in Fig. A.8 a&b, are due to the limitation of the numerical model to handle the imposed inlet and outlet boundary conditions. Specifically, due to the rigid wall at the inlet and outlet, we force the motion to be zero which leads to the discontinuity of the numerical code results.

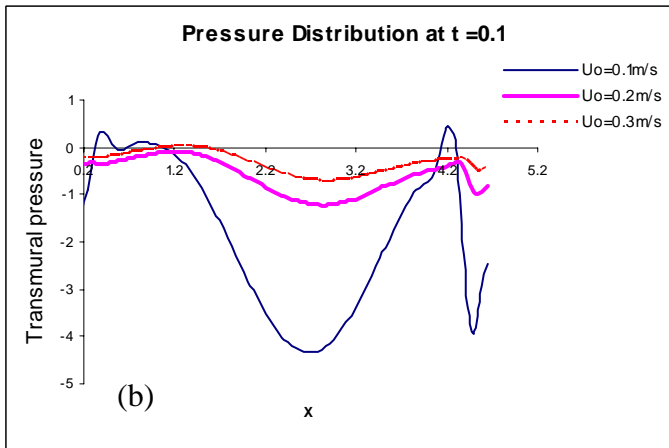
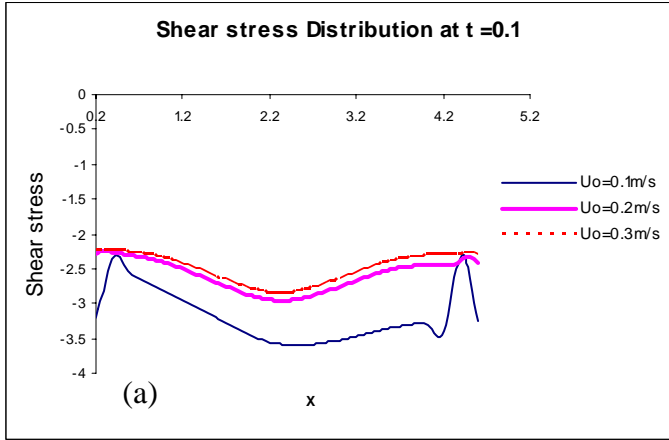


Figure A.8: (a) the wall shear stress distribution and (b) pressure distribution for inlet velocity range from 0.1 m/s to 0.3m/s

A-4-2- Variation of the Inlet Transmural Pressure

The increase of the inlet transmural pressure (tP) results in the membrane to move upward. The transmural pressures applied at the inlet are 180. Pa (Fig. A.9-a), 200 Pa (Fig. A.9-b), 220 Pa (Fig. A.9-c).

The figure shows that the wall deflection increase with inlet transmural pressure increase. Specifically, increasing tP results in increase of internal pressure, and thereby a reduction of flow velocity. Therefore, as presented in the figure, upstream of the wall displays higher deflection magnitude than downstream. There is a bulge appearing at the upstream end, this bulge was also obtained by Luo and Pedley [19] on model with higher initial wall constriction. In addition, we observe another bulge downstream end. This downstream bulge is not surprising in high transmural cases with small wall constriction. Specifically, due to the initial small wall deflection, we expect to obtain the same pattern of result on both ends of the membrane. Large wall displacements following pressure increase has been also found by Djordjevic et al. [13] in similar study for steady state analysis.

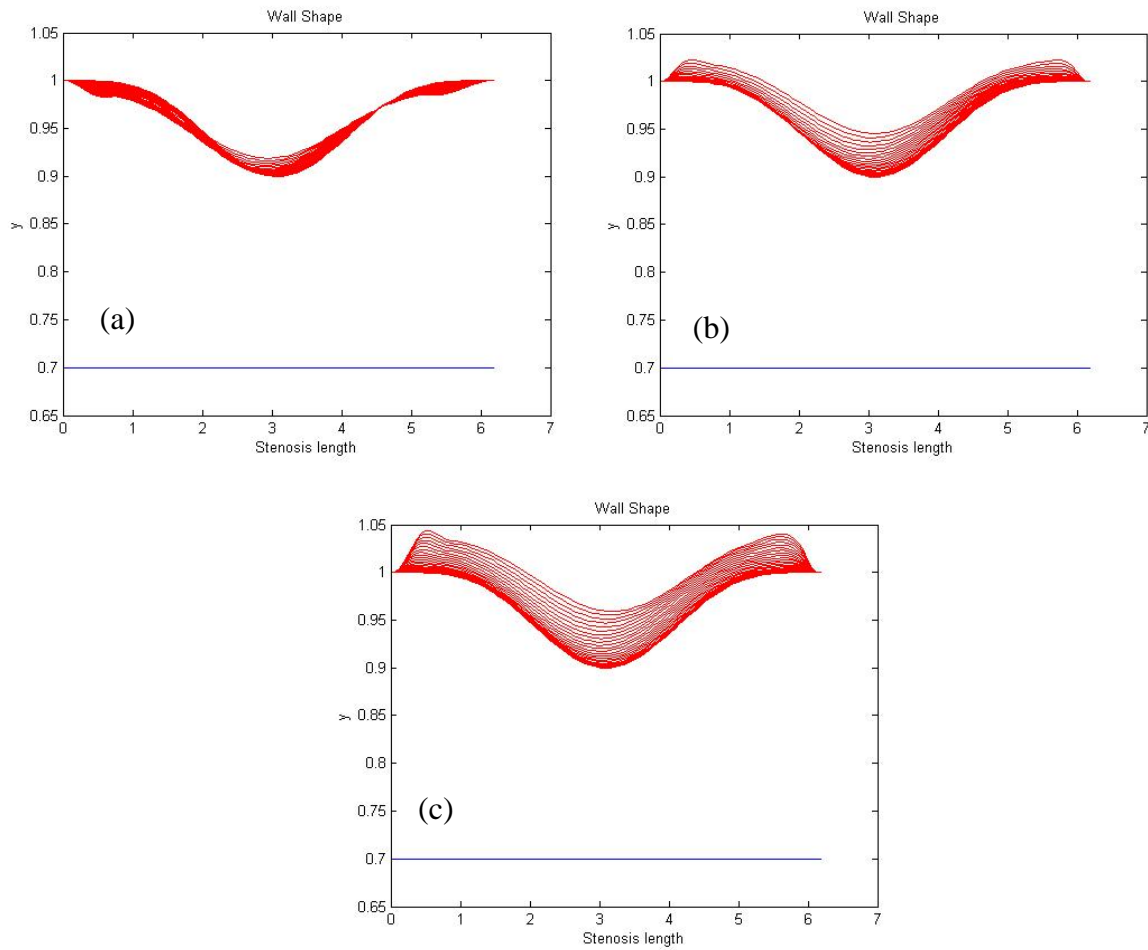


Figure A.9: Wall shape as the inlet transmural pressure, tP increases from 180 Pa (a) to 200 Pa (b) to 220 Pa (c).

It was found in similar study for steady state analysis that increasing the transmural pressure is similar to reduce the longitudinal tension in the membrane [19] or increase internal pressure (Fig. A.10-b); thus it flattens the membrane. The flattened wall causes less friction, thereby impact on the wall shear stress. This trend is also achieved in our results as shown in Fig. A.10.

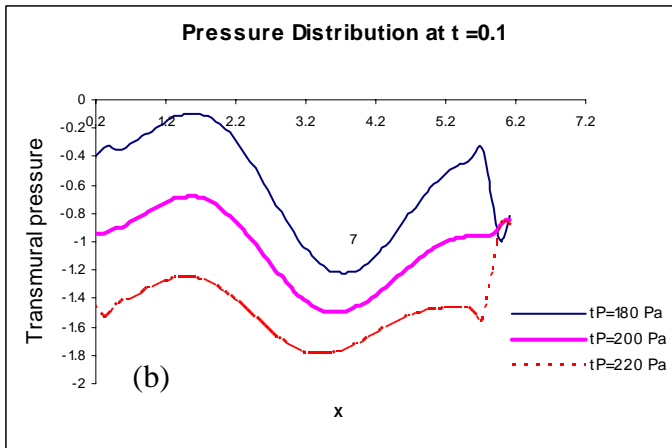
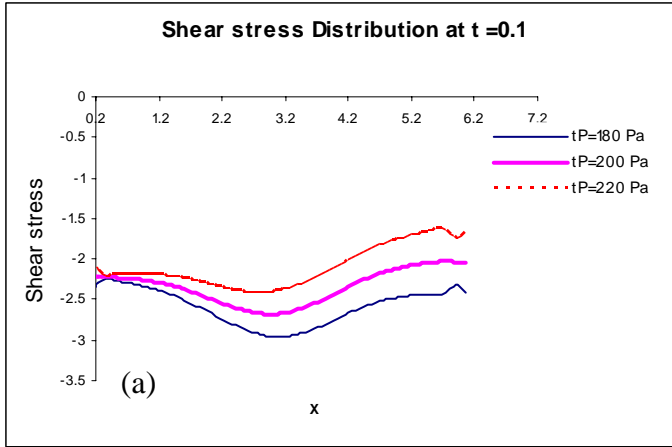


Figure A.10: (a) the wall shear stress distribution and (b) pressure distribution for inlet transmural pressure of 180 Pa, 200 Pa and 220 Pa

A-4-3- Variation of the Wall Thickness h

The increase of the wall thickness requires increase of internal pressure to maintain the dynamic membrane in place and thereby prevent its collapse. The collapsing is due to the unbalance wall governing equation, specifically, since the wall thickness h is part of the 4th order bending force of the single integro-differential equation (A.45), the most dominating term of the wall

governing equation, the slight change in the bending term has great impact on the wall configuration. The results of effects of wall thickness on wall configuration are presented in figure A.11. The wall thicknesses utilized in this calculation are $h = 0.7$ mm (Fig. A.11-a), 0.8 mm (Fig. A.11-b), 0.9 mm (Fig. A.11-c).

When the membrane is thicker from 0.7 mm to 0.8 mm, and keeping the same values of the other control parameters, the membrane deflections are smaller. These results are consistent with those obtained by Djordjevic et al. [13] on steady state analysis. However, when the wall thickness increases to $h = 0.9$ mm, although the deflection at the trough is still smaller than the other cases, the crests display larger deflections. These large displacements may be due to the beginning of breakdown of the equilibrium in the wall governing equation (A.46). In deed, increasing the wall thickness and keeping the other parameters unchanged affect the overall balance of the equation, thus the collapse of the membrane at its ends is caused by predominance of the bending term in the governing equation.

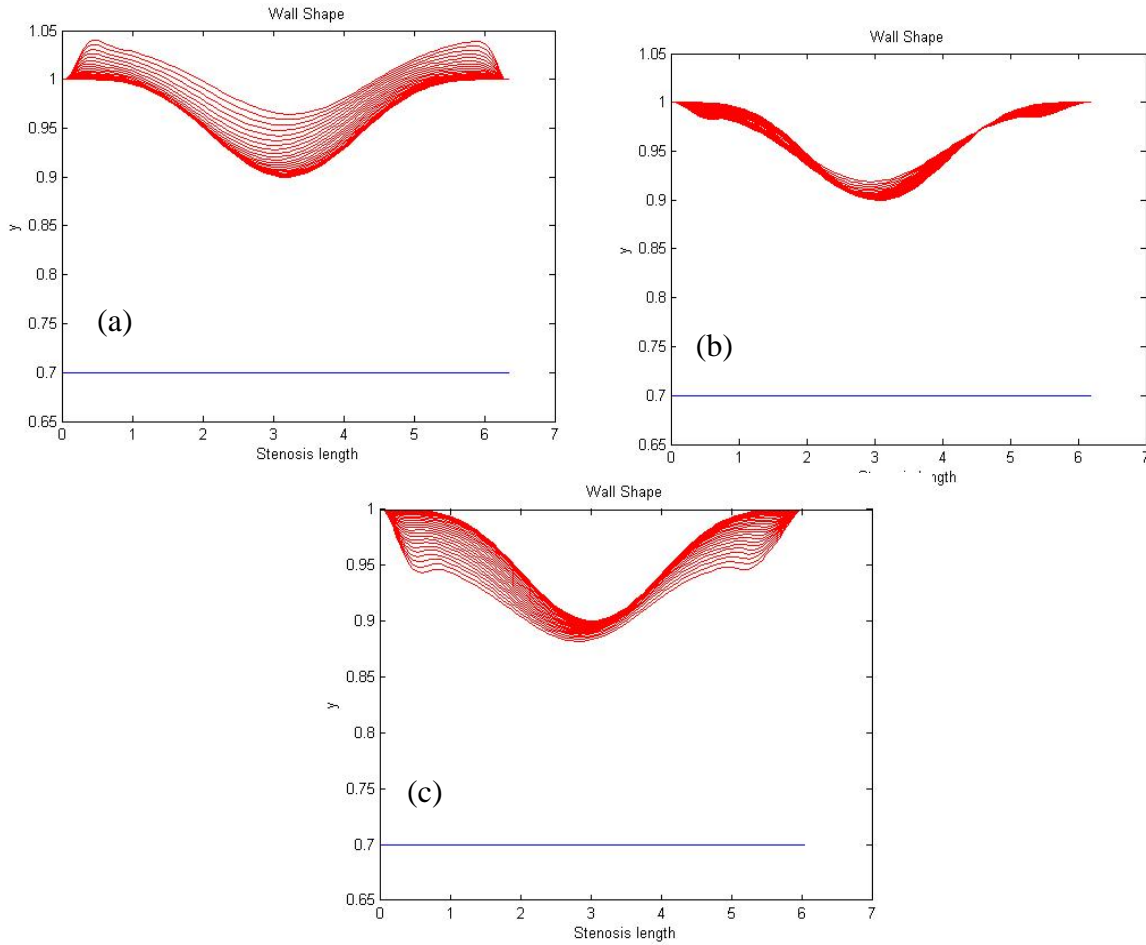


Figure A.11: Wall shape as the wall thickness increases from 0.7 mm (a) to 0.8 mm (b) to 0.9 mm (c).

Figure A.12 shows that as the wall thickness increases, transmural pressure drop (Fig. A.12-b). The pressure drop causes the membrane to collapse and thereby the membrane deflection is increased, thus the increase of the shear stress (Fig. A.12-a).

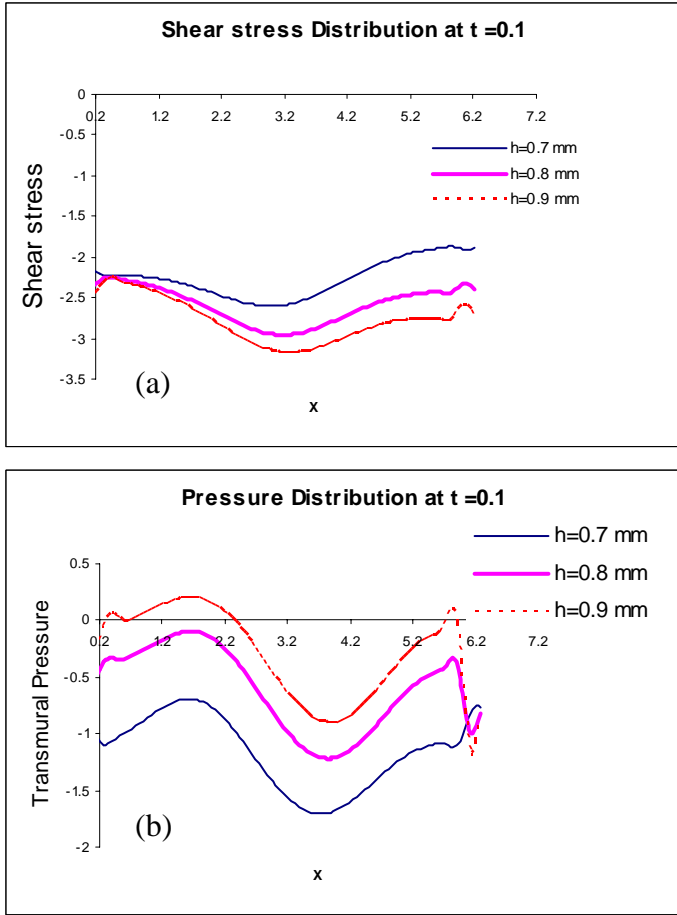


Figure A.12: (a) the wall shear stress distribution and (b) pressure distribution for wall thickness varying from 0.7 mm to 0.9 mm

All the results presented in fig. A.6 to A.12 are characterized by asymmetry due to the effect of flow momentum. This asymmetric I consistent with results obtained by Luo and Pedley [10,19] in studies of similar model but for membrane with larger initial deflection.

A-4-4- Closing Remarks

Our results suggest that, an increase in the inlet velocity is balanced by a reduction in transmural pressure. A reduction in transmural pressure results in a reduction of wall deflection which in turn leads to a reduction in the shear stress. The magnitude of membrane deflection is higher upstream than downstream.

Since increase in transmural pressure is accompanied by a corresponding increase in internal pressure and wall deflection, the wall deflection is larger upstream than downstream. An increase in wall thickness results in a reduction in the wall deflection and ultimately wall collapse. Maintaining the membrane in place requires increase in internal pressure. Increasing the wall thickness while keeping the other parameters constant affects the overall balance of the governing equation. Indeed, collapse of the membrane at its ends is caused by predominance of the bending term in the single integro differential equation.

Our analysis has shown that with proper assumptions the model can be designed to assess the unsteady flow structure interaction phenomena in a constricted compliant channel. The results obtained from the investigation are consistent with previous studies [10,19,25].

A-5- Conclusion and Recommendations

A-5-1- Conclusion

A time-dependent model of 2-D constricted channel was developed using lubrication theory and Karman plate approach to obtain expressions for transmural pressure and a single integro-differential equation for the wall behavior. The finite difference method was used to solve the fluid-structure interaction problem. Parametric studies were conducted of the effect on the unsteady flow model of inlet velocity, inlet transmural pressure and wall thickness.

Using plate theory [13,21] in the transient state, the present model provides a new approach to examine the details of fluid flow behavior in a compliant wall. The work will enable further studies to develop improved analytical models to enhance our understanding of the fluid-structure interaction mechanism. Although the present model enables us to investigate the system's behavior at low Reynolds numbers, it cannot be relied on to investigate the self excited oscillations which are observed in many experiments since they tend to appear at high Reynolds numbers

Our results suggest that an increase in the inlet velocity is balanced by a reduction in transmural pressure. A reduction in transmural pressure results in a reduction of wall deflection which in turn leads to a reduction in the shear stress. Since increase in transmural pressure is accompanied by a corresponding increase in internal pressure and wall deflection, the wall deflection is larger

upstream than downstream. An increase in wall thickness results in a reduction in the wall deflection and ultimately wall collapse. Maintaining the membrane in place requires increase in internal pressure. Increasing the wall thickness while keeping the other parameters constant affects the overall balance of the governing equation. Indeed, collapse of the membrane at its ends is caused by predominance of the bending term in the single integro-differential equation.

Our analysis has shown that with proper assumptions the model can be designed to assess the unsteady flow-structure interaction phenomena in a constricted compliant channel. The results obtained from the investigation are consistent with previous studies [10,12,13].

A-5-2- Recommendations

The next stage of the analytical investigation is to improve the model by relaxing the assumptions and extend to larger initial membrane curvature and higher Reynolds numbers. It is also desirable to analyze stability of the problem and assess the conditions contributing to breakdown of the equilibrium.

Next, it would be interesting to perform stability analysis of the improved model to investigate the membrane self-excited oscillation [10,19,25]. The investigation will help to determine the role each controlling parameter plays in order to focus on the most important one to analyze the fluid-structure phenomena. Ultimately, we would like to investigate the fully coupled three-dimensional model and compare the results with the 2D analyses. The investigation of the fully

three-dimensional problem would reveal many features unique to the geometry [10,19], such as snap-through buckling of the tube wall, flow division into two lobes which remains open during the buckling, buckling with higher circumferential wave numbers for increased upstream pressure, etc.

A-6- References

- [1] Mathias Heil, “ Stokes Flow in collapsible Tubes: Computation and experiment”, J. Fluid Mech. (1997), vol. 353, pp. 285-312
- [2] Katz, A. I., Chen, Y. & Moreno, A. H. “Flow Through a Collapsible Tube. Experimental Analysis and Mathematical Model ” Biophys. J. (1989), 9, 1261-1279
- [3] Conrad, W. A. “Pressure-Flow Relationships in Collapsible Tubes”, IEEE Trans. Biomed. Engng BME-16, (1969) 284-295
- [4] Kamm, R. D., Pedley, T.J., “ Flow in Collapsible Tubes: A Brief Review”, Journal of Biomechanical Engineering, August , 111, 177-179 (1989)
- [5] James B. Grotberg and Olivier E. Jensen, “ Biofluid Mechanics in Flexible Tubes”, 36:121-147 (2004)
- [6] Roland L. Panton, “ Incompressible Flow” second edition, A Wiley-interscience publication (1995)
- [7] Ascher H. Shapiro, “Steady Flow in Collapsible Tubes”, J. Biomech. Eng, 126-147 (1977)
- [8] Rast, M. P. “Simultaneous Solution of the Navier-Stokes and Elastic Membrane Equations by a Finite-Element Method”, Intl J. Numer. Meth. Fluids (1994), 19, 1115-1135
- [9] Lowe, T. W. & Pedley, T. J. “ Computation of Stokes Flow in a Channel with a Collapsible Segment”, J. Fluids Struct. (1995), 9, 885-905
- [10] Luo, X. Y. & Pedley, T.J., “ A Numerical Simulation of Unsteady Flow in a 2-D Collapsible Channel”, J. Fluids Mech. (1996) 314, 191-225
- [11] Shin, J. J. “The Numerical Simulation of Flow Through Collapsible Channels”, Ph.D. Thesis (1996), MIT
- [12] Pedley T. J., “ Longitudinal Tension variation in collapsible Channels: A New Mechanism for the Breakdown of Steady Flow”, J. Biomech. Eng, 144, 60-67 (1992)
- [13] V. D. Djordjevic, M. Vukobratovic, “ On a Steady, Viscous Flow in Two-Dimensional Collapsible Channels”, Acta Mechanica (2003) 163, 189-205

- [14] Heil, M. “ Large Deformations of Cylindrical Shell Conveying Viscous Flow”, Ph.D. Thesis (1995), University of Leeds.
- [15] Heil, M. & Pedley, T. J. “ Large Post- Buckling Deformations of Cylindrical Shells Conveying Viscous Flow”, *J. Fluids Struct.* (1996) 10, 565-599
- [16] T. J. Pedley, “Fluid Mechanics of Large Blood Vessels” , Cambridge University Press, Cambridge, 1980
- [17] V. Shankar and V. Kumaran, “Stability of Wall Modes in Fluid Flow Past a Flexible Surface,” *Phys. Fluids* 14, 2324 (2002)
- [18] A. D. Shah, J. D. Humphrey, “Finite Strain Elastodynamics of Intracranial Saccular Aneurysms”, *Journal of Biomechanics* 32 (1999) 593 –599
- [19] Luo, X. Y. & Pedley, T.J., “ A Numerical Simulation of steady Flow in a 2-D Collapsible Channel”, *J. of Fluids and structures.* (1995) 9, 149-174
- [20] Nicholson, W. David, 2003, “Finite Element Analysis, Thermomechanics of Solids”, CRC Press, Florida.
- [21] T. Atanackovic, A. Guran, “ Theory of elasticity for Scientists and engineers” Birkhauser, 2000
- [22] Kobayashi, S., Tsunoda, D., and al. “ Flow and compression in arterial models of stenosis with lipid core”
- [23] Tannehill, J., Anderson, D., Pletcher, R., “Computational Fluid Mechanics and Heat Transfer”, second Edition, Taylor&Francis, 1997
- [24] Chapra, S., Canale, R., “Numerical Methods for Engineers with software and programming applications” Boston, MacGraw-Hill, 2002
- [25] Jensen, O. E., “Instabilities of Flow in a Collapsed Tube”, *J. Fluid Mech.* 220, 623-659